ALFVÉN WAVES IN THE INTERPLANETARY MEDIUM

Thesis by

John Winston Belcher

In Partial Fulfillment of the Requirements

For the Degree of

Doctor of Philosophy

California Institute of Technology

Pasadena, California

1971

(Submitted December 14, 1970)

In Memory of my Father

JOHN COOK BELCHER

And to my Mother

MARGIE HARRIS BELCHER

ACKNOWLEDGMENTS

I wish to thank first and foremost my thesis adviser, Professor Leverett Davis, Jr., for his constant and unfailing guidance, advice, and encouragement during the course of this work.

I am deeply indebted to the Mariner V plasma experimenters, H. S. Bridge, A. J. Lazarus, and C. W. Snyder, for extensive use of their detailed plasma data. I am similarly indebted to the Mariner V magnetometer experimenters, P. J. Coleman, L. Davis, Jr., E. J. Smith, and D. E. Jones for access to and use of the magnetic field data. I am thankful to all of these experimenters for helpful and stimulating discussions.

My graduate studies at Caltech were supported in part by the National Science Foundation and by the National Aeronautics and Space Administration (under NASA grant NGR-05-002-160).

ABSTRACT

A study of the wave properties of the microscale fluctuations (scale lengths of .01 a.u. and less) in the interplanetary medium is presented using plasma and magnetic field data from Mariner V (Venus 1967). The reduction procedure for the magnetic field data is summarized, and descriptions are given of the MIT plasma data and the merged plasma/field data tapes used in the analysis.

Observationally, it is found that large amplitude, non-sinusoidal Alfvén waves propagating outward from the sun with a broad wavelength range from 10^3 to 5×10^6 km dominate the microscale structure at least 50% of the time. The waves frequently have an energy density comparable both to the unperturbed magnetic field energy density and to the thermal energy density. The purest examples of the Alfvén waves are found in high velocity solar wind streams and on their trailing edges. The largest amplitude waves occur in the compression regions at the leading edges of high velocity streams where the velocity increases rapidly with time. In addition to being transverse to the average magnetic field direction, $\underset{\sim}{e}_B$, the Alfvénic fluctuations generally exhibit a 10% partial polarization in the $\underset{\sim}{e}_B x \underset{\sim}{e}_R$ direction, where $\underset{\sim}{e}_R$ is a unit vector radially away from the sun. Presumably magnetoacoustic wave modes occur, but they have not been identified, and, if present, have a small average power of the order of 10% or less of that in the Alfvén mode.

These observations are organized on the basis of a model of the solar wind velocity structure. Most of the Alfvén waves in the

interplanetary medium seem likely to be the undamped remnants of waves generated at or near the sun. The high level of wave activity in high velocity, high temperature streams can be interpreted as evidence for the extensive heating of these streams by wave damping near the sun. The highest level of Alfvénic wave activity in the compression regions at the leading edges of high velocity streams may be due either to the amplification of ambient Alfvén waves in high velocity streams as they are swept into the compression regions or to the fresh generation of waves in these regions by the stream-stream collisions. The observed absence of the magnetoacoustic modes is evidence for their strong damping. The $\underset{\sim}{e}_B x \underset{\sim}{e}_R$ anisotropy is viewed as due to the partial conversion of the Alfvén waves to the damped magnetoacoustic modes as they are convected away from the sun; this process continually transfers energy from the micro-scale field fluctuations to the thermalized solar wind plasma.

The detailed behavior of the Alfvén waves and their effects on the dynamics of the expanding solar corona as they propagate and are convected out into interplanetary space is investigated in a simplified one fluid polytrope model of the solar wind. It is found that the inclusion of energy fluxes due to Alfvén waves at the base of the corona can result in significant changes in the large scale streaming properties of the solar wind.

TABLE OF CONTENTS

CHAPTER I

INTRODUCTION

A. Large Scale Properties of the Solar Wind

The interplanetary medium is a rarefied, essentially collisionless plasma whose thermal and magnetic field energy densities are usually of the same order of magnitude. A knowledge of the wave and turbulence properties of this medium is essential for a reasonably complete understanding of the solar wind, its energy sources, and its interaction with cosmic rays, the planets, and the interstellar region. The wave properties of such plasmas are also of general astrophysical interest, and spacecraft observations made in situ offer a unique opportunity to study these properties directly. The present work is primarily a phenomenological study of the small scale fluctuations superimposed on the supersonic streaming motion of the solar wind, using simultaneous plasma and magnetic field data from Mariner 5 (Venus 1967). We first review the large scale characteristics of the solar wind, and consider briefly the types of waves and discontinuities which might be expected to produce small scale fluctuations in the interplanetary plasma. The Mariner 5 experiment and the data reduction process are then described. The identification of Alfvén waves on the basis of both plasma and field data is demonstrated, and the properties of these waves, in particular their patterns of occurence with respect to the large scale solar wind streams, are described. Deficiencies in previous models of the small scale fluctuations are pointed out, and a qualitative model is presented for the origins and energy

sources of these fluctuations which explains many of their observed properties. Finally, we discuss a quantitative mathematical model for the interaction of the waves and the solar wind, and show that the presence of the waves can be a significant factor in the dynamics of the expanding solar corona.

The large scale properties of the solar wind are well known (for a comprehensive review, see Hundhausen [1968]). The plasma itself is a hot, ionized gas consisting primarily of electrons, protons, and alpha particles (~4% by number); it is highly conducting and essentially collisionless. The proton number density at 1 a.u. is typically 8 particles/cm^3, with an average field strength B of 8 γ (10^{-5} gauss), giving an Alfvén velocity ($B/(4\pi\rho)^{\frac{1}{2}}$) of around 50 km/sec and a proton cyclotron frequency (eB/m_p) on the order of 1 cps. The solar wind velocity at 1 a.u. averages 400 km/sec, with only small (~5%) deviations from purely radial flow. The magnetic field direction is on the average along the classic spiral field direction [Parker, 1963], with a hose angle of about 45° at the orbit of the earth.

The proton thermal speed averages around 40 km/sec. Alpha particles generally have the same thermal speed as the protons, and are thus four times hotter. Electron temperatures are much more difficult to measure, but they appear to be slightly higher than the proton temperatures, and show less variation. The adiabatic expansion and cooling of the plasma as it flows outward results in a temperature anisotropy aligned with the magnetic field, with the proton temperature parallel to the field direction typically a factor of 2.0 higher than that perpendicular. The electron parallel temperature is on the

average only 1.2 times higher than that perpendicular. The ratio of proton thermal energy density to magnetic field energy density is typically .6 at 1 a.u.

There are large scale fluctuations about these average values [Neugebauer and Snyder, 1966]. High velocity streams (~600 km/sec) with high proton thermal speeds (~80 km/sec) and low densities (~5/cm^3) are interspersed with low velocity streams (~300 km/sec) which are colder (~30 km/sec) and more dense (~25/cm^3). The usual duration of one of these streams is on the order of two days and longer. The patterns of occurence of the smaller scale plasma waves are closely related to these large scale streaming patterns. The nature of this relationship is discussed in subsequent chapters.

B. MHD Fluctuations

Irregular small scale fluctuations in the magnetic field and velocity are usually superimposed on the large scale spiral field and stream structure. In order to understand the probable physical nature of these fluctuations, we briefly review the properties of small amplitude waves and abrupt discontinuities in the magnetohydrodynamic (MHD) approximation.

1. Waves

The theory of small amplitude waves in a collisionless plasma with a static magnetic field is extensive. Approaches to the problem include the cold plasma approximation [Stix, 1962; Montgomery and Tidman, 1964], the two-fluid approximation [Stringer, 1963], and, in the hydromagnetic limit (i.e., in the limit of frequencies small

compared to the ion cyclotron frequency and of wavelengths long compared to the gyroradius), the double adiabatic approximation [Chew, Goldberger, and Low, 1956]. We limit ourselves here to a brief description of the three wave modes in the classical collision dominated MHD plasma theory. This approach is adopted for four reasons: (1) plasma instabilities and the presence of the magnetic field effectively replace particle-particle collisions in giving the plasma the collective bulk properties of a fluid; (2) the experimental data to be considered satisfy the hydromagnetic condition as defined above; (3) the MHD approach has been used with reasonable success in the past in connection with interplanetary shocks and the earth's bow shock; (4) MHD wave theory is relatively simple, and seems adequate to describe the observed wave properties of the medium.

In the isotropic MHD approximation there are three distinct wave modes -- the Alfvén, the fast, and the slow, with frequencies ω_A, ω_+, and ω_-, respectively. If $\underset{\sim}{B}_o$ is the static background field, $\underset{\sim}{k}$ the propagation vector of the wave, and θ the angle between $\underset{\sim}{B}_o$ and $\underset{\sim}{k}$, then the dispersion relations for these three modes are given [Thompson, 1962] by

$$\omega_A^2 = (\underset{\sim}{k} \cdot \underset{\sim}{B}_o)^2/4\pi\rho_o \tag{1}$$

$$\omega_\pm^2 = (k^2/2)\left\{(V_S^2 + V_A^2) \pm \left[(V_S^2 + V_A^2)^2 - 4V_S^2 V_A^2 \cos^2\theta\right]^{\frac{1}{2}}\right\} \tag{2}$$

where $V_A = B_o/(4\pi\rho_o)^{\frac{1}{2}}$ is the Alfvén velocity, ρ_o is the mass density, and V_S is the speed of sound. For the solar wind, V_A and V_S are both

typically of the order of 50 km/sec. The Alfvén mode is purely transverse, and is characterized by constant density and field strength and by velocity and magnetic field perturbations $\underset{\sim}{v}$ and $\underset{\sim}{b}$, respectively, that are perpendicular to the plane of $\underset{\sim}{B}_o$ and $\underset{\sim}{k}$. Thus $\underset{\sim}{b}$ and $\underset{\sim}{v}$ are parallel (or anti-parallel), and are connected by

$$\underset{\sim}{b} = \pm D_A \underset{\sim}{v} \tag{3}$$

where

$$D_A = B_o/V_A = (4\pi\rho_o)^{\frac{1}{2}} \tag{4}$$

and the sign in Equation (3) is the sign of $-\underset{\sim}{k} \cdot \underset{\sim}{B}_o$. Both the fast and slow modes (with $\theta \neq 0$) are associated with fluctuations in density and field strength; variations in field strength are in phase with those in density for the fast mode, and 180^o out of phase for the slow mode. The fluctuations $\underset{\sim}{b}$ and $\underset{\sim}{v}$ are in the plane of $\underset{\sim}{k}$ and $\underset{\sim}{B}_o$, with $\underset{\sim}{b}$ normal to $\underset{\sim}{k}$ in this plane. The perturbation $\underset{\sim}{v}$ is connected to $\underset{\sim}{b}$ by a linear tensorial relationship, in general is not parallel to $\underset{\sim}{b}$, and the ratio of the magnitude of $\underset{\sim}{b}$ to that of $\underset{\sim}{v}$ is

$$D_\pm = B_o \left(|k|/\omega_\pm\right) \sin\varphi \tag{5}$$

where φ is the angle between $\underset{\sim}{v}$ and $\underset{\sim}{B}_o$, and $\omega_\pm$ is given by (2). The detailed equations may be found in Coleman [1967]. For the singular case in which $\underset{\sim}{k}$ is colinear with $\underset{\sim}{B}_o$, the three modes reduce to two simple, orthogonal Alfvén modes, each characterized by Equations (3) and (4), and a pure acoustic mode in which there is no magnetic perturbation.

Equations (1) through (5) above apply to isotropic plasmas. For future reference, we note that for an Alfvén wave in an aniso-

tropic plasma such as the solar wind, Equation (4) becomes

$$D_A = \Theta_A (4\pi\rho_o)^{\frac{1}{2}} \tag{6}$$

where

$$\Theta_A = \left[1 - \frac{4\pi(p_{\|} - p_{\perp})}{B_o^2}\right]^{-\frac{1}{2}} \tag{7}$$

and $p_{\|}$ and $p_{\perp}$ are the pressures parallel and normal to $\underset{\sim}{B}_o$, respectively [Parker, 1957]

2. Discontinuities

Discontinuities in the isotropic MHD approximation are most conveniently treated in a frame in which the plane of the discontinuity is at rest. The Rankine-Hugoniot conservation equations must hold across the discontinuity, and solutions to these equations [Landau and Lipshitz, 1962] are of two types:

(1) Non-propagating. This category includes the contact and the tangential discontinuities. The contact discontinuity is simply the boundary between two media at rest which have different densities and temperatures; the magnetic field and the kinetic pressure are continuous across the discontinuity. The tangential discontinuity is the boundary between two streaming media. The velocity and magnetic field are tangential on both sides of the discontinuity, and can have any change in both magnitude and direction. The total pressure (kinetic plus magnetic) is conserved across the discontinuity, and the discontinuity does not propagate with respect to either media.

(2) Propagating. This category includes the fast and slow shocks, and the rotational discontinuity (sometimes called the Alfvén shock). In the limit of small amplitudes, these discontinuities pro-

pagate at the fast magnetoacoustic, slow magnetoacoustic, and Alfvén velocities, respectively. The rotational discontinuity may be thought of as a sharply crested Alfvén wave. Fast and slow shocks are rarely observed in the solar wind, and we will not treat them further here. The basic discontinuities with which we are concerned are thus the contact, the tangential, and the rotational.

C. The Interpretation of Spacecraft Data

There are well-known difficulties in the interpretation of spacecraft data. The plasma is convected past the spacecraft with a velocity (~400 km/sec) that is high compared to the characteristic MHD propagation speeds (~50 km/sec). Thus, all MHD disturbances are convected outward whatever their true direction of propagation in the rest frame of the plasma. Observed variations are primarily due to the convection past the spacecraft of spatial structures which may be either static and "frozen-in" or dynamic and slowly propagating. In the frame of the wind, the two classes of structures have substantially different properties, different origins, and different physical natures; in the spacecraft frame, they may be quite difficult to distinguish on the basis of either magnetometer or plasma data alone. As we shall see, an identification can usually be made on the basis of a careful study of both magnetic field and plasma data. Throughout, we use the term wave in a broad sense. In many instances the terms Alfvénic turbulence or rotational discontinuity might be more appropriate, although neither is fully descriptive of the phenomenon. In all cases, the term wave is used to apply to dynamic, non-shock struc-

tures, almost always non-sinusoidal and nonperiodic, which propagate in the rest frame of the solar wind.

Unless otherwise specified, time and frequencies given hereafter refer to the spacecraft frame; these must be Doppler shifted to yield wavelengths and frequencies in the rest frame of the wind. For example, a wave structure propagating outward from the sun with the Alfvén velocity V_A superposed on the wind velocity V_W and having an apparent period T in the spacecraft frame has a wavelength of $T(V_W + V_A)$ and period of $T\left[(V_W/V_A) + 1\right]$ in the rest frame of the wind. The fine scale structure we are concerned with has characteristic scales of .01 a.u. and less; this corresponds to periods in the spacecraft frame of one to two hours and less.

CHAPTER II

DATA REDUCTION

A. Recovery of the Basic Magnetic Field Data

1. Master Data Library Tapes

Mariner 5 (Venus 1967) was in operation from June 14, 1967, to November 22, 1967. Magnetic field measurements were made by a low-field, vector, helium magnetometer [Connor, 1968]. Three triaxial field samples were obtained every 12.6 seconds at the high data rate, and every 50.4 seconds at the low data rate. The high data rate period extended from the beginning of the mission until July 24, 1967, after which time data were taken at the low rate; there are approximately 40 days of high rate data and 120 days of low rate data.

The first step in the analysis of the Mariner 5 data was the reduction of the raw magnetometer data to a form which could be used conveniently. The basic source of data for the Mariner 5 experiment is the Master Data Library (MDL) tapes. These tapes are provided by the Jet Propulsion Laboratory, and contain the entire telemetry stream from the spacecraft. The basic data sampling sequence is called a frame, and consists of a number of individual measurements for each experiment on board. The real time sampling length of the frame is 12.6 (50.4) seconds at the high (low) rate, and each frame has one time associated with it. Three vector readings of the magnetic field are returned per frame; they are spaced 1/7, 2/7, and 4/7 of the frame length after the beginning of the frame. The three components of the field are measured in an XYZ spacecraft body-fixed

cartesian coordinate system. The attitude control jets in conjunction with sun and Canopus sensors keep the Z axis oriented along a radial line from the spacecraft to the sun, with the spacecraft/Canopus angle at -45^{o} from the X-axis in the XY plane.

Measurements of the field components are returned in digital units (DN) in the range from +511 to -511. The conversion function from DN to gamma is very nearly linear with approximately .4γ per DN. Once every 2048 frames there is a 24 frame calibration sequence during which known fields of approximately $\pm 40\gamma$ and $\pm 80\gamma$ are produced at the position of the magnetometer; this calibration insures the reliability of the DN to gamma conversion. Using a fortran program XRPM provided by JPL, the magnetometer digital readings in each frame, along with the frame time and various quality control words were read from the eleven MDL tapes comprising the Mariner 5 mission and written on two intermediate tapes, called MARDI tapes. The MARDI tapes were then processed through various phases which successively: (1) converted DN measurements to gamma; (2) removed the calibration offsets so as to recover data during this sequence; (3) provided quality tags for each individual vector reading based on the number of bit errors in the telemetry stream for the frame and the consistency of that reading (within broad ranges) as compared to adjacent measurements.

2. Spacecraft Field Corrections

An extensive analysis of good quality data on the MARDI tapes was carried out to determine the spacecraft magnetic field [Davis and

Smith, 1968]. Magnetometer readings $\underset{\sim}{M}$ are the sum of two vectors

$$\underset{\sim}{M} = \underset{\sim}{B} + \underset{\sim}{S}$$

where $\underset{\sim}{B}$ is the true interplanetary magnetic field (often rapidly varying) and $\underset{\sim}{S}$ is the (unknown) spacecraft field (usually constant or only slowly varying). Mathematically, $\underset{\sim}{S}$ is chosen so as to minimize the high frequency variance in $|\underset{\sim}{M}|$ during selected intervals. The method is based on the fact that previous experiments have shown the fine scale fluctuations in the interplanetary field to be primarily changes in direction, with relatively small changes in field strength. An appreciable error in the spacecraft field estimate for a given component will cause purely directional fluctuations to produce apparent field strength fluctuations. This fact, coupled with the above comment as to the nature of the variations, enables an inflight determination of the spacecraft field to be made. We subsequently show that this method is quite reasonable in view of the predominant physical nature of the fine scale field fluctuations. The spacecraft field correction used for Mariner 5 is on the order of 10γ in magnitude and is considered reliable within $.25\gamma$ on each component. With the exception of five isolated points, the spacecraft field estimate was never changed more than once per day, with at most $.06\gamma$ per axis shift from one day to the next. In most of these five exceptional cases, there was a significant change in the mode of operation of the spacecraft that could have caused the change in zero offset. Subtraction of the spacecraft field from the XYZ magnetometer measurements gives the true interplanetary magnetic field $\underset{\sim}{B}$.

3. RTN Coordinates and the BAMFAT Tape

Using trajectory and spacecraft orientation information provided by JPL, the field vectors $\underset{\sim}{B}$ were rotated from the XYZ system to orthogonal RTN solar polar coordinates, defined as follows: the positive R direction is radially outward from the sun; the T direction is parallel to the solar equatorial plane and positive in the direction of planetary motion, and the N direction is northward along $\underset{\sim}{R} \times \underset{\sim}{T}$ so that RTN is right-handed. The RTN field components of the vectors, with times and quality tags, were then written on the Basic Magnetic Field Analysis Tape (BAMFAT). One tape contains the entire mission, both high and low data rate. The basic unit is still one data frame, packed into five 36 bit words, with 128 frames per BAMFAT record; spacecraft trajectory information is written once per record. The BAMFAT tape contains on the order of 300,000 good quality measurements of the interplanetary magnetic field.

B. Plasma Data and Magnetic Field Averages

The plasma probe on board Mariner 5 was flown by the MIT plasma group, who have generously provided extensive and detailed data from their experiment. The plasma detector, a modulated grid Faraday cup [Lazarus, et al., 1967] points at the sun and measures positive ion currents in 32 energy levels covering the range from 40 to 9400 ev, with a complete sampling cycle of about 5.04 min at the high data rate and 20.16 min at the low. This includes a directional measurement from which the three components of the wind velocity can be deduced based on currents to four subsections of the

collector cup. From the energy spectrum, Bridge and Lazarus obtain estimates of N, the proton number density in cm^{-3}, $\underset{\sim}{V}$, the vector bulk velocity of the solar wind protons, in km/sec, and V_T, the most probable proton thermal speed $(2kT_p/m_p)^{\frac{1}{2}}$, in km/sec. The plasma probe sampling sequence takes exactly 24 frames, and thus spans 72 vector measurements of $\underset{\sim}{B}$. These magnetometer measurements are averaged, and a merged plasma-field tape written containing all of the above plasma parameters and averages of magnetic field components and magnitudes over the plasma probe sampling period.

Using only good quality data from the BAMFAT tape, we also compute averages and variances of the field data over intervals of 168.75 sec (2^{-9}day), 22.5 min (2^{-6}day), 3 hr (2^{-3}day), and one day. For each interval, $\langle \underset{\sim}{B} \rangle$, $\langle | \underset{\sim}{B} | \rangle$, and the matrix $\underset{\sim}{S}$ defined by

$$S_{ij} = \langle B_i B_j \rangle - \langle B_i \rangle \langle B_j \rangle$$

are calculated, where $\langle\ \rangle$ denotes averaging over the specified time interval. This information is stored on magnetic tape.

C. Plots of Magnetic Field and Plasma Data

The Mariner 5 magnetic field data described above contain fluctuations with characteristic times from 10 to 10^6 sec. One of the most important steps in the data reduction is the choice of time scales for data display, since vastly different physical processes occur across the five orders of magnitude in time resolution. The magnetic field data are plotted on four time scales: (1) one or

three hours per plot, using the basic BAMFAT data; (2) one day per plot, using the 168.75 sec. averages; (3) seven days per plot, using the 22.5 min. averages; (4) twenty-seven days per plot, using the three hour averages. The plasma parameters N, V_T, and V are plotted on scales of one day per plot, seven days per plot, and twenty-seven days per plot. Figures 1a through 1e show examples of these plots for each period. Note that the same data appear quite different on the various time scales. A wide range of time scales for data display is absolutely essential to the interpretation of interplanetary data.

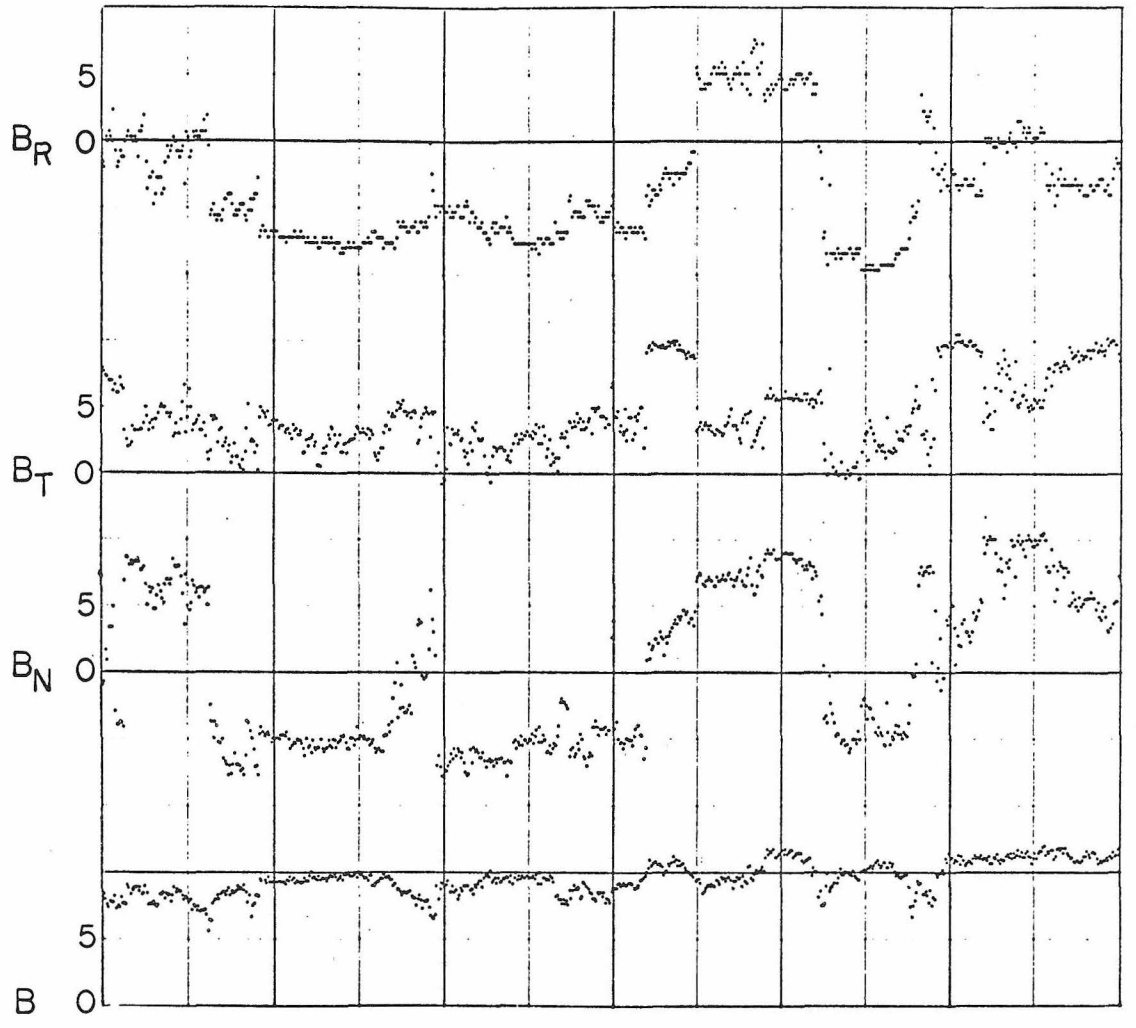

Figure 1a. Three hours of basic magnetometer data from day 228 (9-12). This is during the low data rate part of the mission, so that readings are taken once in approximately 16 sec. B_R, B_N, and B_T are solar polar components, and B is the field magnitude.

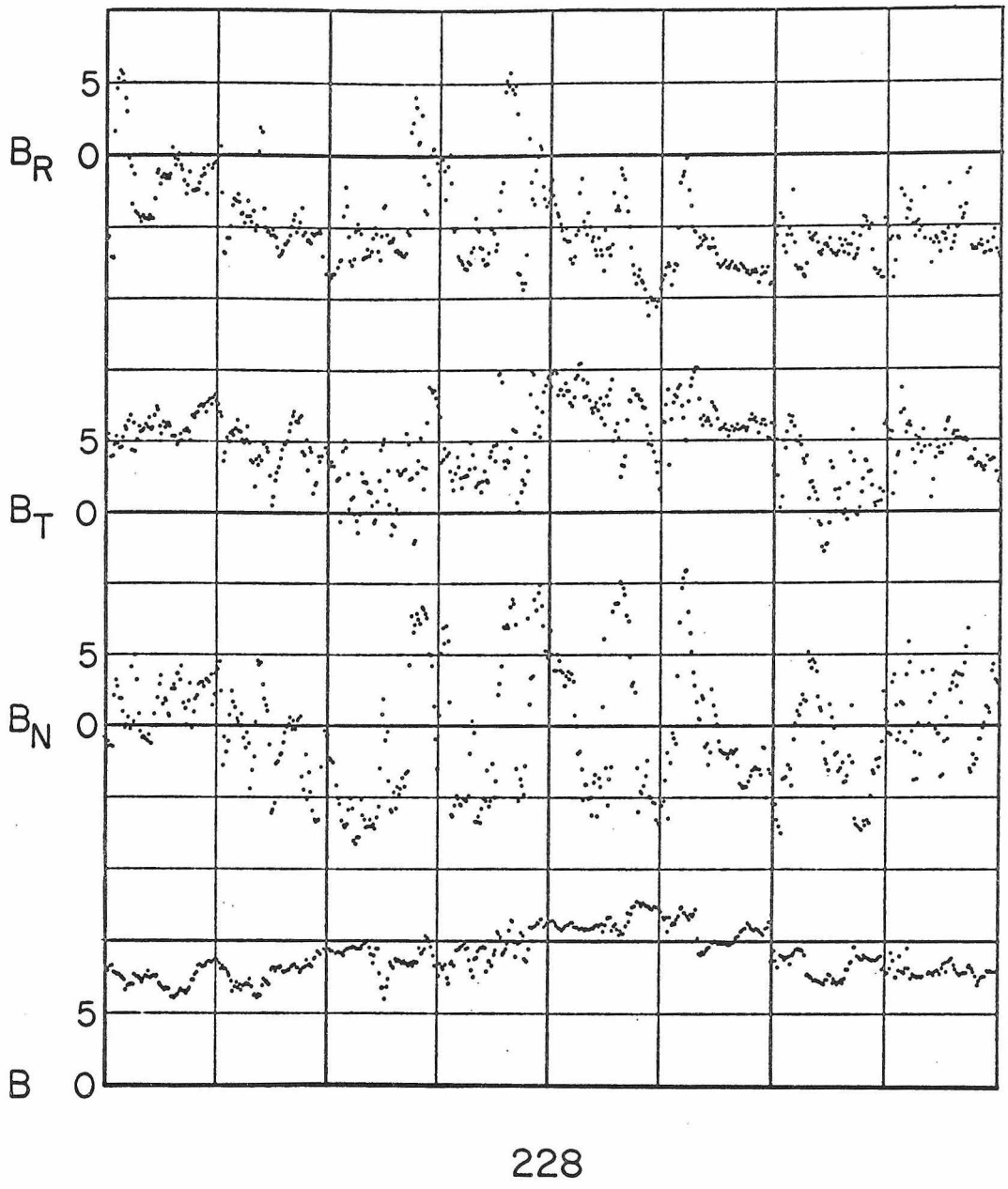

Figure 1b. One day of magnetic field data plotted using 168.75 sec averages of the individual vector measurements.

Figure 1c. Seven days of magnetic field data plotted using 22.5 minute averages. BE and LA are magnetic field direction angles (in degrees). BE is the angle out of the solar equatorial plane (-90^{o} to 90^{o}) and LA is the field angle in this plane measured from an idealized 45^{o} spiral field direction. A dark bar indicates this direction is outward along the 45^{o} spiral, and the absence of a bar indicates this direction is inward along the spiral. BR, BT, BN are RTN solar polar field components and BA is the average field strength.

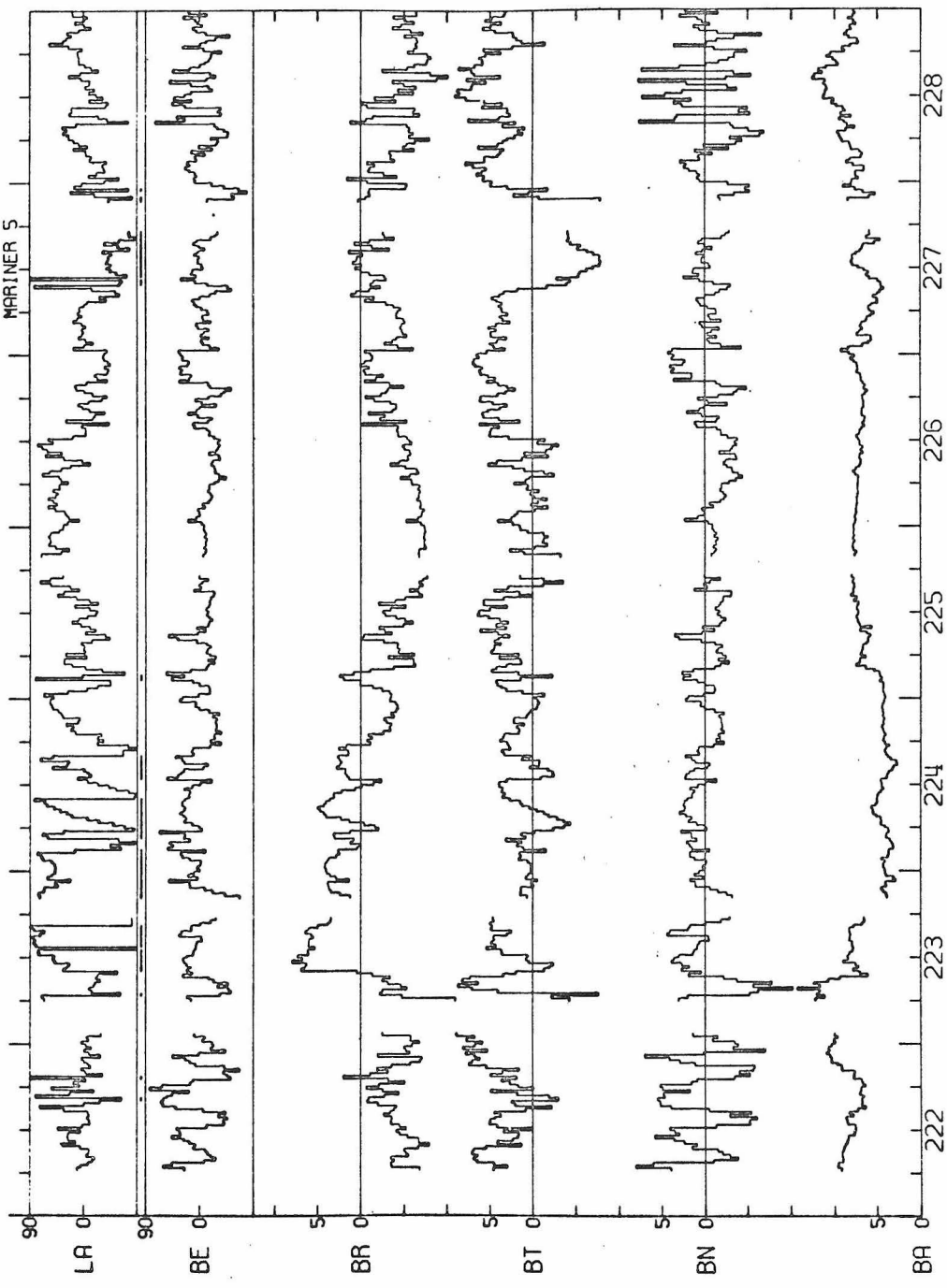

Figure 1c

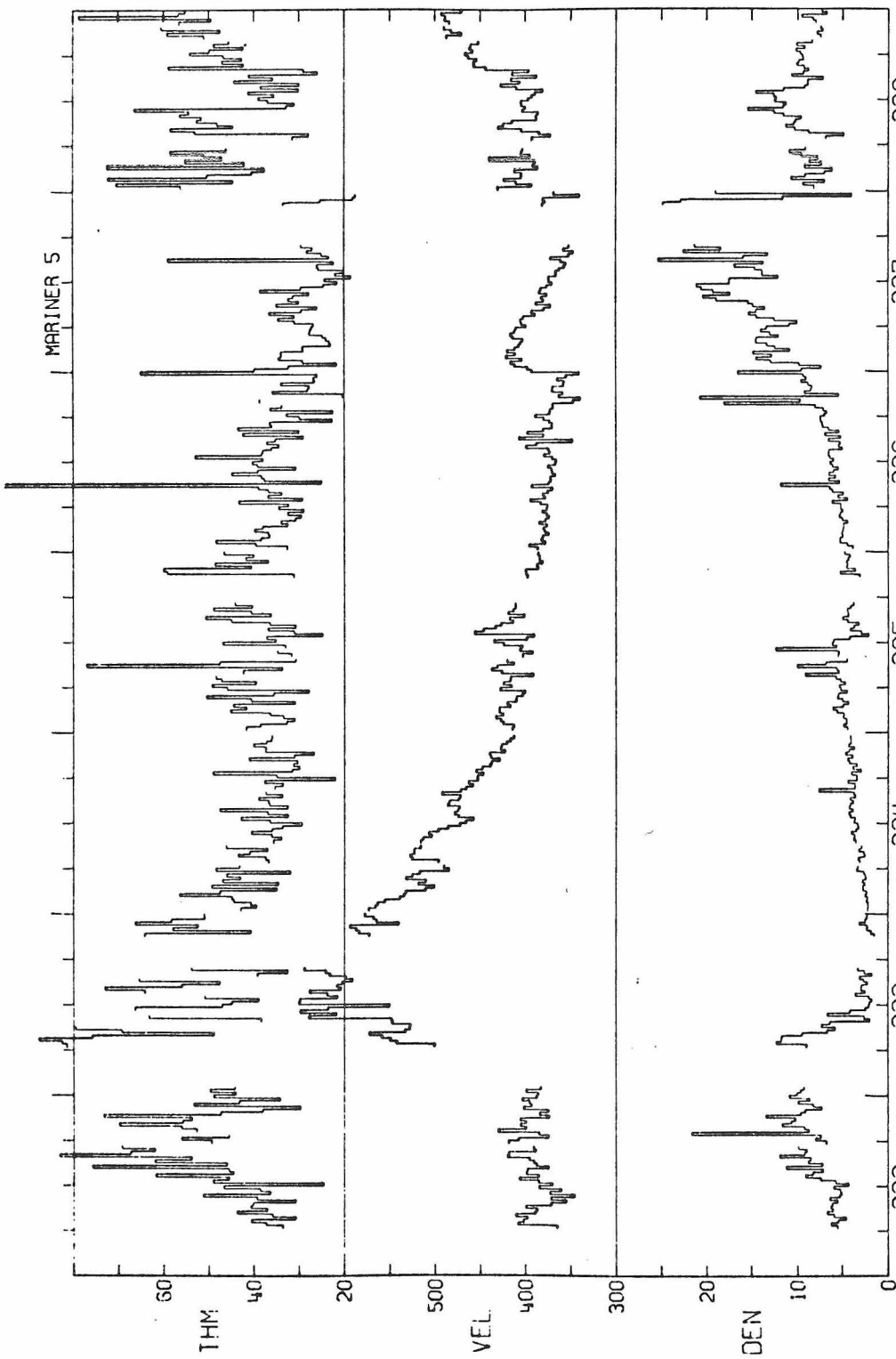

Figure 1d. Seven days of plasma data (the proton thermal velocity, the solar wind speed, and the proton number density) plotted using approximately 22.5 minute averages.

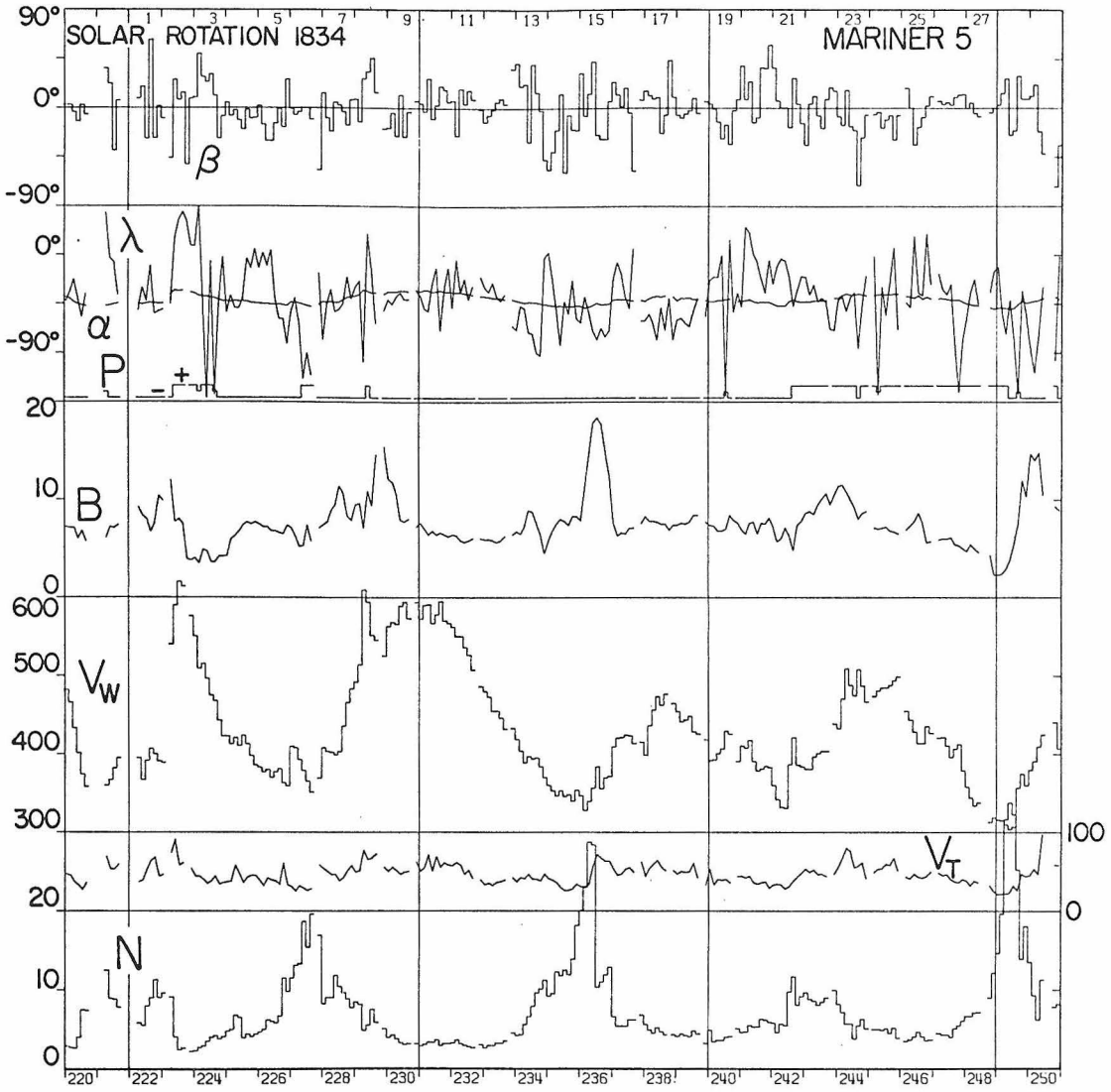

Figure 1e. One solar rotation plotted using three hour averages. B is the magnetic field strength, N is the proton number density, V_W is the solar wind velocity, and V_T is the proton thermal speed. β and λ are field direction angles. β is the field angle out of the solar equatorial plane, and λ is a longitudinal angle in this plane measured from the R axis. P is the polarity, and indicates whether the field has a positive component along a 45^0 spiral angle direction (+) or not (-). α is the theoretical spiral field angle computed with the three hour average wind velocity.

CHAPTER III

OBSERVATIONS

A. Identification of the Alfvén Wave Mode

1. Vector Correlations

When interplanetary magnetic field data were first obtained more than eight years ago, the microscale structure was found to be quite irregular, and it seemed plausible [Davis, 1966] that many of the features were propagating Alfvén or magnetoacoustic waves. Coleman [1967] carried out an extensive spectral and cross-spectral analysis of Mariner 2 (Venus, 1962) plasma and field data, and concluded that Alfvén waves propagating away from the sun in the rest frame of the wind might account for a substantial fraction of the fluctuations with periods in the spacecraft frame from 10 to 10^4 seconds. This statistical analysis did not give patterns of occurence of the waves or explicit examples of the wave forms. The only example in which such waves were specifically identified was in a two hour segment of Mariner 2 data where Unti and Neugebauer [1968] demonstrated the existence of a quasi-sinusoidal Alfvénic waveform with a period in the spacecraft frame of about 30 minutes. Belcher, Davis, and Smith [1969], in a preliminary analysis of Mariner 5 plasma and field data, identified outwardly propagating Alfvénic wave trains as frequently occurring phenomena, although they are for the most part non-sinusoidal and aperiodic.

Figure 2a is an example of such a wavetrain, approximately 1/4 a.u. in length. The variations in the components of the magnetic

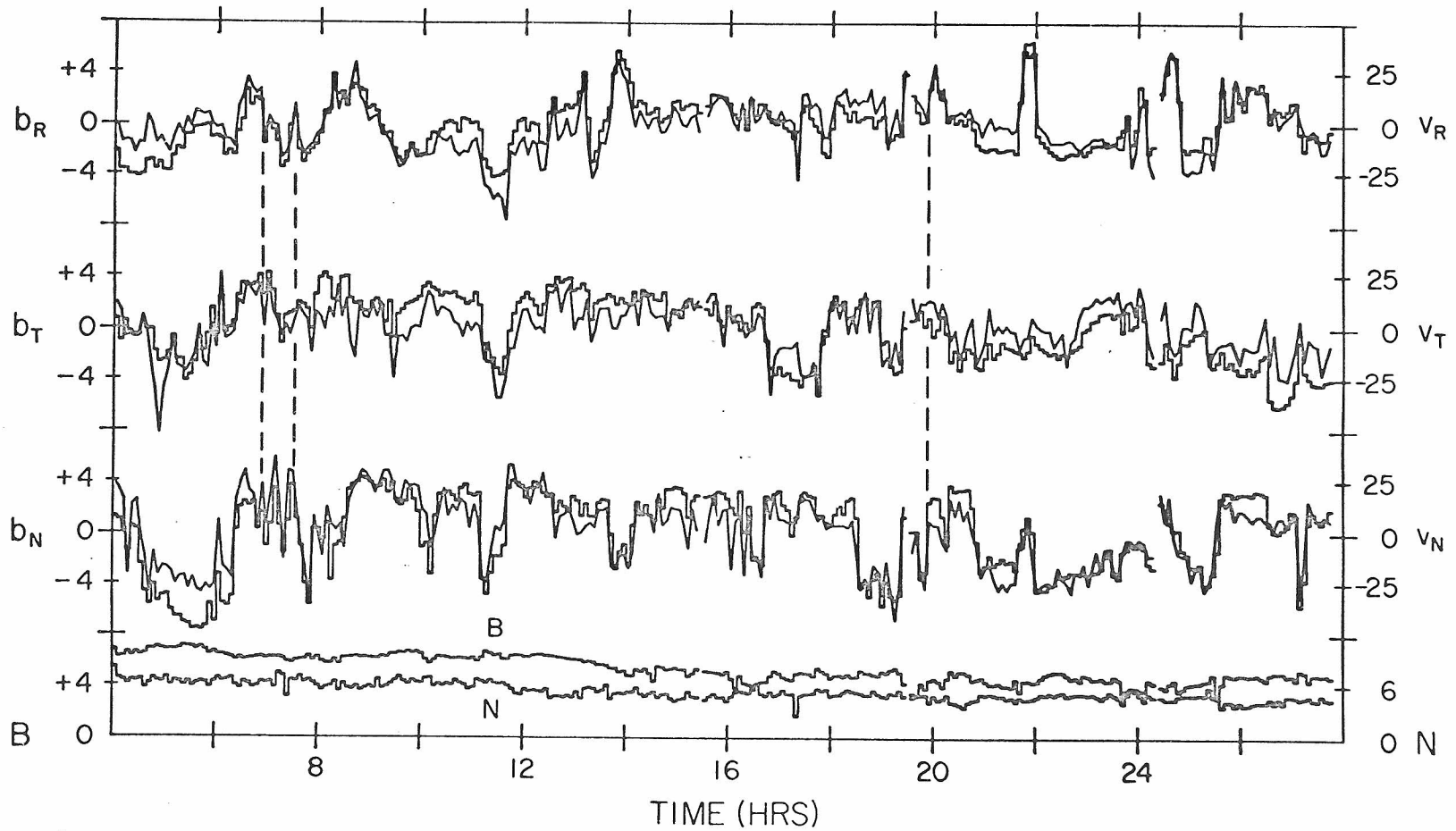

Figure 2a. Twenty-four hours of magnetic field and plasma data demonstrating the presence of nearly pure Alfvén waves. The upper six curves are 5.04 min. bulk velocity components in km/sec (diagonal lines) and magnetic field components averaged over the plasma probe sampling period, in gamma (horizontal and vertical lines). The two lower curves are magnetic field strength and proton number density.

field $\underset{\sim}{B}$ and the plasma velocity $\underset{\sim}{V}$ for a 24 hour period starting at 0400 on day 166 are shown. For each component, the average of that component over the 24 hour period has been subtracted; thus, the plots show the fluctuations about the average ($\langle B_R \rangle = -1.9\gamma$, $\langle B_T \rangle = 1.4\gamma$, $\langle B_N \rangle = 1.2\gamma$, $\langle V_R \rangle = 427$ km/sec; $\langle V_T \rangle$ and $\langle V_N \rangle$ have not yet been corrected for aberration due to the spacecraft motion). The two lower curves on the plot are proton number density N and magnetic field strength B($\langle B \rangle = 5.3\gamma$, $\langle N \rangle = 5.4$ cm^{-3}). The Alfvénic identification is based primarily on the fact that the vector relation between $\underset{\sim}{b}$ and $\underset{\sim}{v}$ given by Equation (3) ($\underset{\sim}{b} = \pm D_A \underset{\sim}{v}$) is satisfied. This period is one of the better examples of the waves and illustrates their most characteristic features -- close correlation between $\underset{\sim}{b}$ and $\underset{\sim}{v}$, variations in $\underset{\sim}{b}$ comparable to the field strength, and relatively little variation in field strength or density, as is expected for the transverse Alfvén mode. The fluctuations in Figure 2a must be predominantly Alfvénic, since if there were a substantial admixture of the fast or slow magnetoacoustic modes, there would be variations in field strength correlated with variations in the density as well as with other quantities. In this case, the average magnetic field is inward along the spiral and the correlation between $\underset{\sim}{b}$ and $\underset{\sim}{v}$ is positive; when the magnetic field is outward, the correlation in periods of good waves is negative. This indicates outward propagation (see Equation (3)).

The scale ratio used for plotting the magnetic field and velocity variations in Figure 2a corresponds to a value of D_A^{-1} in

Equation (3) of 6.4 km sec^{-1}/gamma. This was determined by the condition that when this ratio is used for a fixed area plot of v_R versus b_R for all the data, the sum of the squares of the perpendicular distances from the points to a line of unit slope is minimized. (Mathematically this gives $D_A^{-1} = \sigma v_R / \sigma b_R$, the ratio of the standard deviations.) The average values of N and N_α (the alpha particle number density) during this period are 5.4 cm^{-3} and 0.4 cm^{-3}, respectively; Equation (6) with $\Theta_A = 1$ gives $D_A^{-1} = 8.2$ km sec^{-1}/gamma. We feel that the discrepancy between this predicted value and the observed value of 6.4 is significant and probably is due to the anisotropy in the pressure. This requires that $4\pi(p_{\|}-p_{\perp})/B_o^2$ be 0.40. The average during this period of $(2kT_p/m_p)^{\frac{1}{2}}$, the most probable proton velocity, was observed to be 47 km/sec, which corresponds to $4\pi p_p/B_o^2 = 0.5$, where p_p is the mean proton pressure. With reasonable values of the electron and alpha pressures and of the pressure anisotropy [Hundhausen et al., 1967], the required value of Θ_A seems entirely reasonable. On other occasions when $\beta = 8\pi p_p/B_o^2$ is smaller, values of Θ_A closer to unity would be expected.

2. Waves Versus Discontinuities

Figure 2b is an exanded plot of three particular ten minute periods indicated on Figure 2a, where the crosses are the basic magnetometer data (one reading in approximately four seconds) and the lines are the plasma data (one per 5.04 min), scaled in the same ratio as in Figure 2a. On this time scale, the waves may be either

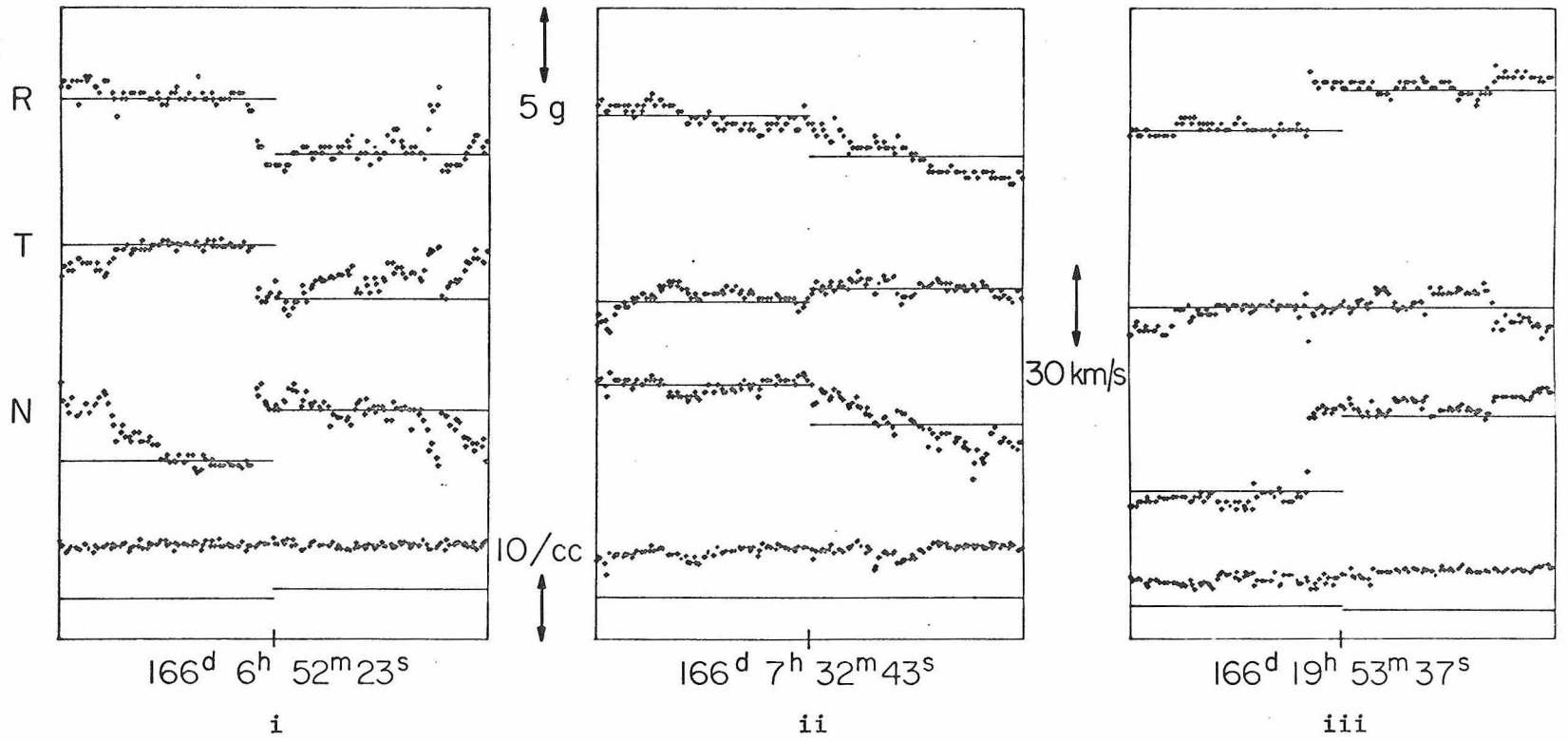

Figure 2b. Expanded plots of three ten minute intervals as indicated in Figure 2a, showing the high frequency magnetic field fluctuations (crosses) and the 5.04 minute plasma readings (bars). The lower two curves are field strength and proton number density, and the upper six curves are bulk velocity and field components.

gradual (2b, ii) or discontinuous (2b, i; 2b, iii), with abrupt changes within 4 seconds. As discussed below, we feel that all three examples are Alfvénic, with continuous magnetic field lines, but with a discontinuity in direction in cases (2b, i) and (2b, iii). Such abrupt changes occur at a rate of about one per hour, and are enmeshed in more gradual changes.

The visual appearance of the field fluctuations is qualitatively different on the time scales of Figures 2a and 2b. With the scale used in Figure 2b, the most prominent structures are the abrupt changes which tend to be preceded and followed by field values that appear nearly constant. For example, the structure in Figure (2b, i) is more striking than that in (2b, ii) even though both have about the same total change over the ten minute period, and both appear very similar in Figure 2a. On the time scale of Figure 2a, the genuine high frequency abrupt changes do not stand out because they are indistinguishable from large smooth changes when the data are averaged over 5.04 minute intervals, and because the field no longer appears to remain steady before and after the jumps. Because the abrupt changes are the most visually striking features when field data are plotted at a high time resolution, even though they are relatively infrequent and not necessarily intrinsically different from the smoother variations, numerous studies have been made of their structure and frequency of occurrence [Siscoe et al., 1968, Burlaga, 1968, 1969]. These authors have tentatively concluded that most of the discontinuities in the solar wind are tangential (non-propagating). In

fact, it has been suggested [Ness, 1969] that the fluctuations in Figure 2a are not dynamic structures propagating in the rest frame of the solar wind, but rather are an ensemble of spatially convected non-propagating MHD discontinuities in equilibrium. Since this point is of major importance in the interpretation of interplanetary magnetic field fluctuations, we discuss it in some detail.

Consider the two non-propagating discontinuities in the isotropic MHD approximation, the contact and the tangential, as discussed in I B above. The magnetic field is continuous across the contact surface, which is of no interest to us, but both plasma and field parameters can change across the tangential discontinuity. Let n and t be subscripts denoting components normal and tangential, respectively, to the discontinuity surface and let [A] denote the change in A across the surface. A tangential discontinuity is characterized by $B_n = 0$, $V_n = 0$, arbitrary and unrelated $[\underset{\sim}{V}_t]$ and $[\underset{\sim}{B}_t]$, and any change in pressure and field strength subject to the condition $[p + B^2/8\pi] = 0$. By constructing a series of special tangential discontinuities, all having continuous density and field strength, with the plane of the discontinuity so chosen that $B_n = 0$ on both sides, and with $[\underset{\sim}{B}_t]$ and $[\underset{\sim}{V}_t]$ related by Equation (3) (where the sign is consistent from discontinuity to discontinuity and changes with the polarity), we can in fact make a structure such as in Figure 2a which is static. None of these special conditions are required, but they are allowed by the tangential discontinuity equations. However, it is not clear what physical mechanism would cause such a configuration in the first

place, and while it is possible to explain any one discontinuity in this way, it is hard to fit together a large number unless their shear planes are all parallel. On the other hand, the Alfvén wave hypothesis accounts for all of the observed properties in a straightforward manner. When sufficiently sharp-crested, an Alfvén wave can be termed a rotational discontinuity. Such a discontinuity has continuous density and field strength, B_n is non-zero and continuous, and $[\underset{\sim}{B}_t]$ and $[\underset{\sim}{V}_t]$ are related by Equation (3). The only special conditions needed to produce a data sequence as in Figure 2a is that all the Alfvén waves propagate outward.

The fluctuations in Figure 2a are thus viewed as purely Alfvénic, with occasional sharply crested Alfvén waves enmeshed in more gradual variations. This interpretation is in sharp contrast to the non-propagating, filamentary model of the microscale structure consisting of equilibrium regions of differing properties separated by tangential discontinuities and convected outward from the sun by the solar wind. Periods such as in Figure 2a are usually found in high velocity streams and on their trailing edges; they can last as long as three days ($\sim$ 7 a.u. of gas), and almost every discontinuity in that time appears to be a sharply crested Alfvén wave. We do not mean to imply that all discontinuities in the solar wind are Alfvénic, as this is obviously not the case, but it appears that a high percentage of them are, particularly in certain regions (as discussed below). Similarly, we feel that the filamentary or discontinuous model of the microscale structure is valid in many circumstances, but that it

must be applied with care. Even a tentative identification of structures as dynamic or static must include a careful study of both magnetic field and plasma data.

3. Frequency of Occurrence and Direction of Propagation

It should be emphasized that the presence of the waves is very common, and tends to dominate the microstructure of the interplanetary medium. There are a total of about 25 days (a day being 24 consecutive hours) from the 160 day mission during which the Alfvén waves are as "pure" as those in Figure 2a; such periods tend to occur in high velocity streams and on their trailing edges where typically the density is low and the temperature high. Other examples of the waves, in the presence of large scale velocity gradients, static structures, shocks, polarity reversals, etc., are less clean, but they are still recognizably present. The identification of the waves during such periods is based on a visual inspection of plots of simultaneous plasma and field data at high time resolution. Alfvén waves are adjudged to be present if there is substantial high frequency fluctuation in the magnetic field, a good high frequency correlation between B_R and V_R (low frequency correlations are influenced by slow linear trends), and relatively little high frequenty fluctuation in density and field strength. In the following, we will state whether Alfvén waves are present or not on the basis of such comparisons of plasma and field data, although such data will not always be reproduced.

To obtain a rough statistical measure of the prevalence of the

waves, we have examined the distribution of ρ, the correlation coefficient between B_R and V_R computed over six hour intervals throughout the entire mission. Six hour intervals dominated by outwardly propagating Alfvén waves will have high values of $|\rho|$, and ρ will have the same sign as -P, where P is the polarity of the average field direction (+1 for $\langle \underset{\sim}{B} \rangle$ outward along the spiral and -1 for $\langle \underset{\sim}{B} \rangle$ inward along the spiral). For the 416 six-hour intervals in the flight with more than 66 percent data return, 33 percent of the intervals had $|\rho| \geq .8$ and 55 percent had $|\rho| \geq .6$. The sign of ρ correlates extremely well with the polarity of the field. Table 1 lists the percentage of the six-hour intervals with $|\rho|$ in the indicated ranges for which ρP is negative. Those six-hour intervals (112 out of 416) for which $\langle \underset{\sim}{B} \rangle$ was not within 45° of a 45° spiral angle are not included because of their poorly defined polarity. All but three of the remaining six-hour intervals with $|\rho| \geq .8$ have $\rho P < 0$, indicating outwardly propagating waves. Inspection of the three six-hour intervals which are exceptions reveals that the high correlation and positive ρP are not caused by inwardly propagating waves, but by slow linear trends during quiet times; such trends can cause a spuriously high value of $|\rho|$ even when there are no wave-like or higher frequency fluctuations present. Thus, Alfvén waves in periods of high $|\rho|$ are essentially always outwardly propagating.

Periods for which $|\rho|$ is not as high ($|\rho| < .8$) have $\rho P < 0$ a large percentage of the time (see Table 1), but not as consistently as do periods of higher correlation. The smaller values of $|\rho|$ could be caused by the presence of static structures, shocks, slow linear

TABLE 1

Range of $\lvert\rho\rvert$	No. and percent intervals in this range	Percent intervals with $\rho P<0$
.0/.2	44 (14)	66
.2/.4	41 (14)	68
.4/.6	47 (15)	83
.6/.8	76 (25)	83
.8/1.0	96 (32)	97
.0/1.0	304 (100)	83

trends, etc., which can mask the effect of the correlation due to the waves. The intervals with $\rho P > 0$ could be due to linear trends that cause a high value of $|\rho|$ even when no waves are present. They could also be due to the presence of inwardly propagating Alfvén waves. Suppose that we are studying microscale fluctuations which are exclusively due to an outwardly propagating Alfvén wave of amplitude A_+ and an inwardly propagating Alfvén wave of amplitude A_-, with no cross correlation between the two waveforms; then it is easily shown that $\rho P = (A_-^2 - A_+^2)/(A_-^2 + A_+^2)$. For $A_-^2/A_+^2 = 1/9$, $\rho P = -.8$, for $A_-^2/A_+^2 = 1/3$, $\rho P = -.5$, and for $A_-^2/A_+^2 = 1$, $\rho P = 0$. Thus, the presence of inwardly propagating Alfvén waves can significantly reduce $|\rho|$ during periods of purely Alfvénic fluctuations, and it is possible that six-hour intervals for which $|\rho| \leq .8$ have inwardly propagating Alfvénic components, perhaps even with $A_-^2/A_+^2 > 1$ in many of the cases with $\rho P > 0$. The important point is that although inwardly propagating Alfvén waves may at times occur, they evidently never occur in an extremely pure form, since $|\rho| \geq .8$ implies $\rho P < 0$. Even though there may be periods in which there are both inward and outward Alfvén waves, there are no periods with exclusively inward propagation, whereas periods with exclusively outward propagation evidently occur on the order of 30 percent of the time.

It is clear from Table 1 that Alfvén waves propagating outward have a strong influence on the sign of ρ, even down to $|\rho| = .4$. This close correspondence between the sign of ρ and the polarity,

together with the high percentage of times with $|\rho| \geq .6$, strongly indicates that outwardly propagating Alfvén waves dominate the microscale structure about 50 percent of the time. Coleman [1967] found precisely the same type of correlation shown in Table 1 in a study of cross spectra between plasma and magnetic field data from Mariner II (Venus 1962), and also noted that this type of correspondence between ρ and P would be expected for outwardly propagating Alfvén waves. The waves were thus also present in appreciable quantities in the interplanetary medium in 1962.

B. Patterns of Occurrence of the Waves

1. Solar Wind Stream Structure

As noted above, Alfvén waves in the interplanetary medium have characteristic patterns of association with the large scale velocity structure of the solar wind. The macroscale properties of this stream structure were first discovered in the Mariner II data [Neugebauer and Snyder, 1966; Snyder et al., 1963], and subsequent probes have confirmed these initial results [Wilcox and Ness, 1965]. Although the high velocity streams observed by Mariner V are not as long lived as those found previously, the streaming patterns in the Mariner V data are very similar to those observed by earlier spacecraft, and exhibit the basic characteristics of fast and slow streams and their interactions. Figure 3 is a plot of three hour averages of various quantities over a 35 day period of the flight; V_w is the wind velocity, B is the magnetic field, N is the proton number density, and V_T is the most probable proton thermal

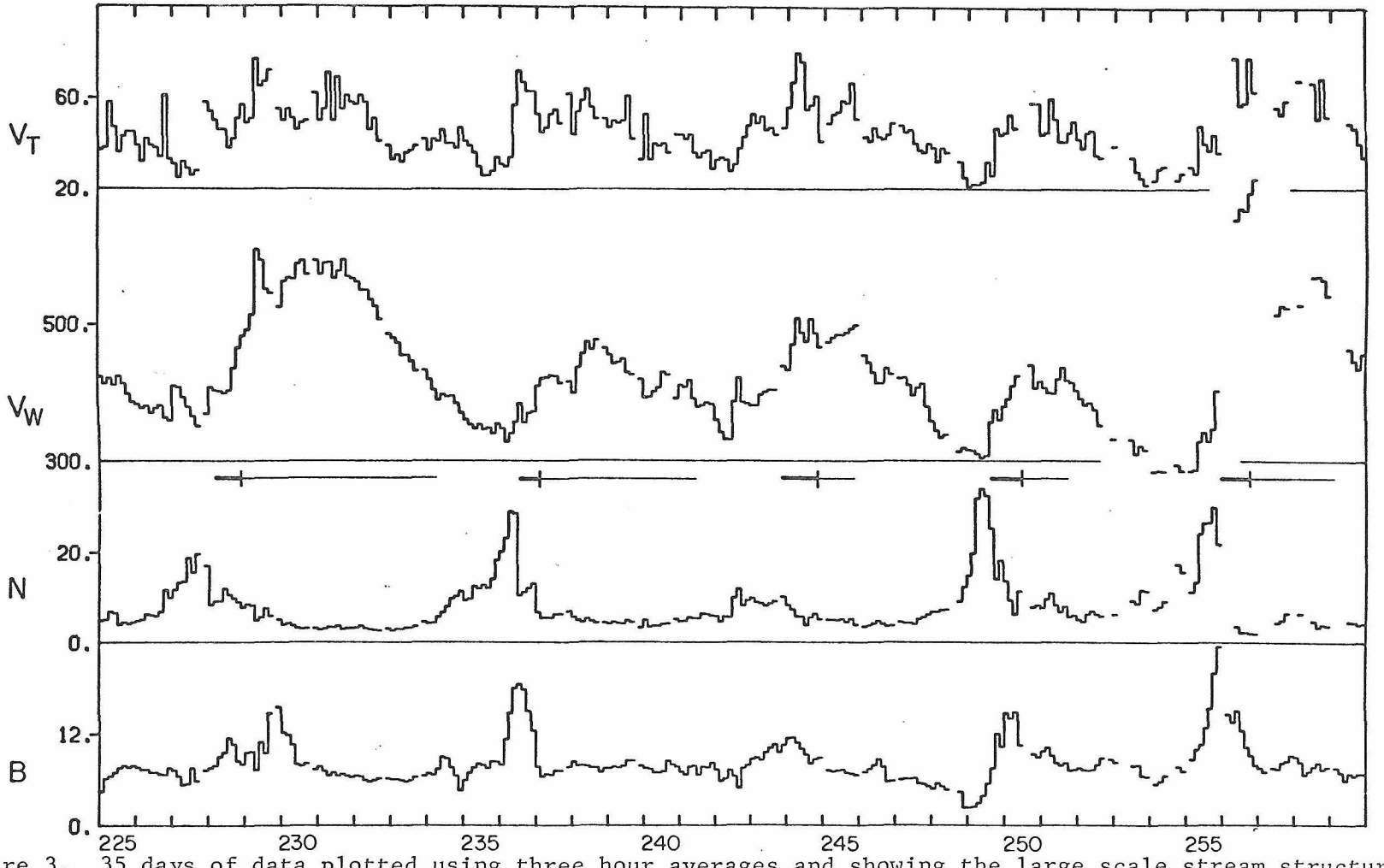

Figure 3. 35 days of data plotted using three hour averages and showing the large scale stream structure of the solar wind. B is in gamma, N is in particles per cubic centimeter, and V_W and V_T are in km/sec. The best examples of the Alfvén waves (light bars) are found in high velocity streams and on their trailing edges. The largest amplitude waves (heavy bars) are found at the leading edges of high velocity streams.

velocity $(2kT_p/m_p)^{\frac{1}{2}}$. High velocity regions in the solar wind tend to be hotter and less dense and low velocity regions colder and more dense. The level of high frequency magnetic field activity also tends to be higher in high velocity streams, although this effect is not as pronounced as the correlation between velocity and temperature. Magnetic field strengths tend to be the same in both high and low velocity regions, except for the high field regions found at the leading edges of fast streams where the velocity increases rapidly with time. In these regions, high velocity streams are overtaking and colliding with low velocity ones, causing local compression and consequent high magnetic fields and densities; there are usually enhanced temperatures and very high levels of magnetic field activity in these colliding stream regions [Davis et al., 1966; Davis, 1966]. The best examples (as in Figure 2a) of the purely Alfvénic, outwardly propagating magnetic field fluctuations are found in high velocity streams and on their trailing edges (where the velocity decreases slowly with time). Regions with waves of this nature are indicated by the light bars in Figure 3. Alfvén waves found in low velocity streams are also outwardly propagating, but tend to be of lower amplitude than those in the fast streams, and tend to be less pure in the sense that they are more strongly intermixed with structures of definitely non-Alfvénic character (such as tangential discontinuities). The largest amplitude Alfvénic fluctuations are found in the colliding stream regions. However, waves in these regions may have significant amounts of inwardly propagating or

non-Alfvénic components. Regions with very large amplitude waves are indicated by the heavy bars in Figure 3.

Figure 4 is a detailed specific example of large scale streaming properties using 40.3 minute averages plotted over a seven day period from day 189 to 195. σ_S is the square root of the 40.3 minute average of the total variance in the magnetic field components, in gamma, where the variances are computed over the plasma probe sampling period of 5.04 minutes, and the total variance is the sum of the variances on the individual axes. Gaps in the curves occur during periods when data were not taken. The region of rapid velocity increase at the leading edge of the high velocity stream extends from approximately the beginning to the end of day 192. It is preceded by relatively high densities, and is accompanied by enhanced temperatures and magnetic field fluctuations. The proton temperature and the standard deviations in field components are low in the low velocity stream, are at a maximum in the region of rapid velocity increase, and decrease with velocity on the trailing edge of the stream. The proton number density falls to very low values inside the high velocity stream proper (on day 193, for example) as compared to values in the low velocity stream (day 189). The density increase from day 189 to the end of day 190 is probably not associated with the compression or pileup of ambient slow gas ahead of the high velocity stream, since it is not accompanied by a field strength increase. The density increase is more likely a reflection of the observed fact that lower velocity streams have higher densities (note that the velocity is decreasing during this period). The density increase at the end

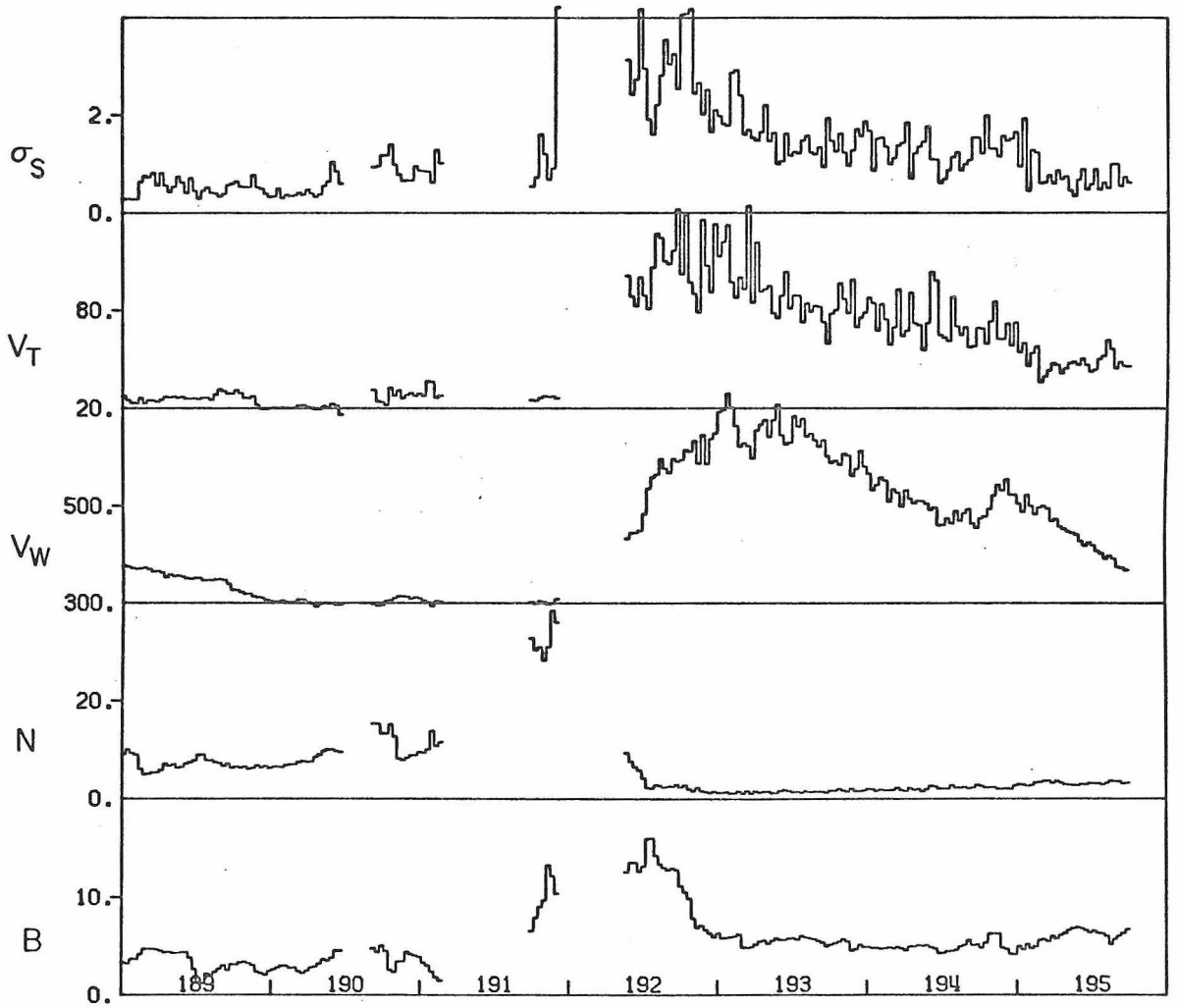

Figure 4. Seven days of Mariner V data plotted using 40.4 minute averages and showing a detailed stream-stream interaction. B, N, V_W, and V_T are as in Figure 3, and σ_S (in gamma) is the square root of the average over 40.4 minutes of the sum of the variances over 5.04 minutes of the R, T, and N field components.

of day 191 is accompanied by high field strengths, and thus is probably associated with compression of the slow gas ahead of the fast stream. The relatively higher field strengths and densities in the latter half of day 192 (as compared with day 193) are similarly the probable result of the deceleration and compression of the fast gas as it runs into the more dense slow gas. (Day 192, hours 15 to 18, has an average density and field strength of 2.6 cm^{-3} and 12.9 gamma, respectively, as opposed to average values of 1.3 cm^{-3} and 5.9 gamma on day 193, hours 0 to 3; although the field strength decrease in Figure 4 in the latter part of day 192 appears much larger than the density decrease, the relative change in the two quantities is the same.) In a later section we discuss further the dynamics of colliding stream structures.

Consider now the microscale fluctuations during this period. Their general level is indicated by the values of σ_S in Figure 4; their character is indicated by comparisons of $\underset{\sim}{v}$ and $\underset{\sim}{b}$ similar to Figure 2a. These are shown for the most interesting part of the interval in Figure 5, in which lower frequency variations have been eliminated from all but the lower curve by subtracting from each point a smoothed low frequency mean obtained by averaging over two hours about the point. The upper curves are thus high frequency variations about running two hour means. We emphasize that the vector velocity data given here are preliminary, and we present them only to demonstrate qualitative behavior. The variations in velocity have been multiplied by $(4\pi\langle N\rangle m_p)^{\frac{1}{2}}$ (See Equation (4)),

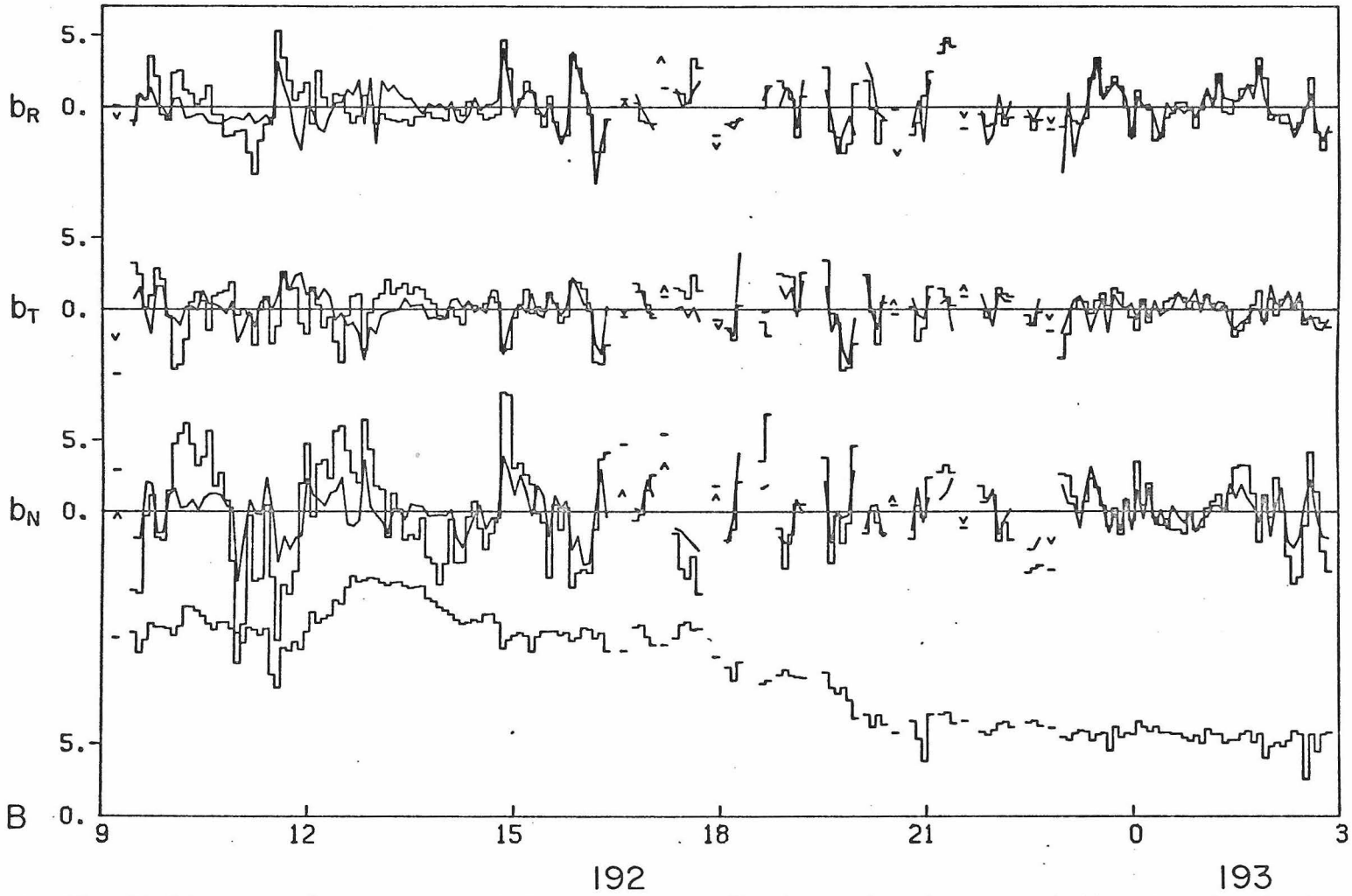

Figure 5. The field strength B and the field components (horizontal and vertical lines) and velocity components in gamma (diagonal lines) for an 18 hour period of Figure 4. Running two hour averages have been subtracted from all curves except B. B is here the magnitude of the 5.04 min average field vector.

where $\langle N \rangle$ is the smoothed proton number density for each point, in order to normalize them to the magnetic field variations. B is the magnitude of the average magnetic field before low frequency averages are subtracted. Days 189 through 191 are very quiet magnetically, with little wave-like fluctuations at high frequencies; however, after the beginning of day 192 there is a high level of wave activity that is seen in Figure 5 to become obviously Alfvénic with good correlations on all three axes after hour 15. The correlation between $\underset{\sim}{b}$ and $\underset{\sim}{v}$ is particularly impressive in view of the fact that the plasma data are probably highly alaised (changes in the plasma properties during the measurement of the energy spectrum) as there is a large amount of variation in the magnetic field with periods of less than five minutes, the plasma sampling period. For comparison Figure 6 is a point plot of 168.75 sec. averages of the magnetic field during days 192 and 193, showing more clearly the large amount of scatter in the field readings. The magnetic field variations in the compression region (before hour 21 in Figure 6) cannot be purely Alfvénic, since there are comparatively large fluctuations in B at higher frequencies. Even so, the power in the field magnitude at higher frequencies is small compared to the power in the field components, and the Alfvén mode is obviously still the dominant one. The polarity during this period is negative, and thus the very large amplitude higher frequency fluctuations (periods less than 2 hours) in the interaction region after hour 15 of day 192 are predominantly propagating outward. Before hour 15, in the most active part of the compression region, the correlations are clearly

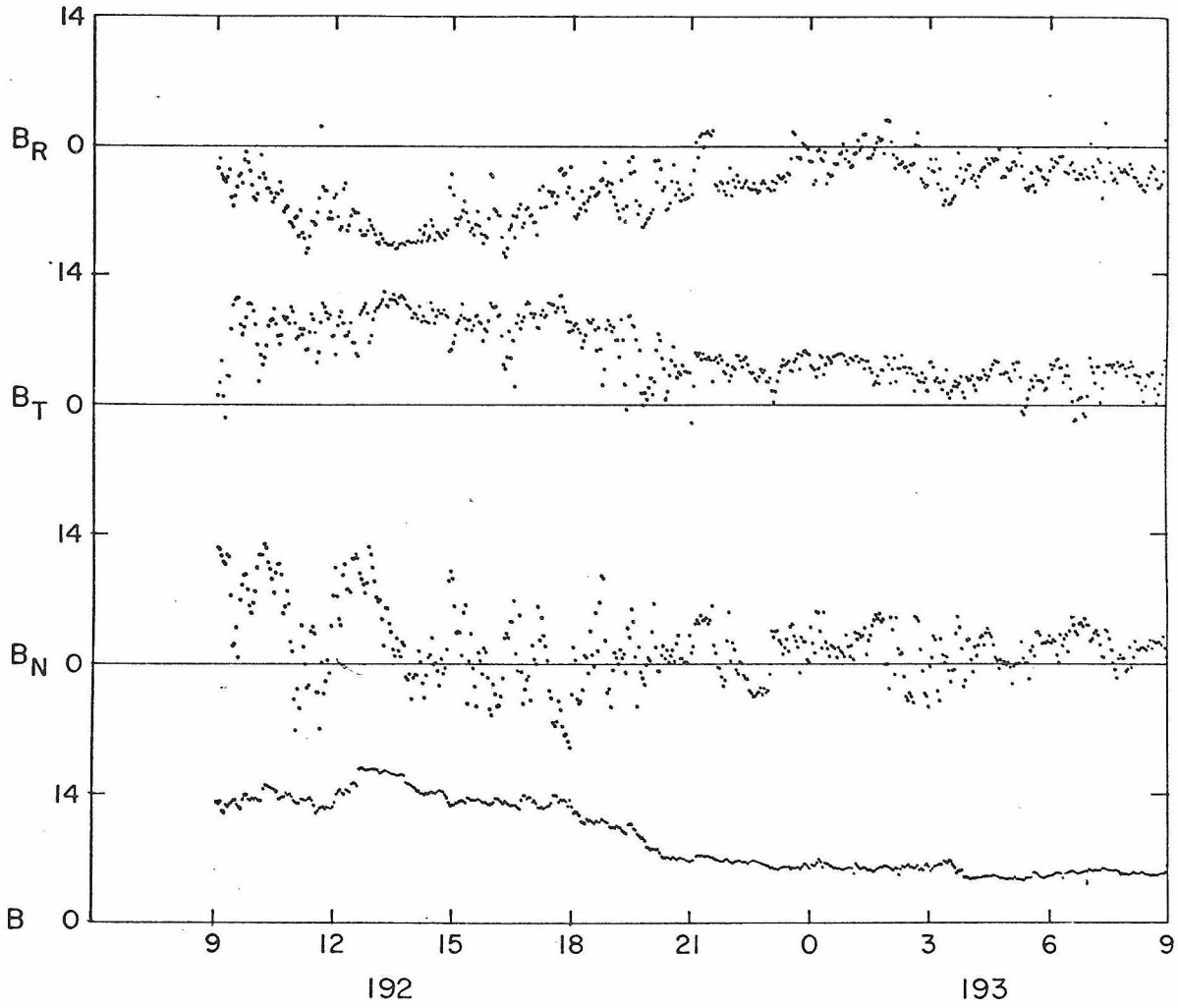

Figure 6. 169.75 sec averages of field data plotted over a 24 hour period of Figure 4. Field strengths here are averaged magnitudes, and thus have more significance than those in Figure 5, where the magnitude of averaged field vectors is plotted. Note the increase in wave amplitude as the compression region is entered.

not as good; this could be caused either by highly aliased plasma data, or by inwardly propagating Alfvénic or magnetoacoustic wave modes. On days 193 and 194, the amplitude of the field fluctuations has decreased (this period is in the high velocity stream proper), and the correlation between $\underset{\sim}{b}$ and $\underset{\sim}{v}$ is extremely good (as in Figure 2a). The strength of the magnetic field fluctuations increases on all three axes as we move from the high velocity stream proper into the compression region at its leading edge; note, however, that the normal component of the field has more power than the radial or the tangential in the compression region itself (see Figure 6). This behavior appears to be a general property of field fluctuations in colliding stream regions.

Other examples of stream structure in the solar wind have characteristics similar to the above. Figure 7 is a plot of days 233 through 239 in the same format as Figure 4, except that now σ_S is the square root of the average total variance of the field components over 20.16 minute intervals (the plasma sampling period at the low data rate used here). In this example, the leading edge of the high velocity stream beginning on day 236 is preceded by dense low velocity gas and the trailing edge of another high velocity stream. Again we point out that the density increase across days 234 and 235 is almost certainly not associated with the pile-up of low velocity gas ahead of the high velocity stream, but instead is simply a reflection of the fact that lower velocities are associated with higher densities in the solar wind. This association is presumably because of conditions in the corona and the radial distribution of the energy

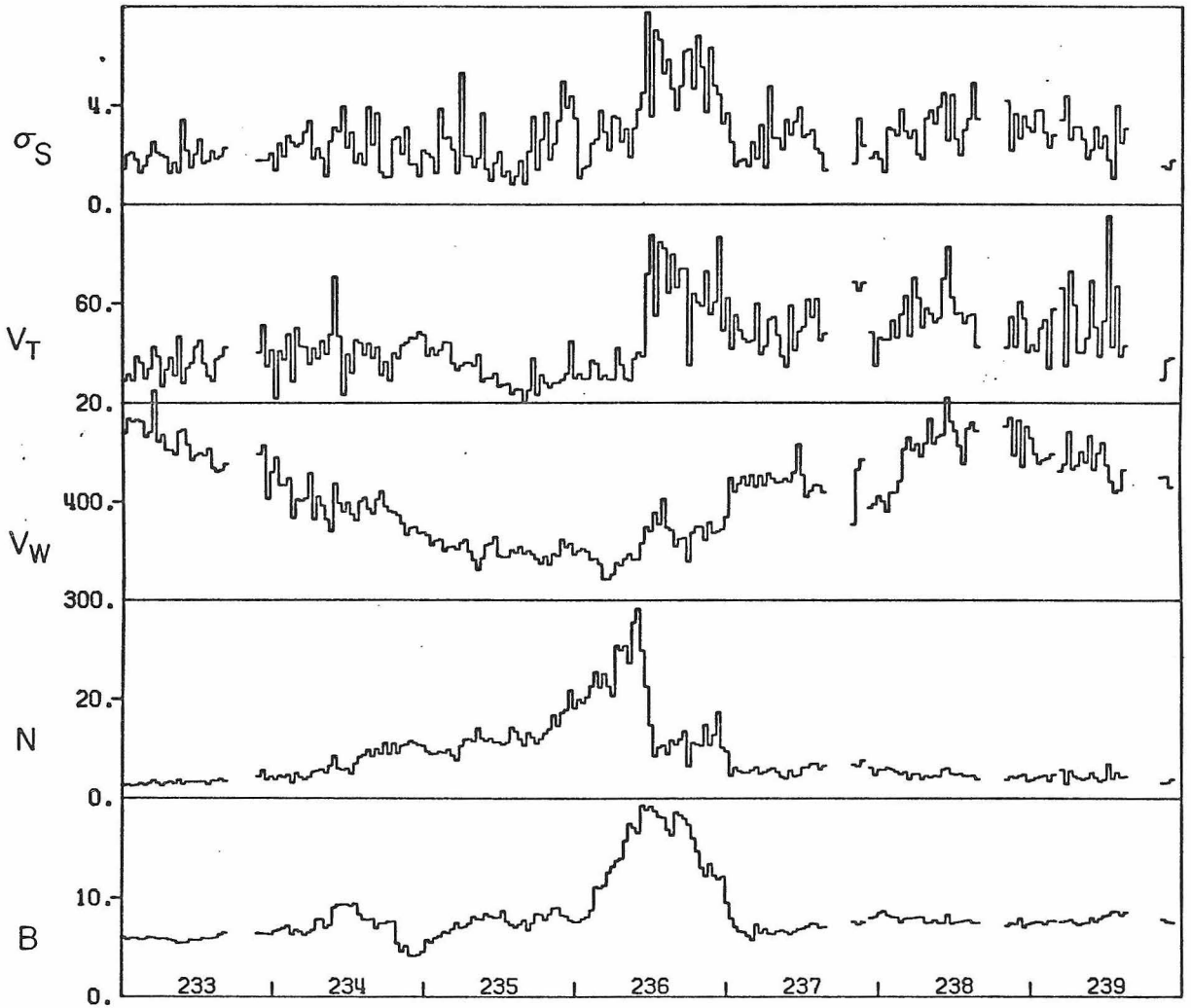

Figure 7. A low data rate example of detailed stream structure, using 40.4 min averages, similar in format to Figure 4. Note the high values of σ_S and V_T in the latter half of day 236.

supply of the solar wind. The increase in density and field strength from the beginning to the middle of day 236 is probably the result of a dynamic compression of slow stream gas ahead of the fast stream, and the increase in field strength and density in going from day 237 to the last half of day 236 is probably due to the deceleration and compression of the fast gas as it runs into the slower, more dense gas ahead. Days 233 and 237 through 239 contain excellent examples of the pure outwardly propagating Alfvén wave mode. Days 234, 235, and the first half of 236 contain Alfvén waves, but they are intermixed with more slowly varying structures which are associated with changes in density and field strength, and which may be static (note the large changes in field strength and density on these two and a half days in Figure 7 as compared to the four days mentioned above). The last half of day 236 (the compressed fast gas) contains very large amplitude fluctuations which are primarily Alfvénic. Figure 8 is a high time resolution plot of the field variations in this period, showing in detail the enhanced field fluctuations in the compression region. The normal component of the magnetic field has more power than the other components in the latter half of day 236.

Figure 9 is a third example of large scale stream structure although in this case the situation ahead of the fast stream is somewhat chaotic. Day 285 after hour 6, and day 286 through the middle of day 287 contain good examples of purely Alfvénic, outwardly propagating waves. Days 282 through 284 contain outwardly propagating Alfvén waves of smaller amplitude, but these are strongly

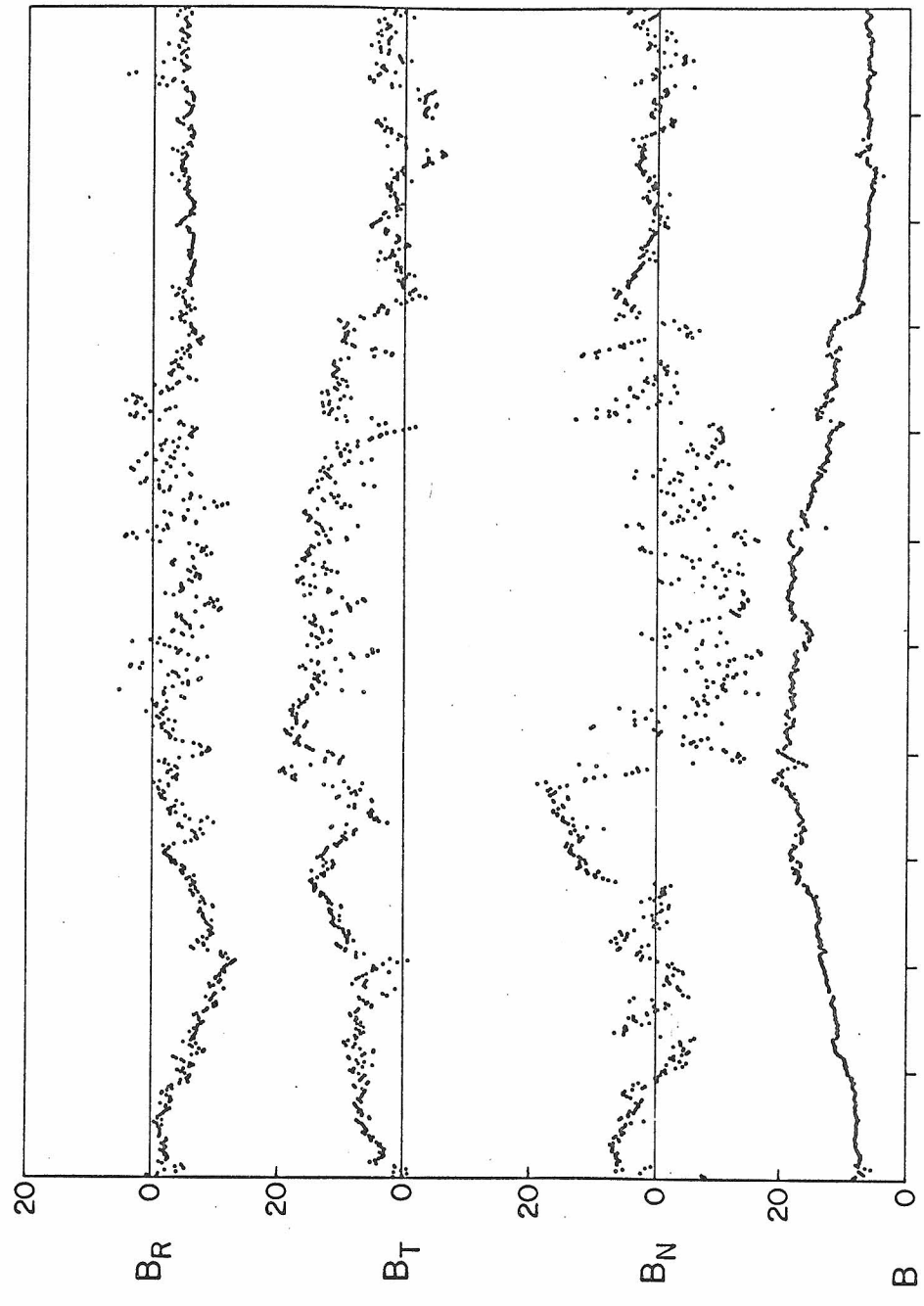

Figure 8. 168.75 sec averages of field data plotted over a 33 hour period of Figure 7, similar in format to Figure 6. The large wave amplitudes with high normal power in the latter half of day 236 are characteristic of colliding stream regions.

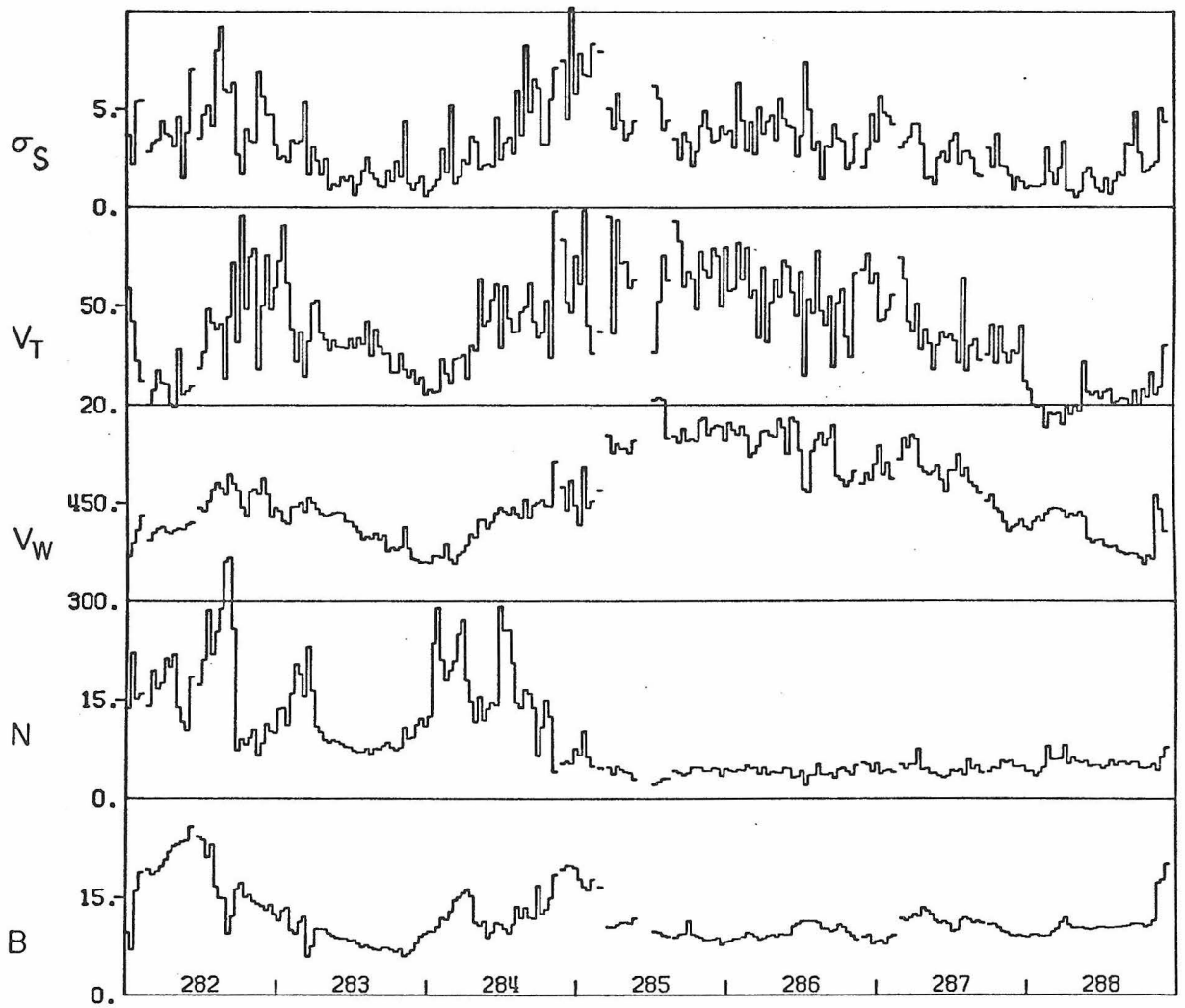

Figure 9. An example of detailed stream structure using 40.4 minute averages, similar in format to Figure 7. The situation ahead of the fast stream (before day 284) is chaotic.

intermixed with large scale changes in field strength and density which may be tangential discontinuities or weak shocks. Figure 10 shows the change in the microscale fluctuations in the high velocity stream proper as they are swept into the compression region at the leading edge of the stream. Running backward in spacecraft time at hour 4 of day 285, one goes from unmodified high velocity gas to more disturbed gas that has already entered the compression region. The amplitude of the fluctuations increases, and again the normal component of the field variations is stronger. Figure 11 is another example of large scale stream structure, and Figure 12 illustrates the character of the microscale magnetic field fluctuations in three distinct regions: the low velocity stream proper (day 227), the compressed leading edge of the high velocity stream (day 228), and the high velocity stream proper (day 231). Day 227 has some high frequency Alfvénic activity intermixed with large scale static structures, day 228 has very large amplitude waves which are predominantly Alfvénic (and which have more power in the normal direction), and day 231 has good examples of outwardly propagating Alfvén waves. Figure 13 is a plot similar to Figure 5, and demonstrates that the fluctuations on days 231 and 232 are extremely pure, outwardly propagating Alfvén waves. The average correlation between B_R and V_R for the four six-hour periods of day 228 was .5 (as opposed to an average of .88 for day 231), and the high frequency variance in the field strength is relatively high (as compared with day 231), so that the waves on day 228 in the compression region

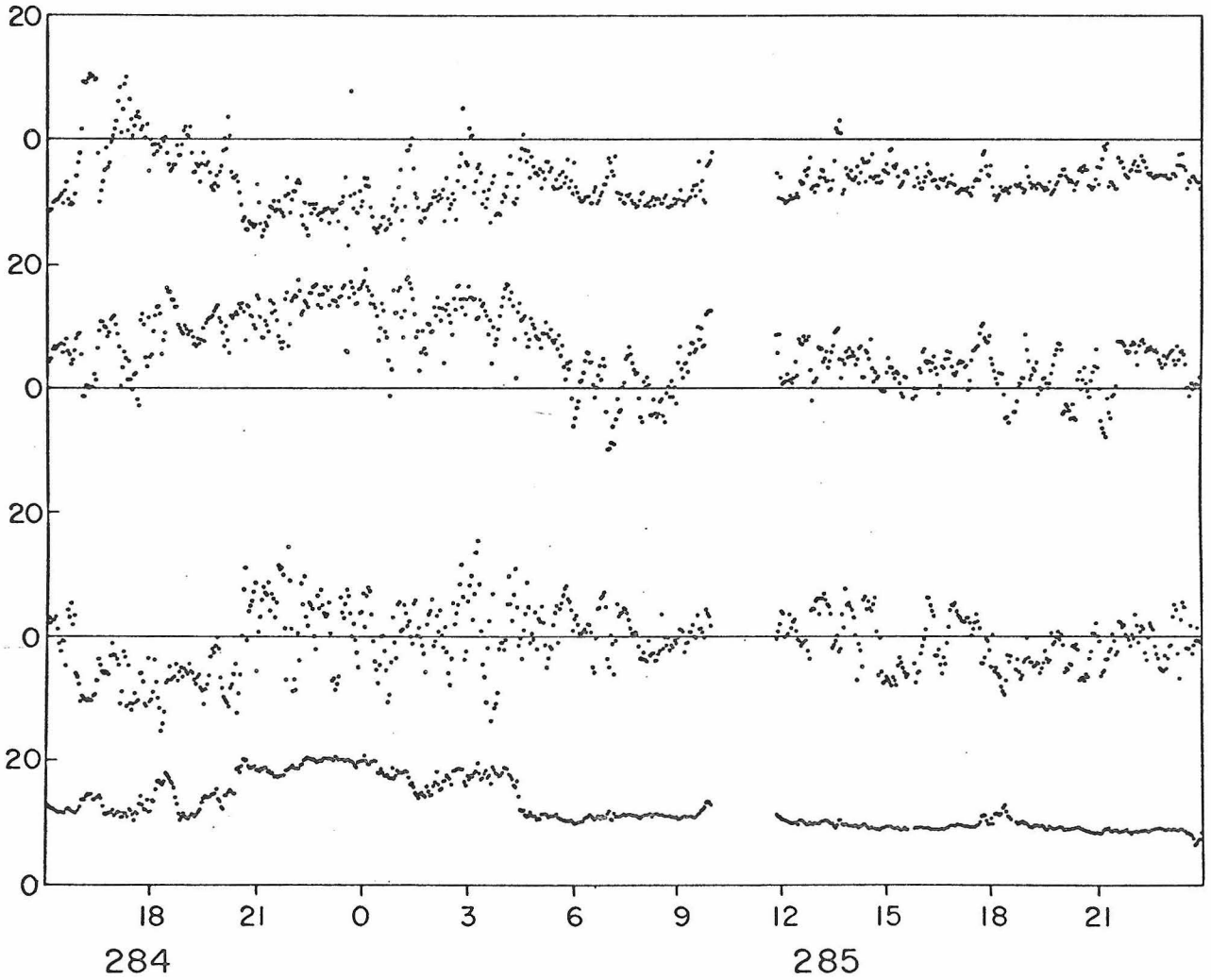

Figure 10. 168.75 sec averages of field components and magnitude plotted over a 33 hour period of Figure 9, similar to Figure 6. Note the abrupt increase in wave amplitude as the compression region is entered.

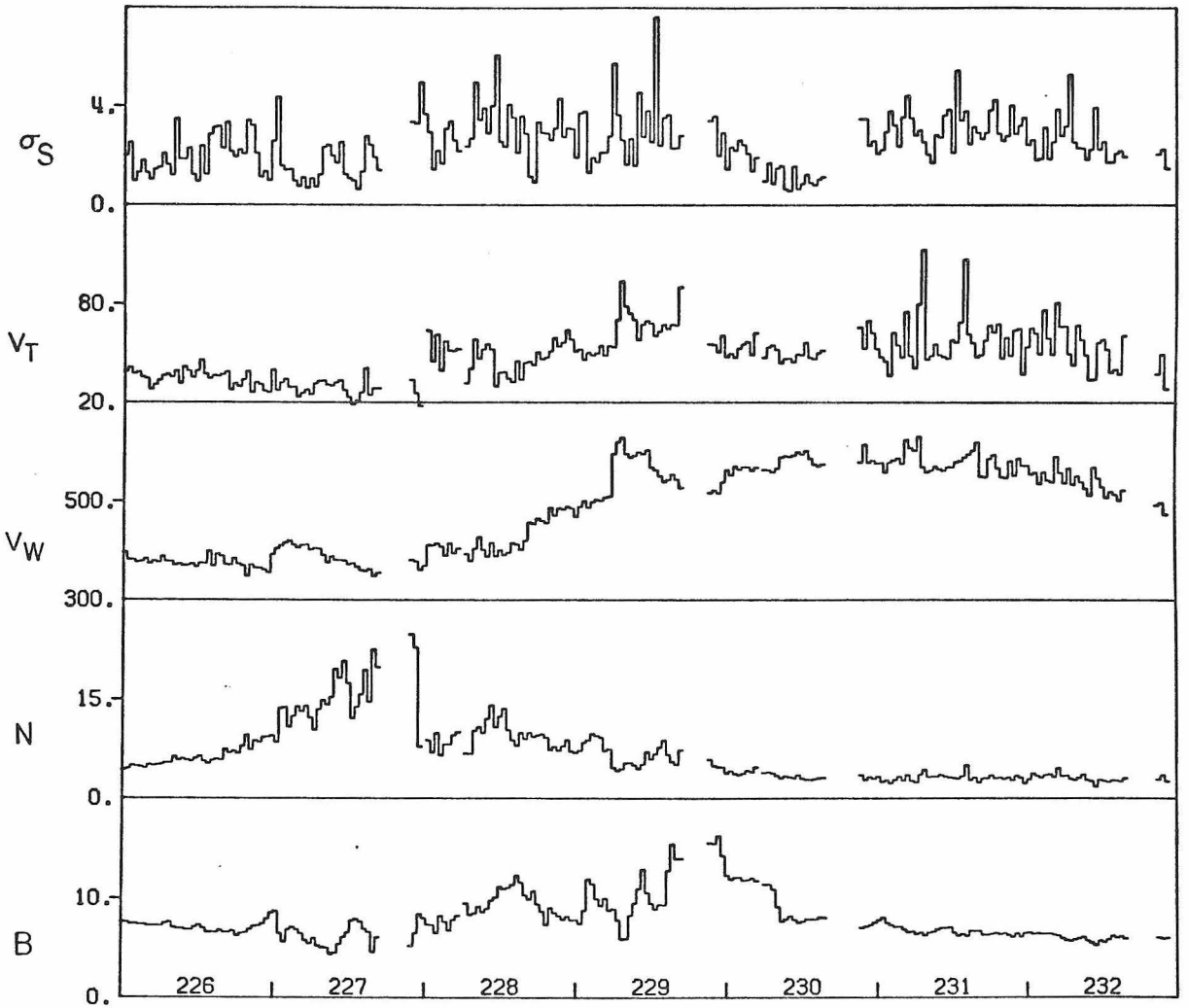

Figure 11. An example of detailed stream structure using 40.4 minute averages, similar in format to Figure 7. The velocity gradient extends from the beginning of day 228 into day 229.

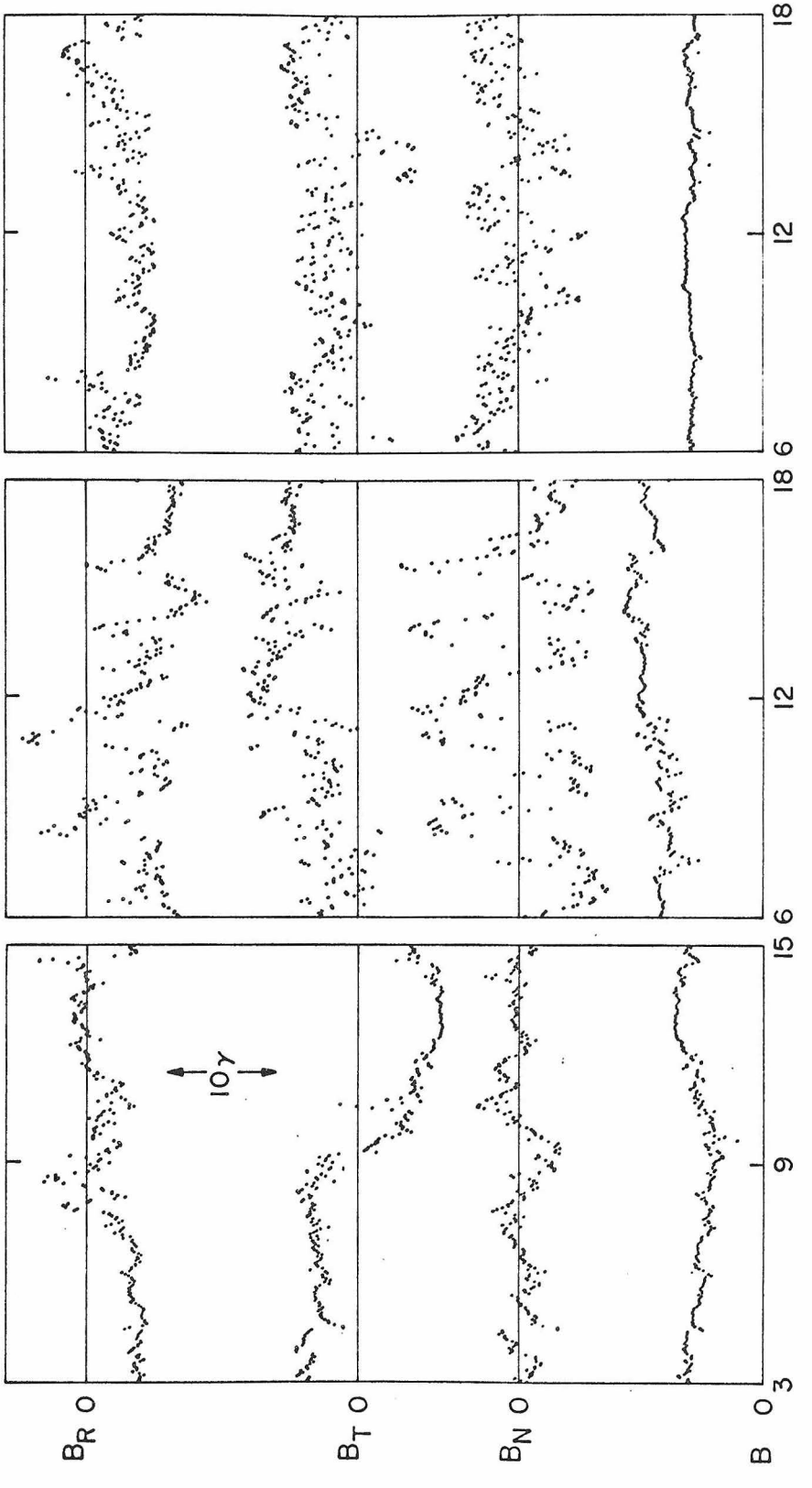

Figure 12. 168.75 sec averages of field components and magnitude plotted for three twelve hour periods of Figure 11, showing field fluctuations characteristic of low velocity streams, compression regions, and high velocity streams, respectively.

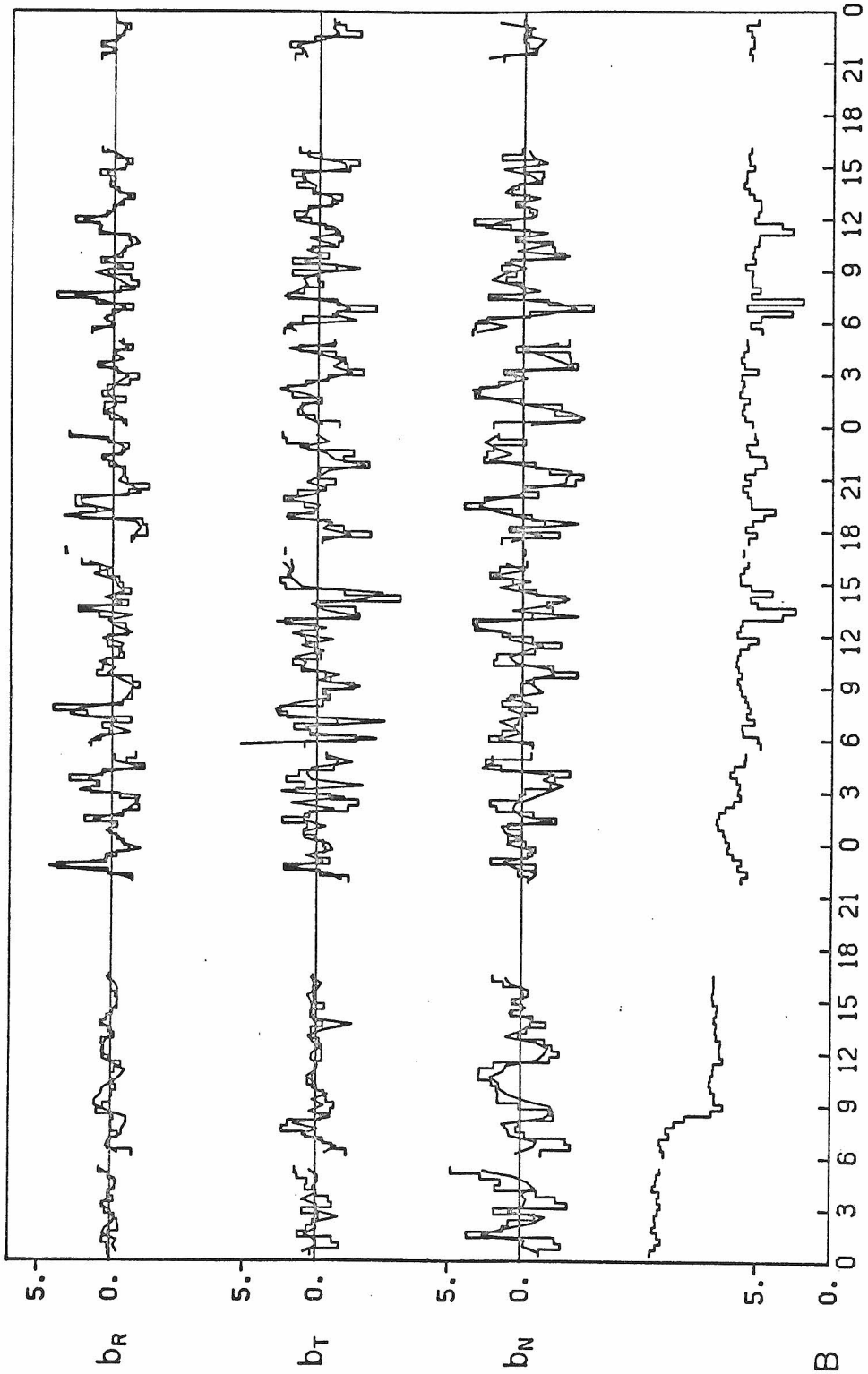

Figure 13. Magnetic field strength B and field and bulk velocity components for a three day period of Figure 11, similar to Figure 5. Each point represents a 20.2 min measurement, and variations with periods longer than four hours have been subtracted from all curves except B.

cannot be said to be purely Alfvénic or outwardly propagating, although they appear to be predominantly so.

2. Correlations between Three Hour Averages of Plasma and Field Data

The character of these general patterns in the stream structure of the solar wind can be seen in correlation coefficients computed between various three hour average parameters over a solar rotation. Correlation coefficients, means, and standard deviations have been calculated for each of the six rotations 1832 through 1837, and Table 2 gives the average of these quantities over the six rotations, weighted according to the number of available three hour data in a rotation. The number of available three hour data averages per solar rotation varied from 95 (1835) to 195 (1834), with an average of 160 per rotation. V_W, N, V_T, and B are as defined above, and β_p is the ratio of a proton thermal energy density to magnetic field energy density ($4\pi m_p N V_T^2/B^2$) computed using the three hour averages of N, V_T, and B; $|\rho|$ is the absolute value of the correlation coefficient ρ between B_R and V_R computed over three hour intervals. σ_{S1} and σ_{S2} are the square roots of the three hour average of the 168.75 sec and 22.5 minute total variances in field components, respectively; σ_{S3} is the square root of the three hour total variance in components. Thus σ_{S1} is representative of the amount of power in the very high frequency magnetic field fluctuations during each three hour interval; σ_{S2} and σ_{S3} are representative of the power at lower frequencies.

From Table 2 we see that V_W is well correlated both with

TABLE 2

Weighted averages of correlation coefficients computed over the six solar rotations of the Mariner V flight. AVE and STD are weighted averages of the average and standard deviation of the various parameters over a solar rotation.

	V_W	N	V_T	B	β_P	$\lvert\rho\rvert$	σ_{S1}	σ_{S2}	σ_{S3}
V_W	1.00	-.51	.66	.16	-.10	.07	.44	.37	.23
N	-.51	1.00	-.36	.08	.31	-.14	-.02	.10	.24
V_T	.66	-.36	1.00	.22	.18	.03	.55	.48	.32
B	.16	.08	.22	1.00	-.52	-.06	.52	.55	.56
β_p	-.10	.31	.18	-.52	1.00	-.10	-.12	-.10	-.11
$\lvert\rho\rvert$	.07	-.14	.03	-.06	-.10	1.00	.09	.06	.06
σ_{S1}	.44	-.02	.55	.52	-.12	.09	1.0	.93	.76
σ_{S2}	.37	.10	.48	.55	-.10	.06	.93	1.0	.87
σ_{S3}	.23	.24	.32	.56	-.11	.06	.76	.87	1.0
AVE	410.	8.5	42.8	8.5	.60	.63	1.46	2.68	4.23
STD	75.	5.4	14.8	3.0	.51	.27	.65	1.25	2.09

V_T and with σ_{S1}. These high correlations occur because high velocity streams are generally hotter, with more power in high frequency field fluctuations. The good anti-correlation between V_W and N reflects the generally lower densities of higher velocity regions. The high correlation between V_T and σ_{S1} occurs both because each is higher in high velocity streams and because local "hot" spots in temperature are usually associated with stream-stream collision regions, which contain very large amounts of high frequency magnetic field fluctuation. B correlates well with σ_{S1} because B is generally high during the stream-stream collisions, where σ_{S1} is high. Note that even though B and σ_{S1} correlate well, and V_W and σ_{S1} also correlate well, B and V_W are poorly correlated; this comes about because both σ_{S1} and B are enhanced in the colliding stream regions (where V_W is low and increasing), whereas B falls off and σ_{S1} stays at relatively high values during the high velocity stream itself.

The standard deviations in field components characteristic of lower frequency variations (σ_{S2} and σ_{S3}) are not as well correlated with V_T and V_W as is σ_{S1}. We ascribe this to the fact that σ_{S2} and σ_{S3} are more strongly influenced by the presence of long term trends and large scale, non-wavelike structures (such as polarity reversals, compression regions, tangential discontinuities, etc.). The parameter σ_{S1} is comparatively free of such low frequency effects, and we feel that it is the best index to the relative strength of the dynamic, wavelike fluctuations in the magnetic field.

There is a good anti-correlation of β_p with B, but poor correlations with N and V_T, even though these latter quantities are also used in its computation; this indicates that the magnetic field strength is the dominant factor producing variation in β_p. β_p correlates very poorly with V_W and σ_{S1}. High velocity streams, even though they are hotter, are not necessarily high β_p regions, because in general the density is lower. Also, the interaction regions between high and low velocity streams (where σ_{S1} is highest) are not necessarily high β_p regions, even though these regions are local "hot" spots, because usually the magnetic field strength is also very high. In general, β_p is a very poor index for the strength of the high frequency magnetic field fluctuations, and thus we conclude that these fluctuations are not governed by the local balance between proton thermal energy density and magnetic field energy density (in contrast to the conclusions of Burlaga, Ogilvie and Fairfield, 1969). Rather the strength of the microscale fluctuations is predominantly governed by the non-local (i.e., macroscale) properties of the solar wind, such as stream structure and generation or amplification of waves in colliding stream regions, and the best index to the strength of these fluctuations is the proton temperature V_T.

Table 2 shows that $|\rho|$, which is an indication of the presence of the waves, correlates very poorly with all other quantities; this fact was the basis for the statement in Belcher, Davis, and Smith [1969] that the Alfvén waves have "...no discernible pattern of association with large scale structures such as high velocity streams ...". As far as the presence of the waves is concerned, this state-

ment is strictly true; examples of the Alfvén waves can be found under almost any macroscale condition. However, although $|\rho|$ is an index to the presence of the waves, it gives no indication as to their amplitudes, and this is the property of the waves which correlates with the macroscale velocity structure.

In summary, we find that Alfvén waves in the solar wind are quite common, and may occur under most conditions. The purest examples of the outwardly propagating Alfvénic fluctuations are found in high velocity streams and on their trailing edges. Outwardly propagating Alfvén waves are also found in low velocity regions, but they tend to be of smaller amplitude and less pure in the sense that they are more strongly intermixed with structures which are not wavelike and possibly static. The largest amplitude Alfvén waves in the solar wind are found in the compression regions at the leading edges of high velocity streams; these regions may have inwardly propagating or non-Alfvénic wave modes. This characterization of Alfvén wave properties as related to stream structure is a generalized description only and notable exceptions exist. The macroscale properties of stream structure can be quite different from the examples we have given (i.e., shocks, etc.), and very large amplitude Alfvén waves can be found away from colliding stream regions (and even in low velocity streams, for example). However, the pattern described above occurs repeatedly throughout the five months of data from Mariner V, and appears to be a basic property of stream structure in the interplanetary medium.

C. Statistical Properties of the Microscale Fluctuations

1. Wave Spectra and Energy Densities

The frequency range over which the waves extend is extremely broad. Figure 14 is a plot of the cross spectrum between B_R and V_R for a two day period of good waves, computed with 30 degrees of freedom and giving estimates for coherency and phase at frequencies from 1/(4.2 hours) up to the Nyquist frequency of 1/(10.08 minutes). High coherencies and 0^o phase are indicative of the presence of the waves; they extend from a low frequency cutoff of about 1/(2 hours) up to the highest frequency measurable by the plasma probe, 1/(10.08 minutes). Cross-spectra of other segments of the data when waves are present show the same qualitative behavior. Taking into account the convective motion of the wind, these frequencies correspond to waves in the rest frame of the wind with periods from roughly 80 minutes (or less) to 16 hours, and wavelengths from $.25 \times 10^6$ km (or less) to 5×16^6 km.

It is likely that velocity fluctuations are well correlated with the magnetic field fluctuations at much higher frequencies than we can experimentally measure (1/(10.08 min.)). The velocity can easily follow the abrupt transitions shown in Figure 2b, and the properties of the magnetic field fluctuations above frequencies of 1/(10 min.) are similar to those below 1/(10 min.) (as discussed in the next section). Hence the higher frequency fluctuations in periods of good Alfvén waves are probably also Alfvénic. Since there is some variation at even the highest measurable frequency (see Figure 2b), we would

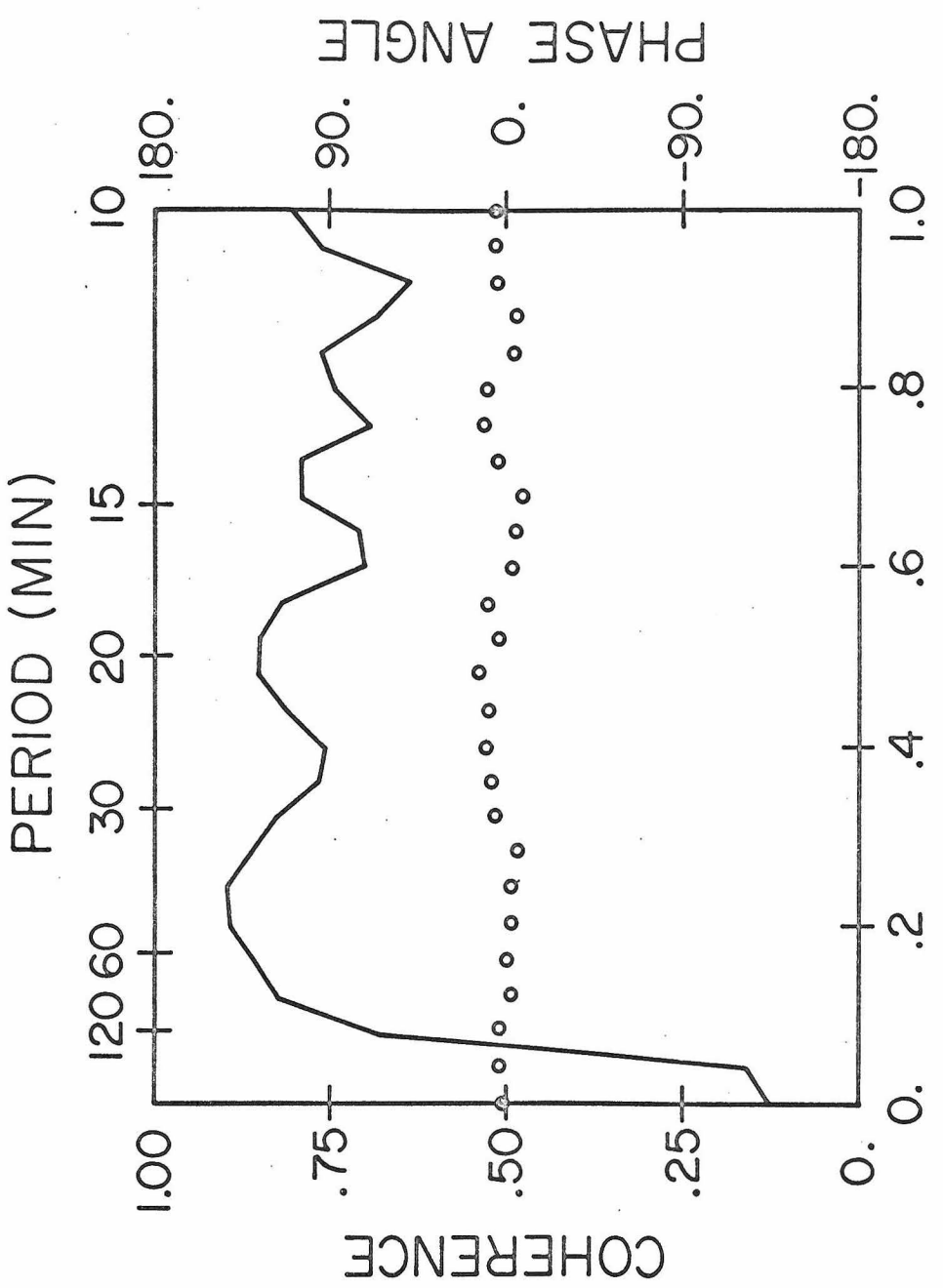

Figure 14. Coherency (line) and phase (circle) estimates for cross spectra between V_R and B_R during a period of good Alfvén waves (193-194), computed with thirty degrees of freedom.

argue that the Alfvén wave number spectrum typically extends from 10^3 km to 5×10^6 km.

Preliminary power spectra and cross spectra of the interplanetary magnetic field in the frequency range from 1/(107.5 min.) to 1/(25.2 sec.) have been calculated over most of the high data rate part of the mission, using the fast Fourier transform [Hinich and Clay, 1968]. Each spectrum is computed with 32 degrees of freedom, using 4096 averages, each 12.6 seconds in length (~14.3 hours of data); the resulting power spectral estimates are displayed on log-log plots, thus giving straight lines when the frequency dependence is $f^{-\alpha}$. The power levels obtained agree with those of earlier studies [Siscoe, et al, 1968; Coleman, 1966], except for those of Sari and Ness [1969], whose estimates during days of comparable magnetic field activity are in error by a factor of 10 to 100. In the range from approximately 1/(10 min.) to 1/(25.2 sec.), the spectra quite generally exhibit values of α close to 1.6 or 1.7; in the range from 1/(107.5 min.) to 1/(10 min.), there is a much broader spread in values of α, from as low as 1.5 to as high as 2.2. There is some indication that high values of α ($\alpha \simeq 2.$) in this frequency range are associated with cold plasma regions, where there is little high frequency field fluctuation, and that low values of α ($\alpha \simeq 1.5$) are associated with hot plasma regions, where there is a high level of high frequency field fluctuation (Table 2). A detailed study of least squares fits of α as a function of various plasma parameters is being made to test such possible correlations.

Slopes of spectra during periods of very good waves (high correlation, little variance in field strength and density) tend to cluster about 1.7, but can be as high as 2. in the low frequency range mentioned above. It should be noted that an f^{-2} spectral dependence is completely consistent with the observed properties of the waves; such a spectrum can result both from a succession of discontinuities [Siscoe, et al, 1968] or from irregular waveforms having no discontinuities. As we have seen, the waves can appear either as very irregular with gradual changes or as discontinuous, both on the time scale of Figure 2a and at the highest time resolution (Figure 2b and Figure 16). In contrast to Sari and Ness [1969], we strongly support the conclusions of Coleman [1967] that the observed fluctuations of the interplanetary magnetic magnetic field as measured by power spectra and especially as correlated with plasma measurements, indicates the existence of waves in the interplanetary medium.

When the waves are prominent, the energy densities associated with them are comparable to magnetic field and kinetic energy densities [Coleman, 1967, 1968]. For various three hour intervals which are dominated by wave activity we take the total wave energy density W_E to be half magnetic and half kinetic energy of plasma motion, and to be equal to $\delta B^2/4\pi$, where δB^2 is the total variance in field components over the three hour period. We compare this quantity to $B^2/8\pi$ and NkT_p in Table 3. The three regions designated as periods of extreme field activity are all located at the leading edges of high velocity streams; those designated as moderate to

TABLE 3

Period	$8\pi W_E/B^2$	W_E/NkT_P	Field Activity
167 12/15	.53	.95	moderate
192 15/18	.42	.88	extreme
195 12/15	.05	.13	quiet
228 12/15	.64	2.67	extreme
231 12/15	1.27	1.45	moderate
236 15/18	.42	1.28	extreme

quiet occur in the main bodies of streams or on their trailing edges. In all except the quiet period, W_E is comparable to field or thermal energy densities.

2. Microscale Anistropies

In the previous section dealing with the wave spectra, we made no reference to or use of the vector nature of the magnetic field fluctuations. Power levels and slopes were estimated on the basis of spectra computed for each of the three RTN cartesian axes, treating variations in each direction as independent variables and neglecting their vector properties. We now consider directions of maximum and minimum power in a preferred coordinate system, using a method employed by Sonnerup and Cahill [1967] and by Siscoe et al. [1968] which allows one to deduce power levels along any given direction. We first discuss the general properties of the microscale variations in the magnetic field, and then examine in detail specific periods of dynamical interest.

The variance tensor $\underset{\sim}{S}$ is defined by $S_{ij} = \langle B_i B_j \rangle - \langle B_i \rangle \langle B_j \rangle$, where i, j refer to the RTN components of the magnetic field $\underset{\sim}{B}$, and $\langle\ \rangle$ denotes averaging over a specified time interval. The tensor components in any other system are given by the usual tensor transformation for rotation of axes. The trace of $\underset{\sim}{S}$ is σ_S^2 as defined above; it is invariant to rotation of axes and is the sum of the eigenvalues of the matrix. If $\langle \underset{\sim}{B} \rangle$ is the average field, then

$$\sigma_{\|}^2 = \Sigma\ \langle B_i \rangle\, S_{ij}\, \langle B_j \rangle / \left| \langle \underset{\sim}{B} \rangle \right|^2$$

$$\sigma_{\perp}^2 = \sigma_S^2 - \sigma_{\|}^2$$

are the variances in the field parallel and perpendicular, respectively, to the average field direction. Hence they measure, respectively, the fluctuations that primarily change the field strength and those that primarily change the field direction.

The matrix $\underset{\sim}{S}$ can be diagonalized, yielding the eigenvalues $P_1 \geq P_2 \geq P_3$, and the corresponding eigenvectors $\underset{\sim}{S}_1$, $\underset{\sim}{S}_2$, and $\underset{\sim}{S}_3$. The eigenvectors form the principle axes of the "variance" ellipsoid; $\underset{\sim}{S}_1$ is the direction of maximum variation and $\underset{\sim}{S}_3$ is the direction of minimum variation. The relative magnitudes of the eigenvalues provide information about the anisotropy that is independent of coordinate system used. For example, if P_1, P_2, and P_3 are of approximately equal magnitudes, the fluctuations are approximately isotropic in three dimensions and the directions of the eigenvectors have little significance. If P_1 and P_2 are of comparable magnitude and much larger than P_3, the fluctuations are isotropic in the plane whose normal is $\underset{\sim}{S}_3$. If P_1 is much larger than P_2 or P_3, the fluctuations are primarily in the direction $\underset{\sim}{S}_1$. In the Mariner V data, we characteristically see large fluctuations in field components with little change in field strength. For variations of this nature, we should expect $\underset{\sim}{S}_1$ and $\underset{\sim}{S}_2$ to be perpendicular to $\langle \underset{\sim}{B} \rangle$, and $\underset{\sim}{S}_3$ to be parallel to $\langle \underset{\sim}{B} \rangle$.

In order to study the general nature of the field variations using this formalism, we have calculated variance matrices and the corresponding eigenvalues and eigenvectors from the basic magnetometer data for the entire Mariner V mission. Three different averaging times have been used in computing the $\underset{\sim}{S}$ matrices -- 168.75 sec. (2^{-9} day), 22.5 min (2^{-6} day), and 3 hours (2^{-3} day).

Each period is longer than the preceding by a factor of eight. The properties of the 168.75 second variance matrices are characteristic of very high frequency fluctuations, whereas the 3 hour variance matrices provide information about much lower frequency variations. Of course, we include the effects of the higher frequency fluctuations in the calculation of 3 hour variances, but since the spectrum of the magnetic fluctuations obeys a power law, we expect the lower frequencies to dominate in any given period. For each of these intervals we have also calculated B, the average magnitude of the field, and P_4, the variance in the field strength. Table 4 then gives averages over the entire mission of various quantities based on these interval averages. No attempt has been made to separate dynamic from static (purely convected) structures -- all data have been included. The low average values of P_2/P_1 and P_3/P_2 imply that in general the eigenvectors $\underset{\sim}{S}_1$, $\underset{\sim}{S}_2$ and $\underset{\sim}{S}_3$ are well defined directions, and thus a study of their directional distributions is meaningful and of some interest.

The RTN system is a poor one in which to study the eigenvectors, since $\langle \underset{\sim}{B} \rangle$ is obviously a preferred direction (values of P_4/P_1 are very small). Since the flow direction of the solar wind also has physical significance and is approximately along $\underset{\sim}{e}_R$, we resolve the eigenvectors from each interval in a field-velocity coordinate system shown in Figure 15 and defined as follows: Z is the direction of $\underset{\sim}{e}_B$, the unit vector parallel to $\langle \underset{\sim}{B} \rangle$ for that interval, X is the direction of $\underset{\sim}{e}_B \times \underset{\sim}{e}_R$, and Y is in the direction $\underset{\sim}{e}_Z \times \underset{\sim}{e}_X$. Thus,

TABLE 4

Average Eigenvalue Properties

Averaging Period	No. of Matrices	$\langle P_1 \rangle_{\gamma^2}$	$\langle P_2/P_1 \rangle$	$\langle P_3/P_2 \rangle$	$\langle P_3/P_1 \rangle$	$\langle P_4/P_1 \rangle$	$\langle P_1/B^2 \rangle$
168.75 sec	59488	2.3	.28	.30	.08	.16	.04
22.5 min	7523	7.4	.28	.32	.08	.10	.13
3 hr	990	16.8	.35	.37	.12	.08	.31

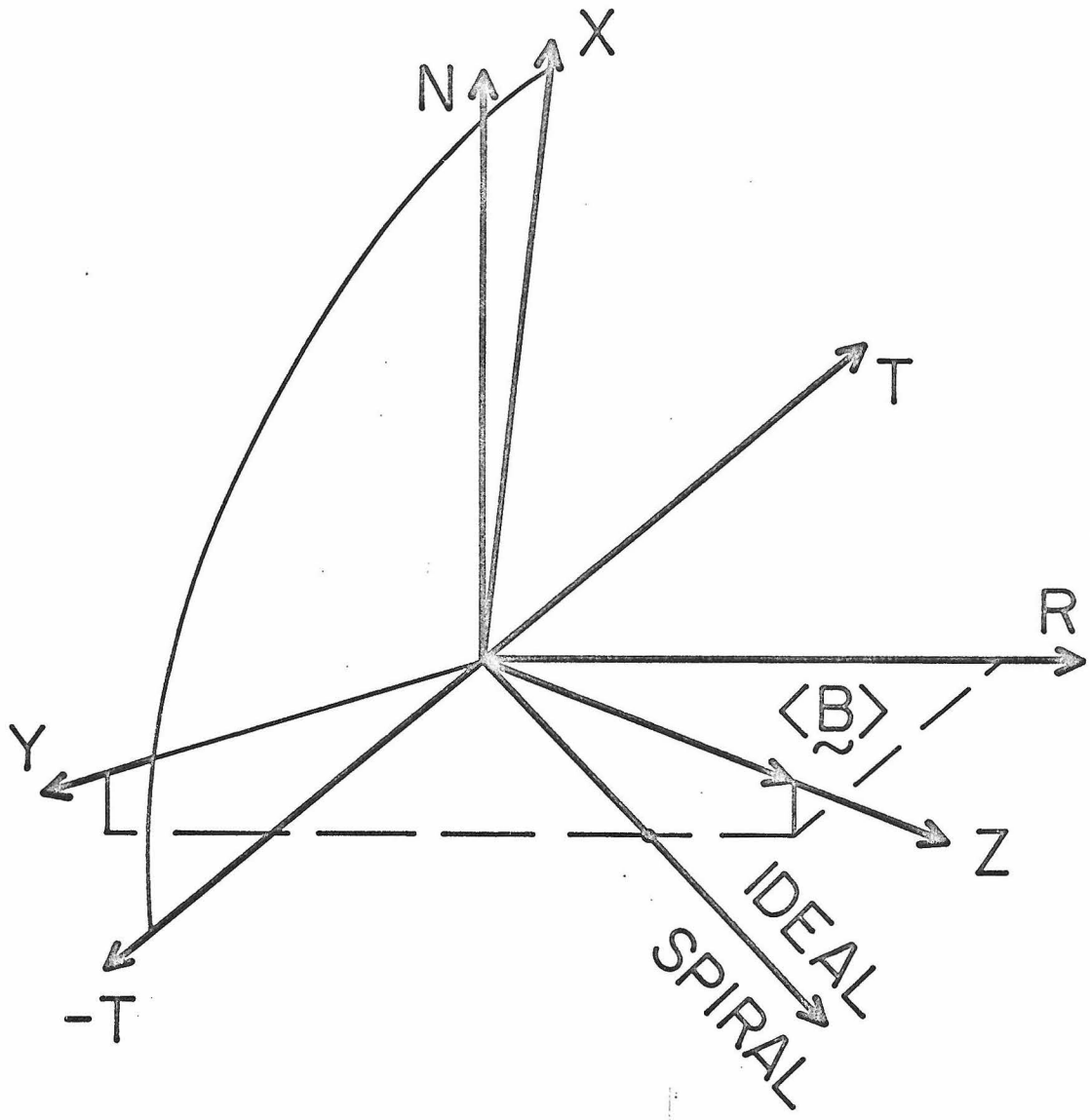

Figure 15. The field-velocity coordinate system. Z is along the average field direction, and X is along $\underset{\sim}{e}_B \times \underset{\sim}{e}_R$. The X-axis thus always lies in the TN plane.

fluctuations along X are perpendicular both to the average field for that interval and the radial direction. Note that the field-velocity coordinate system changes from interval to interval, since the direction $\langle \underset{\sim}{B} \rangle$ changes. For long averaging times, $\langle \underset{\sim}{B} \rangle$ tends to be along the spiral field direction and in the solar equatorial plane, and hence X tends to be along the N direction. For shorter averaging times, however, $\langle \underset{\sim}{B} \rangle$ frequently has a significant component out of the equatorial plane, and X no longer bears as close a relationship to the N direction. The ultimate justification for the use of these coordinate axes is that eigenvector distribution are symmetric in this system.

Table 5 gives the directional distribution in the field-velocity system of the eigenvectors associated with the 168.75 sec. variance matrices; distributions for the 22.5 min and 3 hour matrices are given in Tables 6 and 7. Directions are specified by the usual spherical polar coordinates θ and φ, where θ is the polar angle from the Z axis and φ is an azimuthal angle measured from the X-axis. The range of θ is divided into equal increments of $\cos\theta$ to correct for solid angle effects. Thus the various bins in the distribution tables represent equal solid angles on the unit sphere, and a spatially isotropic distribution of vectors would have equal percentages in each bin. The full distribution in all eight octants of the unit sphere is not given for the following reasons: 1) the eigenvectors are arbitrary to a factor of ± 1, so that we may give all vectors a positive components along Z; 2) examination of the distributions thus obtained reveals that they are symmetric both about the XZ plane and the YZ plane. Thus by reflection in these two planes we obtain a

TABLE 5

Eigenvector Distributions 168.75 sec. intervals

$\underset{\sim}{S}_1$: Direction of Maximum Variation

		φ					
		0/18	18/36	36/54	54/72	72/90	0/90
	0/41	.7	.7	.7	.6	.6	3.3
	41/60	1.1	1.0	.8	.7	.7	4.3
θ	60/76	3.3	3.1	2.8	2.1	1.7	13.0
	76/90	21.7	19.6	16.5	12.2	9.3	79.3
	0 to 90	26.8	24.4	20.8	15.6	12.3	

$\underset{\sim}{S}_2$: Direction of Intermediate Variation

		φ					
		0/18	18/36	36/54	54/72	72/90	0/90
	0/41	2.4	2.6	2.8	3.1	3.3	14.2
	41/60	1.6	2.0	2.7	3.0	3.2	12.5
θ	60/76	2.7	3.4	4.4	5.3	5.7	21.5
	76/90	7.3	8.7	10.7	12.1	13.0	51.8
	0 to 90	14.0	16.7	20.6	23.5	25.2	

$\underset{\sim}{S}_3$: Direction of Minimum Variation

		φ					
		0/18	18/36	36/54	54/72	72/90	0/90
	0/41	12.1	13.2	15.0	16.5	18.4	75.2
	41/60	1.0	1.4	1.9	2.4	2.9	9.6
θ	60/76	.8	1.1	1.5	1.7	2.2	7.3
	76/90	.9	1.1	1.6	1.9	2.3	7.8
	0 to 90	14.8	16.8	20.0	22.5	25.8	

TABLE 6

Eigenvector Distributions 22.5 minute intervals

$\underset{\sim}{S}_1$: Direction of Maximum Variation

		φ					
		0/18	18/36	36/54	54/72	72/90	0 to 90
	0/41	.6	.6	.5	.4	.4	2.5
	41/60	1.1	1.1	1.0	1.0	.5	4.7
θ	60/76	3.8	3.8	3.3	2.4	1.6	14.9
	76/90	22.5	19.6	16.7	11.1	8.2	78.1
	0 to 90	28.0	25.1	21.5	14.9	10.7	

$\underset{\sim}{S}_2$: Direction of Intermediate Variation

		φ					
		0/18	18/36	36/54	54/72	72/90	0 to 90
	0/41	2.5	2.9	2.8	2.8	3.1	14.1
	41/60	1.5	1.9	2.3	2.3	2.5	10.5
θ	60/76	1.8	2.6	3.8	4.1	4.8	17.1
	76/90	7.5	9.2	12.1	14.3	15.3	58.4
	0 to 90	13.3	16.6	21.0	23.5	25.7	

$\underset{\sim}{S}_3$: Direction of Minimum Variation

		φ					
		0/18	18/36	36/54	54/72	72/90	0 to 90
	0/41	12.0	13.5	14.6	17.4	19.4	76.9
	41/60	.7	1.1	1.3	2.3	2.4	7.8
θ	60/76	.4	.7	1.4	1.7	1.9	6.1
	76/90	.6	1.4	2.0	2.5	2.7	9.2
	0 to 90	13.7	16.7	19.3	23.9	26.4	

TABLE 7

Eigenvector Distributions 3 hour intervals

$\underset{\sim}{S}_1$: Direction of Maximum Variation

		φ					
		0/18	18/36	36/54	54/72	72/90	0/90
	0/41	.7	1.1	.9	1.1	.8	4.6
	41/60	1.2	3.1	2.2	.9	1.6	9.0
θ	60/76	5.8	6.3	4.0	2.7	2.9	21.7
	76/90	19.5	14.4	13.2	8.7	8.7	64.5
	0 to 90	27.2	24.9	20.3	13.4	14.0	

$\underset{\sim}{S}_2$: Direction of Intermediate Variation

		φ					
		0/18	18/36	36/54	54/72	72/90	0/90
	0/41	2.8	4.3	4.4	3.7	4.0	19.2
	41/60	2.1	2.3	3.3	3.6	3.8	15.1
θ	60/76	3.4	3.0	4.1	4.8	4.9	20.2
	76/90	8.8	6.8	7.5	9.3	12.6	45.0
	0 to 90	17.1	16.4	19.3	21.4	25.3	

$\underset{\sim}{S}_3$: Direction of Minimum Variation

		φ					
		0/18	18/36	36/54	54/72	72/90	0/90
	0/41	11.0	10.7	12.1	13.9	17.0	64.7
	41/60	1.1	1.9	2.1	2.1	4.0	11.2
θ	60/76	1.2	.7	2.3	2.3	2.6	9.1
	76/90	1.2	1.4	4.4	3.9	3.7	14.6
	0 to 90	14.5	14.7	20.9	22.2	27.3	

representative distribution in the first octant only; distributions in other octants are symmetric reflections of the first octant.

The distributions presented demonstrates that $\underset{\sim}{S}_3$ has a strong tendency to be parallel to $\langle \underset{\sim}{B} \rangle$ ($\theta = 0^o$), whereas $\underset{\sim}{S}_1$ and $\underset{\sim}{S}_2$ are generally perpendicular to $\langle \underset{\sim}{B} \rangle$ ($\theta = 90^o$) as we would expect. In addition, $\underset{\sim}{S}_1$ tends to be nearer the X-axis ($\varphi = 0^o$) than the Y-axis ($\varphi = 90^o$); i.e., the direction of maximum power tends to be in the $\underset{\sim}{e}_B x \underset{\sim}{e}_R$ direction. This is true for each of the three different averaging times, and thus is characteristic of the microscale fluctuations over a broad frequency range. It should be remembered that the higher frequency fluctuations are superimposed on lower frequency fluctuations with larger amplitudes. The higher frequency fluctuations hence appear to adjust themselves to the average "background" field that they see, even though this field is changing as part of a lower frequency variation.

Having established that this non-stationary field-velocity coordinate system is preferred for the microscale fluctuations, we compute variances of the field along the XYZ axes. The variance of the magnetic field in a direction $\underset{\sim}{e}_D$ is given by $\underset{\sim}{e}_D \cdot \underset{\sim}{S} \cdot \underset{\sim}{e}_D$, where $\underset{\sim}{S}$ is the variance matrix. Table 8 gives the average fractional variances for both the XYZ and the RTN systems; $P_S = P_X + P_Y + P_Z$ = Trace ($\underset{\sim}{S}$) and is thus independent of any particular coordinate system. $\langle\ \rangle$ denotes long term averages of the properties of variance matrices for a given time interval; in Table 8 the averages are taken over the entire Mariner V mission. In the XYZ system, $\langle P_X/P_S \rangle$, the aver-

TABLE 8

Average Fractional Variances

Averaging Period	No. of Matrices	$\langle P_S \rangle$ γ^2	$\langle P_X/P_S \rangle$	$\langle P_Y/P_S \rangle$	$\langle P_Z/P_S \rangle$	$\langle P_R/P_S \rangle$	$\langle P_T/P_S \rangle$	$\langle P_N/P_S \rangle$
168.75 sec	59488	2.6	.51	.38	.11	.26	.33	.40
22.5 min	7523	9.3	.52	.37	.11	.25	.34	.41
3 hr	990	23.8	.47	.36	.17	.26	.34	.40

age fractional variance in the X direction, is consistently larger than $\langle P_Y/P_S \rangle$, which is in turn larger than $\langle P_Z/P_S \rangle$, as we would expect from the eigenvector distributions. In the RTN system, $\langle P_N/P_S \rangle$ is larger than $\langle P_T/P_S \rangle$ and $\langle P_R/P_S \rangle$ for all averaging times, as we would expect from the orientation of the XYZ system with respect to the RTN system. The $\underset{\sim}{e}_B x \underset{\sim}{e}_R$ direction is of more significance than the $\underset{\sim}{e}_N$ direction, as is shown by the fact that $\langle P_X/P_S \rangle$ is 25% larger than $\langle P_N/P_S \rangle$. We note that R and T do not display equal amounts of power (as we might naively assume from the average orientation of the XYZ system) because the direction of maximum power, $(\underset{\sim}{e}_B x \underset{\sim}{e}_R)$, is always perpendicular to the R direction, whereas it can have a large component along the T direction if $\underset{\sim}{e}_B$ has a significant N component. Table 8 also indicates that the average fractional variance along the field direction is larger for the three hour intervals than for the 22.5 min. or 168.75 sec. intervals, even though Table 4 shows that the ratio of variance in field strength to the maximum component variance is smaller for the three hour intervals. These results at first appear inconsistent, but it must be remembered that for long averaging times the standard deviations in components become comparable to the background field strength (Table 4) and consequently the concept of an "average" background field direction is not as well defined for the three hour intervals in Table 8 as it is for the shorter averaging times. Thus we can characterize the general statistical nature of the microscale fluctuations as consisting primarily of variations perpendicular to the average field direction

("average" referring to the time scale of interest), with more power along the $\underset{\sim}{e}_B x \underset{\sim}{e}_R$ direction over a wide range of frequencies. In the RTN system these properties produce on the average more power in the N direction, with minimal power along the R direction. The fluctuations are primarily Alfvénic, with magnetoacoustic wave modes (if present) having a small average power of the order of 10% or less of that in the Alfvén mode (Table 8).

For completeness, we mention that one can also apply the basic ideas used above in a more sophisticated power spectral analysis. For every six hour interval in the Mariner V mission with sufficient data return, we have computed auto and cross spectral estimates with 32 degrees of freedom, using 168.75 second averages of the magnetic field. This process yields (for each 6 hour interval) eight power spectral tensors (each with six independent elements, three auto powers and three cross powers) at eight uniformly spaced frequencies in the frequency range from 1/(45 min) to 1/(5.625 min). These matrices were diagonalized to obtain characteristic directions of maximum and minimum power, etc., for each frequency; properties of the power matrices (for each individual frequency) averaged over the entire mission are similar to the properties of the variance matrices described above, over the entire frequency range. The advantage of the power spectral method lies in the fact that it can describe anisotropies characteristic of a specific frequency, whereas the variance matrix approach gives results that are in some sense representative of all frequencies above a certain minimum fre-

quency. The drawback of the power spectral method is that it is quite difficult to define an average field direction for the higher frequency fluctuations, since they are superimposed on larger amplitude low frequency variations; thus, distributions similar to those in Table 5 for the higher frequency spectral estimates (using the 6 hour averaged magnetic field as the direction of $\underset{\sim}{e}_B$) are not as strongly peaked as those in Table 5. The variance matrix approach, on the other hand, provides an obvious and physically appropriate average "background" field for each interval, and hence provides the most sharply peaked distributions. In any event, the two methods give basically the same result, conclusively demonstrating that the anisotropies described above are characteristic of the microscale fluctuations over a wide frequency range.

In the above considerations we have made no attempt to select data on any basis; every interval of the Mariner V mission with sufficient data return has been included. If we compute distributions such as those given in Tables 4 through 8 for individual solar rotations instead of for the entire mission (as above), we obtain essentially the same results except for the increase in power level (P_S) as Mariner V approaches the sun. Average fractional variances and eigenvector distributions remain approximately the same from one solar rotation to the next, even though the average power level of the fluctuations increases, and it appears that the $\underset{\sim}{e}_B \times \underset{\sim}{e}_R$ fractional power excess averaged over a solar rotation is independent of distance from the sun in the range .7 to 1 a.u.

Since all data are included in these analyses, with no attempt to distinguish dynamic from static effects, the observed $\underset{\sim}{e}_B x \underset{\sim}{e}_R$ anisotropy might be caused either by a dynamical process associated with fluctuations propagating in the rest frame of the wind, or, perhaps, by some preferred orientation of static irregularities convected by the solar wind. To resolve this ambiguity, we have computed distributions similar to those in Tables 4 through 8 for each day of the mission, using 22.5 minute variance matrices (64 per day) and 168.75 second variance matrices (512 per day). The 168.75 second variances invariably show values of $\langle P_X/P_S \rangle$ (averaging over one day) larger than $\langle P_Y/P_S \rangle$ or $\langle P_Z/P_S \rangle$. Only on very quiet days is $\langle P_X/P_S \rangle$ approximately equal to $\langle P_Y/P_S \rangle$; on more active days (moderate power at high frequencies) values for the different parameters averaged over the day are closely similar to those given in Table 8. The properties of the 22.5 minute variances, considered on a day to day basis, also exhibit the expected anisotropies, although not as consistently as do the 168.75 second variances (139 days out of 150 have $\langle P_X/P_S \rangle > \langle P_Y/P_S \rangle$). More significantly, the $\underset{\sim}{e}_B x \underset{\sim}{e}_R$ anisotropy tends to be most pronounced in the interaction regions between high and low velocity streams, for both averaging times. For example, Table 9 gives the distribution of eigenvectors associated with maximum variation for both 168.75 second and 22.5 minute intervals on day 192. As previously mentioned, this is a period of rapid velocity increase and large magnetic field variations (see Figure 4). Table 9 indicates that both the 22.5 minute and

TABLE 9

$\underset{\sim}{S}_1$: Direction of Maximum Variation (168.75 sec intervals), Day 192

		φ					
		0/18	18/36	36/54	54/72	72/90	0 to 90
	0/41	.0	.0	.0	.0	.0	.0
	41/60	.0	.0	.0	.0	.0	.0
θ	60/76	1.3	2.2	2.2	.3	.9	6.9
	76/90	31.0	26.9	16.5	7.9	10.8	93.1
	0 to 90	32.3	29.1	18.7	8.2	11.7	

168.75 sec, 316 matrices:

$$\langle P_S \rangle = 6.9\gamma^2, \quad \langle P_X/P_S \rangle = .59, \quad \langle P_Y/P_X \rangle = .36, \quad \langle P_X/P_S \rangle = .05$$

$\underset{\sim}{S}_1$: Direction of Maximum Variation (22.5 min intervals), Day 192

		φ					
		0/18	18/36	36/54	54/72	72/90	0 to 90
	0/41	.0	.0	.0	.0	.0	.0
	41/60	.0	2.5	.0	.0	.0	5.0
θ	60/76	7.5	5.0	2.5	.0	2.5	17.5
	76/90	35.0	17.5	12.5	7.5	5.0	77.5
	0 to 90	42.5	25.0	15.0	7.5	7.5	

22.5 min, 40 matrices:

$$\langle P_S \rangle = 18.2\gamma^2, \quad \langle P_X/P_S \rangle = .60, \quad \langle P_Y/P_S \rangle = .30, \quad \langle P_Z/P_S \rangle = .10$$

168.75 second intervals have a strongly enhanced $\underset{\sim}{e}_B x \underset{\sim}{e}_R$ anisotropy as compared to the average values (Tables 4 through 8). Figure 6 is a point plot of 168.75 second field averages on this day, clearly showing larger fluctuations in the normal component of the field at low frequencies. Figure 16 is a plot of one hour of basic magnetometer data (one reading in approximately 4 seconds) on this same day, showing roughly the same effect at higher frequencies. On the following day (193) the wind velocity levels off and the power in the field fluctuations decreases (see Figure 6); the anisotropy in the 168.75 second variances decreases almost exactly to the values given in Table 8, and the $\underset{\sim}{e}_B x \underset{\sim}{e}_R$ anisotropy in the 22.5 minute variances essentially disappears. Figures 8 and 12 illustrate this same effect in the microscale fluctuations of day 228 and 236, which are the interaction regions for the streams shown in Figures 7 and 11. Since the most prominent $\underset{\sim}{e}_B x \underset{\sim}{e}_R$ anisotropies tend to occur during regions of definitely non-static character, it is clear that the effect is a dynamic one, and not due to some peculiar orientation of static, convected discontinuities. This is not meant to imply that the anisotropy occurs only in stream-stream interaction regions, as it is essentially always present at high frequencies, and usually present at lower frequencies.

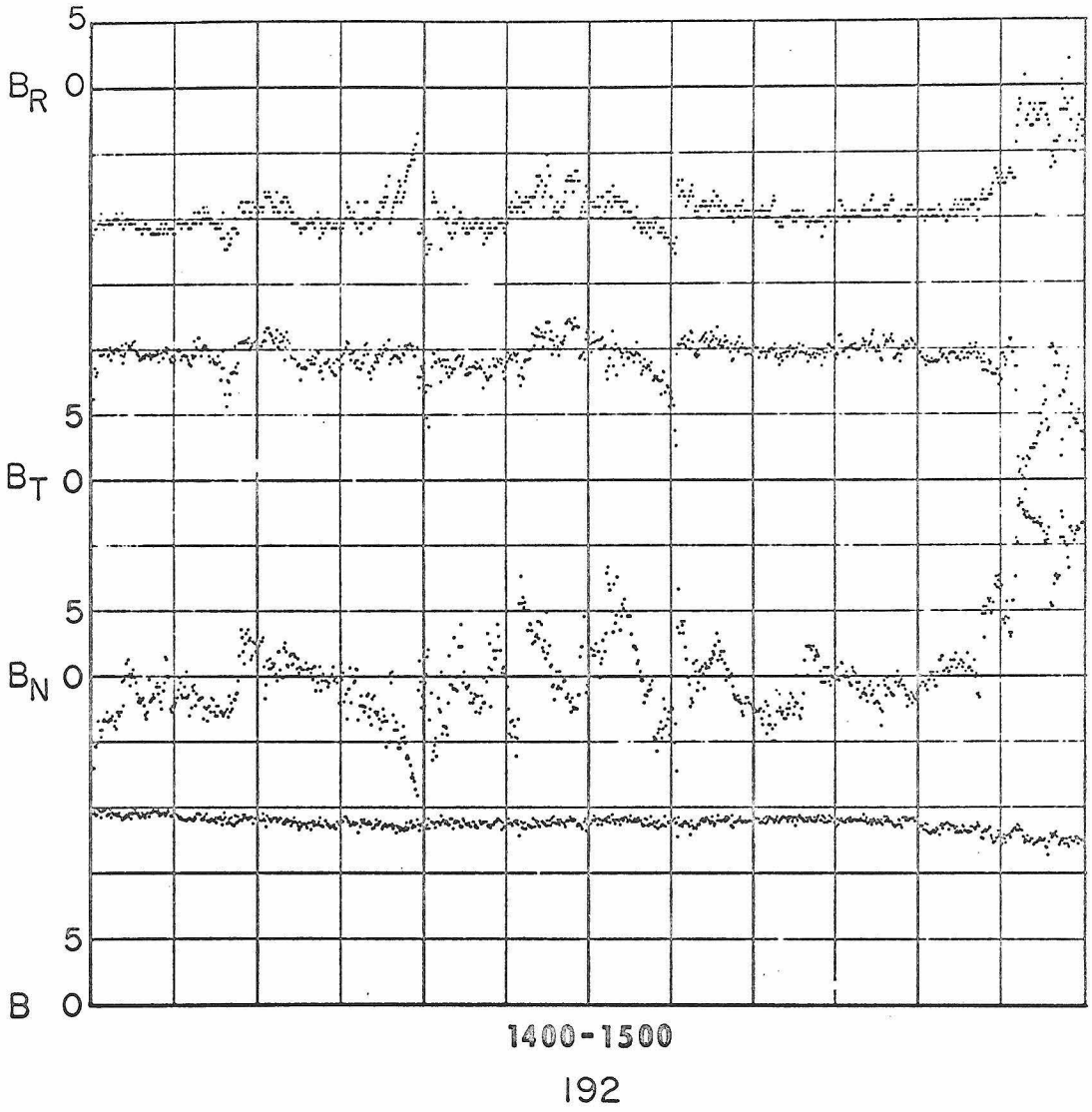

Figure 16. · High frequency magnetic fluctuations during a one hour period of day 192 showing clearly the large amount of power in the N direction.

CHAPTER IV

DISCUSSION OF OBSERVATIONS AND QUALITATIVE MODELS

A. Possible Origins of the Interplanetary Alfvén Waves

As we have seen, Alfvén waves occur quite often in the solar wind, and their energy densities are frequently comparable both to the unperturbed magnetic field energy density and to the thermal energy density. The origins and energy sources for these waves are thus of considerable interest, as is their contribution to the dynamics and heating of the solar wind. We consider three possibilities: (1) the waves are produced locally in the solar wind (in the same general region where they are observed) by internal plasma instabilities; (2) the waves are produced locally by large scale velocity differences in the solar wind; (3) the waves are remnants of processes occurring in the solar photosphere, chromosphere, or corona. We discuss these points in some detail, especially as they relate to the heating of the solar wind by means other than thermal conduction.

(1) Parker [1963] has pointed out that local thermal anisotropies due to the radial expansion of the solar wind should lead to "internal" plasma instabilities and subsequent wave generation. It is not immediately apparent that waves generated by such instabilities would propagate predominantly outward along field lines, although such preferential generation might, for example, stem from the high energy tail of the thermal proton distribution (which is outward along field lines [Hundhausen et al., 1967]). However, plasma instabili-

ties such as the firehose instability [Parker, 1963; Scarf, Wolfe, and Silva, 1967] do not efficiently generate waves with wavelengths many orders of magnitude longer than the ion cyclotron radius (~100 km). As the dominant wavelengths at issue are on the order of 10^6km, with decreasing power at shorter wavelengths, it seems unlikely that internal plasma instabilities are of importance in their generation.

(2) Several models have been proposed in which large scale velocity differences in the solar wind provide the basic energy source for the microscale fluctuations. In the analysis of the Mariner II data, it was suggested [Neugebauer and Snyder, 1966; Davis, et al, 1966] that the heating and high magnetic field activity found in the compression regions at the leading edges of high velocity streams were generated locally by the faster streams overtaking and colliding with slower streams. Jokipii and Davis [1969] pointed out the importance of such stream-stream collisions as a source of wave and thermal energy in the solar wind. They noted that if the collisions are predominantly between clouds moving radially, the compression will be mainly in the radial direction, and this will produce more fluctuations in the transverse than the radial component of the magnetic field, in accord with observations (Table 8) [Coleman, 1966; Siscoe et al, 1968]. It seems quite plausible that the high level of magnetic field activity in colliding stream regions is freshly generated, but there is no obvious reason to expect waves produced in this manner to propagate predominantly outward in the rest frame of the wind.

The relatively smaller amplitude fluctuations away from such regions might also be related to this type of generation process, al-

though there are major difficulties with this view. As Burlaga and Ogilvie [1970] point out, colliding stream regions occur infrequently and are of relatively limited spatial extent at 1 a. u. (cf. Figure 3). Alfvén waves generated in these regions cannot leave them faster than the Alfvén velocity, and hence can propagate at most of the order of .1 a. u. away from their point of generation by the time the solar wind reaches 1 a. u. As will be seen below, field lines tend to make a rather small angle with the interface between high and low velocity regions, and hence waves that propagate along field lines leave the interface at a normal velocity that is much less than the Alfvén velocity. Thus Alfvén waves in the main body of a stream well away from regions of rapid velocity increase (greater than 12 hours away in the spacecraft frame) cannot be associated with waves generated in those regions. This is especially true of Alfvén waves in high velocity streams, since these waves are propagating toward the collision region rather than away from it. Observationally, the level of the field fluctuations usually drops abruptly immediately outside the colliding stream regions, as can be seen in Figures 6, 8, and 10, for example. It thus appears [Burlaga et al, 1970] that the large amplitude fluctuations found in the colliding stream regions cannot effectively propagate away from them.

It could be argued that fine scale velocity differences near the sun might produce waves but be completely eliminated by the time the solar wind has reached 1 a. u., leaving behind Alfvén waves and enhanced temperatures in the main body of the streams. It is unlikely,

however, that such a process will have occurred on the trailing edges of the high velocity streams where the velocity is decreasing with time, even though we observe reasonably pure Alfvén waves in these regions. There is also no convincing reason to expect such collisions to generate Alfvén waves propagating exclusively outward in the rest frame of the wind. Thus although there is little question that stream-stream collisions are an important energy source for the large amplitude waves actually found in the colliding stream regions, it seems implausible that they are also responsible for the relatively smaller amplitude Alfvén waves found in the main body of velocity streams.

In a somewhat different approach that does not emphasize colliding stream regions, Coleman [1968] has proposed a turbulent model of the solar wind in which all large scale differential velocities feed energy into a hierarchy of turbulent eddies through instabilities associated with the shear and compression of the plasma. The fluid is treated as uniformly turbulent with a non-linear cascade of energy through Alfvénic turbulence of intermediate wavelengths, where there is little dissipation, to very short wavelengths, where cyclotron damping converts the wave energy into thermal energy. As above, the major objection to such a model is the lack of an explanation for the predominantly outward propagation of the observed fluctuations. Also, in a collisionless magnetized plasma, the coupling between waves of different wave numbers seems likely to be quite different from that for the waves in fluids where conventional turbulence theory applies.

In summary, it appears that unless a plausible explanation for preferentially outward wave generation is advanced (and this seems unlikely), large scale velocity differences in the solar wind cannot be considered a primary energy source for the Alfvén waves observed at 1 a.u. However, such velocity differences in the solar wind streams do represent a potentially major source of energy for the microscale fluctuations, and may eventually become the dominant energy source beyond 1 a.u.

(3) It is commonly accepted that the solar corona is heated by the dissipation of magnetoacoustic wave energy generated at the photosphere [Van de Hulst, 1953]. Estimates of the energy requirements for heating the solar chromosphere and lower corona are 5×10^{29} ergs/sec and 5×10^{27} ergs/sec, respectively [Osterbrook, 1961]. The Alfvén waves observed at 1 a.u. represent a net outward efflux of energy on the order of 3×10^{24} ergs/sec, and can reasonably be viewed as the undamped remnants of waves produced at or near the sun. Recent theoretical work [Barnes, 1966] indicates that linear magnetoacoustic MHD waves are strongly damped in collisionless plasmas such as the solar wind (moderate to high β), and that the Alfvénic mode is undamped. Thus, by the time the solar wind reaches .7 to 1 a.u. we would expect to observe only the Alfvénic remnants of what is perhaps a much broader spectrum of MHD waves generated closer to the sun. As long as the waves are produced at distances from the sun of less than Alfvénic critical point (15-50$R_\odot$ [Weber and Davis, 1967], only those Alfvén waves propagating away

from the sun will eventually appear in the superalfvénic solar wind. Generation of the observed Alfvén waves inside the Alfvénic critical point thus easily accounts for their preferential direction of propagation in the interplanetary medium. The waves can easily survive until they reach 1 a.u. since they are convected about ten times as fast as they propagate and hence make only on the order of 1 a.u./ 10λ oscillations for a wavelength of λ. For a wave of wavelength .01 a.u. this is only 10 oscillations.

The hypothesis that the interplanetary Alfvén waves are the remnants of "noise" introduced into the solar corona near the sun is an interesting one, since it suggests the possibility of monitoring small-scale solar activity from the orbit of the earth [Parker, 1965]. This possibility has important implications with regard to current theories of the heating of the solar wind by mechanisms other than thermal conduction. It is generally agreed that the solar wind requires an extended heat source above the base of the corona; if the only energy transport from the base of the corona is conduction and convection, the calculated density at the orbit of the earth in the two fluid model is too high, and both the velocity and proton temperature too low, as compared with observations [Sturrock and Hartle, 1966]. It has been suggested [Parker, 1969] that the energy equation of the solar wind is dominated near the sun by the transport and deposition of energy by waves. Barnes [1968, 1969] has proposed a model of solar wind proton heating by eventual dissipation of MHD waves generated at less than $1.5 R_{\odot}$, and Hartle and Barnes [1970] have shown

that a heat source for protons added to the two fluid solar wind model can increase both the proton temperature and the wind speed and lower the density at 1 a.u. if the energy disposition takes place over an extended range ($2R_\odot \leq r \leq 25\ R_\odot$). In this model, more active regions of the sun with a higher level of wave generation could cause extensive heating of the corona by wave damping near the sun, thus producing solar wind streams with higher velocities and proton temperatures and lower densities as compared to streams without such heating. The higher level of pure, outwardly propagating Alfvénic wave energy observed in the high velocity streams can easily be interpreted as a signature of this process, since the purely outwardly propagating waves in the main body of the streams are very probably a direct consequence of "turbulent" conditions near the sun. The observational fact that the largest amplitude waves occur at the leading edges of the high velocity streams where the velocity is increasing rapidly (but before it is at a maximum) at first seems inconsistent with this model, since we would naively expect the highest wave amplitudes to be associated with the highest velocities. However, local wave generation and amplification due to compression at the leading edges of the high velocity streams can account for this, as we shall see in the next section. It seems most probable that the exclusively outwardly propagating Alfvén waves found in the main bodies of solar wind streams, away from sharp velocity changes, are generated in the vicinity of the sun. Alfvén waves which cannot be definitely said to propagate exclusively outward, such as those found in colliding

stream regions, may be generated locally to a large extent.

B. Quasi-Stationary Stream Structure in the Solar Wind

On the basis of the discussion in points (2) and (3) above, and taking into account observed patterns in the solar wind stream structure, we would like to suggest a qualitative model for the observed properties of the interplanetary Alfvén waves and their relation to the large scale structure of the interplanetary medium. First, we interpret the presence of high velocity, high proton temperature, low density streams in the solar wind as a probable result of extensive proton heating by wave damping near the sun; streams in which there has been a smaller amount of such heating have lower velocities and proton temperatures, higher densities, and less easily detectable Alfvén waves. The occurrence of larger amplitude, purely outwardly propagating Alfvén waves in the main bodies of the high velocity streams is presumed to be a consequence of this heating process. The streaming pattern of a non-rotating sun would be quite simple, consisting of a number of (non-circular) cones containing high velocity, low density, hot gas (with a high level of outward Alfvén wave activity) separated by low velocity, low temperature, dense gas (with a lower level of Alfvén wave activity). The rotation of the sun complicates this picture considerably. Solar rotation causes slow gas to be followed by fast, and fast by slow on the same radial line. The fast streams overtake the slow streams ahead, causing compression, and draw away from the slower streams behind, causing rarefaction.

Figure 17 illustrates what we consider to be the major fea-

Figure 17. Top half, two high velocity streams and adjacent low velocity streams shown at one instant of time for the steady state case. Dotted lines represent ideal spiral magnetic field lines and are also the flow lines for the steady state flow in the corotating frame. Botton half, curves showing as functions of time the changes in solar wind properties which will be observed by a spacecraft as the streaming pattern sweeps past. σ_S, V_T, V_W, N, and B are as defined above, and V_φ is the T component of the solar wind velocity.

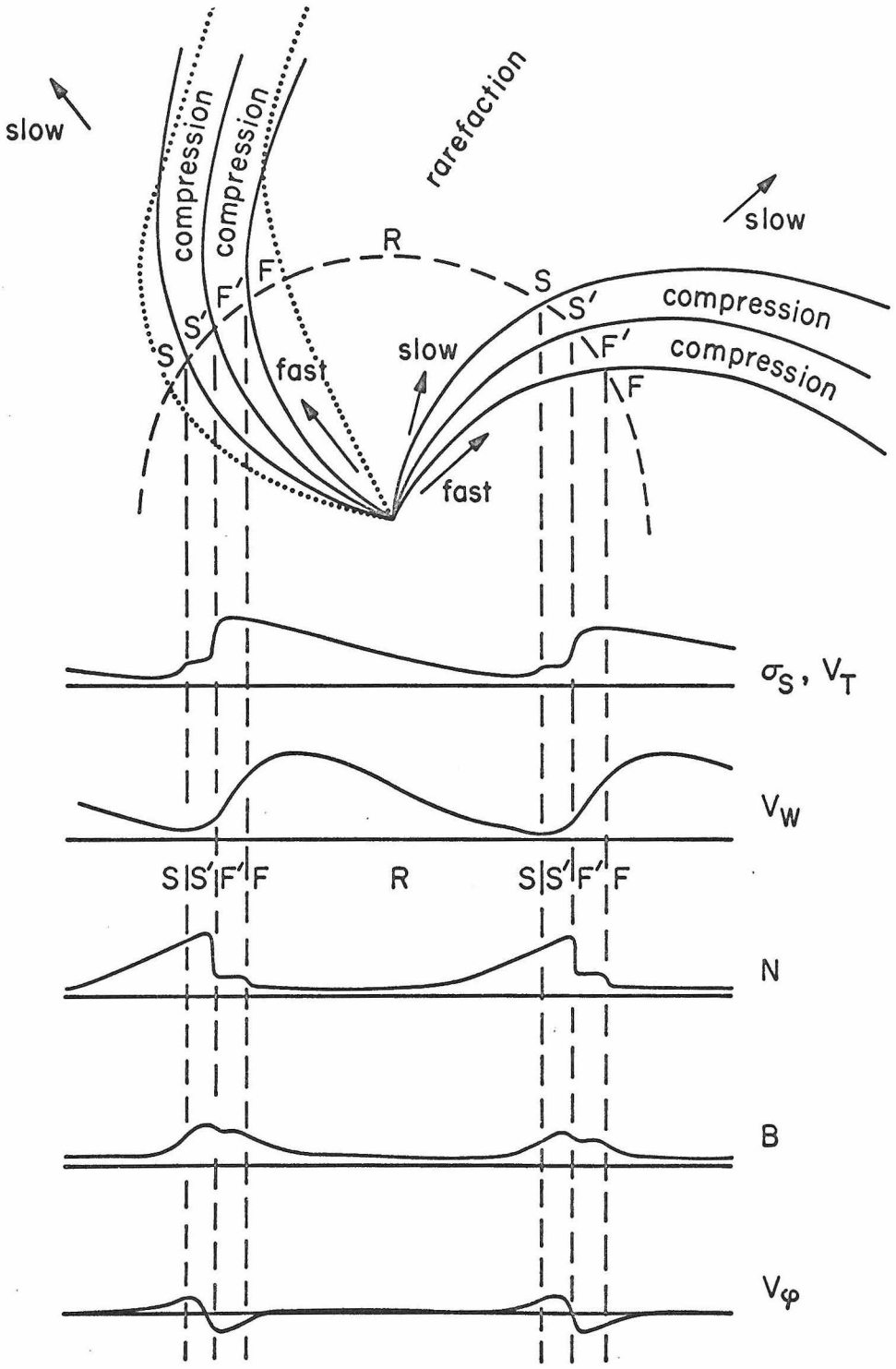
slow
compression
compression
rarefaction
slow
R
S
S′
F
F′
compression
compression
S
S′
F′
F
slow
fast
fast
σ_S, V_T
V_W
S S′ F′ F
R
S S′ F′ F
N
B
V_φ

Figure 17

tures of the interaction between high and low velocity streams, assuming that the structures are long lived enough to be considered as quasi-stationary and corotating. The labeled regions in the upper half of Figure 17 have different physical characteristics. In the older, conventional double shock models [Dessler and Fejer, 1963; Davis, 1966] they would be separated by shocks or contact surfaces; for the present discussion it does not matter whether the lines in the figure represent discontinuities, extended collisionless shock structures, or more or less continuous transition zones. Region S is the unperturbed slow stream and region F the fast stream followed by another slow stream. Region S' is the slow stream gas compressed and accelerated by the collision and region F' is the compressed and decelerated fast stream gas. The velocity vectors shown are those in an inertial frame; in this frame, the figure rotates with the sun.

It is instructive to consider this steady state flow in a rotating coordinate system. The structure in the upper half of Figure 17 now does not rotate; instead, the spacecraft moves clockwise in a circle and makes observations which, when plotted as functions of time, yield the idealized curves shown in the bottom half of the figure. In this corotating frame, the velocity is everywhere parallel to the smoothed magnetic field lines, and hence the flow is in a spiral whose pitch changes as it passes into the regions of compression because of the pressure gradient (or discontinuity) across the transition. The deflection provides a natural explanation for the observations [Lazarus, 1970; Wolfe, 1970] that in a region such as S' the solar

wind appears to come from east of the sun while in a region such as F' it appears to come from the west. This aspect of the model is very similar to that of Siscoe, Goldstein and Lazarus [1969] except that they do not emphasize the distinction between the compressed interaction regions and the remainder of the fast and slow streams.

The flow along the magnetic spirals is from F to F' and from S to S'. In each case, the gas is compressed in the transition, and in the simple double shock model both transitions are ordinary fast shocks while the S'F' interface is a tangential discontinuity. The F to F' shock appears to be running backward toward the sun into a low density region, and hence is often called a reverse shock. Because of the compression, both primed regions will have higher temperatures, densities, and field strengths than do the adjacent unperturbed gases in their respective streams. Typically, the fast stream is decelerated more in going from F to F' than the slow stream is accelerated in going from S to S', since the slow stream is more dense.

Although the simplest theoretical model is that of the ideal double shock, the observations rarely if ever show the expected discontinuities in velocity, density, and magnetic field. Either this represents a thicker than expected shock structure or there are no shocks and instead a continuous transition produced by some as yet unexplained mechanism. In either case, the Rankine-Hugonoit conservation theorems must hold across the transition, and most of the results of the simple shock analysis should be good approximations. Ideally, S' and F' are separated by a tangential discontinuity which

neither plasma nor field lines cross, and in practice this can often be recognized as an abrupt change in density, temperature, and wave amplitude (for example see Figure 7, day 236, hour 12). The fact that the larger amplitude Alfvén waves from the fast stream appear to be confined to the fast stream side of this boundary (cf. Figure 8) is a strong indication that the field lines do not cross the boundary between the fast and slow streams.

In region R of Figure 17 there should be a rarefaction, causing a relative decrease in density in the leading part of the slow and the trailing part of the fast stream. The net result of the compression and rarefaction is the production of an asymmetry in the shape of the streams, as indicated in the lower part of Figure 17, that increases with the distance from the sun. This asymmetry in the streaming patterns, as well as many other features of the model, can be seen both in the observational data presented above (cf. Figures 3, 4, 7, 9, and 11) and in the earlier Mariner 2 data [Neugebauer and Snyder, 1966]. We emphasize that in this model the increased density usually observed ahead of fast streams (Regions S and S′) is for the most part not the result of the pileup of ambient gas ahead of the fast stream. Rather, it is primarily due to the fact that the energy supply at the base of the solar wind for the slow gas which precedes the fast is such as to produce higher densities in the slow gas (as well as lower velocities and temperatures) at 1 a.u.

Imp I data, organized by Wilcox and Ness [1965] on the basis of the magnetic sector structure, i.e., the magnetic polarity, rather than the stream structure, also exhibit patterns similar to the curves

in the lower half of Figure 17. The two methods of analysis give similar results because, in the case of the Imp I data, polarity reversals occur near the center of the prominent low velocity regions and there is a strong tendency for each high velocity stream to occupy its own sector. At the times of Mariners 2 and 5 this was not the case, since two or more adjacent high velocity streams have the same magnetic polarity. In these cases analysis based on solar wind velocity characteristics gives clearer patterns than does the use of magnetic polarity. This is plausible since the variations in energy supply associated with velocity variations are likely to be more basic than are changes in magnetic polarity. An explanation is needed for the observation that reversals of polarity apparently occur predominantly in low velocity regions. Perhaps the magnetic configuration in the lower corona near polarity reversals affects the energy supply to the solar wind in such a way as to favor low velocities.

The effect on the microscale fluctuations of the compressed regions in this quasi-stationary large scale streaming structure will be both to amplify existing waves and to generate fresh waves locally. Large amplitude, outwardly propagating Alfvén waves in region F propagate and are convected into region F'. If the Alfvén waves are initially polarized in the $\underset{\sim}{e}_N$ direction, then they will remain purely Alfvénic as they are swept into F' since their magnetic field fluctuations remain perpendicular to the average field direction. If they are polarized in the solar equatorial plane, they will be partially converted into magnetoacoustic waves because of the abrupt turning

of the field lines in this plane across the transition (see Figure 17).

In any case, the amplitude of the waves will increase across the transition because of the compression. In the colliding stream region on day 192 (Figure 4), for example, we see a considerable increase in the amplitude of the waves as the compression region is entered (around hour 21 in Figure 6), although they remain predominantly outwardly propagating across the transition (Figure 5). If the transition between F and F' is smooth compared to a wavelength, we would expect the waves convected into F' to still be outwardly propagating. If the transition is an ideal thin shock, an outwardly propagating wave will produce both outwardly and inwardly propagating waves as it passes the discontinuity. However, the latter wave remains in F' and is not reflected back into region F, as would be the case for a discontinuity in a non-streaming medium, since the streaming velocity in a system in which the interface is stationary is faster than the wave velocity on the F side of the interface. Thus the waves cannot escape from F' to F and Alfvén waves cannot escape into S' because the field lines do not cross the tangential discontinuity at the interface. Leakage out of the region F' is perhaps possible only because of the finite dimensions of the region normal to the field lines or by the partial conversion of the Alfvén mode into the magnetoacoustic modes. Thus Alfvén waves from F will be swept into F', amplified by compression, and channeled outward along the compressed leading edge of the high velocity stream. We should expect this same general effect for waves swept from S into S', although it should not

be as pronounced since the waves convected from S into S' are typically of smaller amplitude than those in F.

At each transition we expect that the collision will, in addition to amplifying the convected Alfvén waves, generate additional fluctuations. These will presumably be a mixture of Alfvén and magnetoacoustic modes propagating both inward and outward. Again, these freshly generated waves will be primarily confined to the colliding stream region. Thus the total wave structure in the colliding stream regions will consist of higher amplitude fluctuations which are not as purely Alfvénic or outwardly propagating as are waves in the neighboring regions.

It appears that all of the observed properties of waves in the solar wind follow naturally from this model. Most of the waves in the interplanetary medium are outwardly propagating Alfvén waves from near the sun, and are remnants of the processes that supply energy to drive the different solar wind streams. Higher velocity streams undergo the most extensive heating, and thus contain the best examples of such waves. Compression of these waves and fresh generation of new fluctuations in colliding stream regions account for the waves with the largest observed amplitudes.

C. The Microscale Anisotropies and Wave Damping

The analysis of the observational data has revealed a number of anisotropies in the microscale magnetic fluctuations whose physical basis we now consider. The main points to be explained are that the minimum component of the fluctuations is parallel to $\underset{\sim}{e}_B$, the

direction of the average magnetic field, and that the maximum component is in the $\underset{\sim}{e}_B x \underset{\sim}{e}_R$ direction, where $\underset{\sim}{e}_R$ may be regarded as the direction of the solar wind flow. The first of the anisotropies is explained by the predominantly Alfvénic nature of the fluctuations. Thus we wish to understand why the Alfvén waves dominate the magnetoacoustic modes, and why they are partially polarized in the $\underset{\sim}{e}_B x \underset{\sim}{e}_R$ direction. Such properties may be due either to the mechanisms which generate the waves or to decay mechanisms.

It is unlikely that Alfvén waves are dominant solely because the magnetoacoustic modes are not generated strongly. In colliding stream regions, for example, we expect to see all types of hydromagnetic waves produced, but the fluctuations are primarily Alfvénic (little variance in field strength compared to large variance in components). Even if Alfvén waves are preferentially generated, we would expect them to excite magnetoacoustic modes either because of non-linearities in the equations of motion or because of geometrical considerations (a pure Alfvén wave must extend to infinity in the plane of polarization). Thus the observations suggest that magnetoacoustic modes must be damped at a rate sufficient for their reasonably complete removal from waves convected from near the sun and for partial removal from more locally generated waves. Barnes [1966] has shown theoretically that linear magnetoacoustic MHD waves are strongly damped in collisionless plasmas of moderate to high β ($\beta > .5$) and that the Alfvén mode is undamped. Thus this theory both explains and is confirmed by the observations.

There appears to be no plausible anisotropy in the generation of the Alfvén waves which would favor the $\underset{\sim}{e}_B x \underset{\sim}{e}_R$ direction. Thus we examine mechanisms which couple the undamped Alfvén waves into the strongly damped magnetoacoustic modes. For example, consider the convection away from the sun of Alfvén waves which are initially unpolarized. Assume that the magnetic field fluctuations are isotropic in the plane perpendicular to an average magnetic field along the classic spiral. As the waves are convected outward, the rotation of the sun causes the average field to turn in the plane normal to $\underset{\sim}{e}_N$ as the spiral is generated. The component of the Alfvén waves originally polarized along $\underset{\sim}{e}_N$ is unaffected by this turning since it always remains normal to $\underset{\sim}{e}_B$; however, the component originally along $\underset{\sim}{e}_B x \underset{\sim}{e}_N$ develops a component along $\underset{\sim}{B}$, and hence is coupled into magnetoacoustic modes. Thus the gradual spiraling of the field combined with the damping of the magnetoacoustic modes converts an initially isotropic distribution of Alfvén waves into one having more power along $\underset{\sim}{e}_N$.

If the average magnetic field is not along the ideal spiral then the expansion of the solar wind in the direction normal to $\underset{\sim}{e}_R$ as it flows outward will turn the field vector in a plane whose normal is $\underset{\sim}{e}_B x \underset{\sim}{e}_R$. The mechanism just described then produces an anisotropy in the $\underset{\sim}{e}_B x \underset{\sim}{e}_R$ direction. The $\underset{\sim}{e}_B x \underset{\sim}{e}_R$ and the $\underset{\sim}{e}_N$ directions are in general close to each other unless $\underset{\sim}{e}_B$ has a large component out of the solar equatorial plane; in this case, it is the $\underset{\sim}{e}_B x \underset{\sim}{e}_R$ direction that is the preferred one, and not the $\underset{\sim}{e}_N$ direction. The fact that the aver-

age field direction frequently has significant components out of the equatorial plane explains why the R component of the fluctuations on the average has less power than the T component (Table 8), since the $\hat{e}_B x \hat{e}_R$ direction never has a component along $\underset{\sim}{e}_R$, whereas it can easily have a component along $\underset{\sim}{e}_T$ if $\underset{\sim}{e}_B$ has a component along $\underset{\sim}{e}_N$. Earlier studies of Mariner 2 and Mariner 4 data [Coleman, 1967; Siscoe, 1968] have shown that the microscale field fluctuations are transverse to the average field direction with minimum power along $\underset{\sim}{e}_R$. These results are confirmed by the Mariner 5 data, and are seen to be a natural consequence of the frequent occurrence of transverse Alfvén waves partially polarized in the $\underset{\sim}{e}_B x \underset{\sim}{e}_R$ direction.

Alfvén waves convected into colliding stream regions will see a rapid change in the average field direction across the transition into the compressed plasma (see Figure 17). This more abrupt change in field direction (as compared to the gradual spiraling described above) should result in enhanced anisotropies and a higher level of (rapidly damped) magnetoacoustic oscillations, as observed. Another process suggested by J. R. Jokipii (private communication) that could contribute to the $\underset{\sim}{e}_B x \underset{\sim}{e}_R$ anisotropy in these regions is the probability that radially colliding streams produce primarily radial compressions and hence amplify magnetic fluctuations primarily normal to $\underset{\sim}{e}_R$. Those fluctuations along $\underset{\sim}{e}_B x \underset{\sim}{e}_R$ are pure Alfvén waves while those along $\underset{\sim}{e}_R x (\underset{\sim}{e}_B x \underset{\sim}{e}_R)$ must become mixed Alfvénic and magnetoacoustic modes. The latter are rapidly damped leaving the anisotropy and a higher plasma temperature.

The interpretation of the $\underset{\sim}{e}_B x \underset{\sim}{e}_R$ anisotropy as a result of magnetoacoustic wave damping has interesting implications with respect to the heating of the solar wind. The observational fact that the anisotropy extends over the entire microscale frequency range supports the conclusions of Jokipii and Davis [1969] that turbulence in the solar wind (such as in colliding stream regions) has no equilibrium subrange of wave numbers, in contrast to ordinary turbulence. Instead of a cascade of energy to shorter and shorter wave numbers [Coleman, 1968], it appears that all wavelengths damp by direct interaction with the thermal plasma. The fact that this anisotropy is essentially always present implies that there is a continuous coupling between the dynamic microscale fluctuations and the thermal plasma which feeds energy out of wave motion and into thermal energy. We note also that the type of damping described above is essentially a geometrical coupling of Alfvén waves to the fast MHD mode propagating at a small angle with respect to the magnetic field (assuming $\beta < 1$). Damping of the fast MHD mode at this angle increases the proton temperature parallel to the magnetic field by resonant Landau damping between the thermal protons and the wave [Barnes, 1966]. Since the observed Alfvén waves propagate predominantly outward, we would expect damping of the waves to heat thermal protons moving outward along the field lines, since it is these protons which resonate strongly with the waves. Thus, damping of the outwardly propagating Alfvén waves will contribute to the high energy tail of the proton thermal distribution [Hundhausen, 1967]. In the

rest frame of the wind, the Alfvén waves transport energy outward at the rate $V_A(\delta B)^2/8\pi$, where δB is the wave amplitude and V_A is the Alfvén velocity. If we assume that the 5:4:1 $\underset{\sim}{e}_B \times \underset{\sim}{e}_R$ anisotropy commonly observed at 1 a.u. means that 10 percent of the energy in the Alfvén waves at 1 a.u. has already been transferred by damping to the protons, we would expect to see an energy transport rate due to the high energy tail of the proton distribution of about 10^{-5} ergs/cm^2 sec for an Alfvén velocity of 50 km/sec and a wave amplitude of 2γ. This is just the rate for the proton distribution found by Hundhausen [1967].

CHAPTER V

A WAVE DRIVEN SOLAR WIND MODEL

The observational studies presented above indicate that a large fraction of the Alfvén waves in the interplanetary medium are generated at or near the sun. The detailed behavior of these waves and their effect on the dynamics of the expanding solar corona as they propagate and are convected out into the interplanetary medium is of considerable interest. Let us examine the properties of solutions to a steady state MHD polytrope solar wind model which includes wave energy fluxes, using the WKB approximation for the wave amplitudes, with no wave damping. We assume spherical symmetry, with no solar rotation. In sections A and B of this chapter we develop the mathematical details of the model, and in section C we consider numerical solutions to the equations and physical interpretations. The presence of the coronal Alfvén waves modifies the standard Bernoulli relation, and under most conditions can cause significant changes in the large scale streaming properties of the solar wind.

A. The WKB Wave Amplitudes

For an MHD plasma with fluid velocity $\underset{\sim}{V}$, mass density ρ, thermal pressure p, and magnetic field $\underset{\sim}{B}$, the appropriate Maxwell equations and the relevant equations of motion in the presence of a spherically symmetric gravitational potential Φ are

$$\rho\left(\frac{\partial}{\partial t} + \underset{\sim}{V}\cdot\underset{\sim}{\nabla}\right)\underset{\sim}{V} + \underset{\sim}{\nabla}p + \underset{\sim}{\nabla}B^2/8\pi - (\underset{\sim}{B}\cdot\underset{\sim}{\nabla})\underset{\sim}{B}/4\pi + \rho\underset{\sim}{\nabla}\Phi = 0 \tag{1}$$

$$\frac{\partial}{\partial t}(\underset{\sim}{B}) = \underset{\sim}{\nabla} \times (\underset{\sim}{V} \times \underset{\sim}{B}) \tag{2}$$

$$\frac{\partial}{\partial t}(\rho) + \underset{\sim}{\nabla}\cdot(\rho\,\underset{\sim}{V}) = 0 \tag{3}$$

$$\underset{\sim}{\nabla}\cdot\underset{\sim}{B} = 0 \tag{4}$$

where

$$\Phi = -\frac{GM_\odot}{r} \tag{5}$$

We assume a polytrope relation between p and ρ

$$p = p_o\left(\frac{\rho}{\rho_o}\right)^a \tag{6}$$

and look for solutions of Equations (1) through (4) of the form

$$\begin{aligned} \underset{\sim}{V} &= V_r(r)\,\underset{\sim}{e}_r + \delta\underset{\sim}{V}(r,t) \\ \underset{\sim}{B} &= B_r(r)\,\underset{\sim}{e}_r + \delta\underset{\sim}{B}(r,t) \\ \rho &= \rho(r) \end{aligned} \tag{7}$$

where $\delta\underset{\sim}{V}$ and $\delta\underset{\sim}{B}$ are Alfvénic perturbations which are transverse to the radial direction. In the following derivation, we assume that the waves are linearly polarized, although the results are equally valid for other polarizations. Since we assume $\delta\underset{\sim}{V}$ and $\delta\underset{\sim}{B}$ are Alfvénic, they are parallel, and cause no perturbations in density or pressure. We consider Equations (1) through (7) in the equatorial plane of a spherical polar coordinate system. In this plane, the r- component

of Equation (1) is

$$V_r \frac{\partial V_r}{\partial r} - \frac{\delta V^2}{r} + \frac{1}{\rho} \frac{\partial p}{\partial r} + \frac{1}{8\pi\rho r^2} \frac{\partial}{\partial r} (r\delta B)^2 + \frac{\partial \Phi}{\partial r} = 0 \qquad (8)$$

The component of Equation (1) transverse to the radial direction is

$$\frac{\partial}{\partial t} (\delta V) + \frac{V_r}{r} \frac{\partial}{\partial r} (r\delta V) = \frac{B_r}{4\pi\rho r} \frac{\partial}{\partial r} (r\delta B) \qquad (9)$$

Equations (3) and (4) are simply

$$\frac{1}{r^2} \frac{\partial}{\partial r} (r^2 \rho V_r) = 0 \qquad (10)$$

and

$$\frac{1}{r^2} \frac{\partial}{\partial r} (r^2 B_r) = 0 \qquad (11)$$

The radial component of Equation (2) is identically zero, and the transverse component is

$$\frac{\partial}{\partial t} (\delta B) = \frac{1}{r} \frac{\partial}{\partial r} \left[r (B_r \delta V - V_r \delta B) \right] = (B_r \frac{\partial}{\partial r} \delta V - V_r \frac{\partial}{\partial r} \delta B)$$
$$+ \frac{1}{r} (V_r \delta B - B_r \delta V) + \frac{V_r \delta B}{\rho} \frac{\partial \rho}{\partial r} \qquad (12)$$

where we have used Equations (10) and (11) to obtain the final form in Equation (12).

The WKB solution for the wave amplitudes can be obtained from the transverse Equations (9) and (12). Let h be the scale length for variations in ρ, V_r, and B_r

$$h \simeq \left[\frac{1}{\rho} \frac{\partial \rho}{\partial r} \right]^{-1}$$

We assume that δB and δV are of the form

$$\delta B(r,t) = \left[\delta B_1(r) + \mu\delta B_2(r) + \mu^2\delta B_3(r) + \ldots\right] e^{i(S(r)-\omega t)}$$

$$\delta V(r,t) = \left[\delta V_1(r) + \mu\delta V_2(r) + \mu^2\delta V_3(r) + \ldots\right] e^{i(S(r)-\omega t)} \tag{13}$$

where

$$\mu = \frac{2\pi}{kh}$$

$$k = \frac{\partial S}{\partial r} \tag{14}$$

The parameter μ is the ratio of the Alfvén wavelength to the scale length of ρ, B_r, and V_r, and is taken to be small. δB_1, δB_2, δV_1, etc., are also assumed to have scale lengths on the order of h. Inserting Equation (13) into (9) and (12), and keeping terms to first order in μ, we have

$$\left[(ikV_r - i\omega)\delta V_1 - \frac{ikB_r}{4\pi\rho}\delta B_1\right] = -\left[(ikV_r - i\omega)\delta V_2 - \frac{ikB_r}{4\pi\rho}\delta B_2\right]\mu$$

$$+\left[\frac{B_r}{4\pi\rho}\frac{\partial}{\partial r}(\delta B_1) - V_r\frac{\partial}{\partial r}(\delta V_1)\right] + \left[\frac{B_r}{4\pi\rho r}(\delta B_1) - \frac{V_r}{r}(\delta V_1)\right] \tag{15}$$

$$\left[(ikV_r - i\omega)\delta B_1 - ikB_r\delta V_1\right] = -\left[(ikV_r - i\omega)\delta B_2 - ikB_r\delta V_2\right]\mu$$

$$+\frac{1}{r}\left[V_r\delta B_1 - B_r\delta V_1\right] + \frac{V_r\delta B_1}{\rho}\frac{\partial\rho}{\partial r} + \left[B_r\frac{\partial}{\partial r}(\delta V_1) - V_r\frac{\partial}{\partial r}(\delta B_1)\right] \tag{16}$$

where we have assumed that $r \gtrsim h$. The left hand sides of Equations (15) and (16) are of zeroth order in μ, and the right hand sides are of first order. The zeroth order approximation is obtained by assuming

the right hand sides are zero. This yields the solutions

$$\omega = k\left(V_r \pm \frac{B_r}{(4\pi\rho)^{\frac{1}{2}}}\right)$$
$$\delta V_1 = \mp \frac{\delta B_1}{(4\pi\rho)^{\frac{1}{2}}} \tag{17}$$

where the upper (lower) sign in Equation (17) corresponds to outwardly (inwardly) propagating waves. In the first order approximation, we insert the zeroth order solutions (17) into Equations (15) and (16), and keep terms to first order in μ. Taking the upper sign in Equation (17) for outward waves, we obtain

$$\begin{aligned} 0 = \mu\Bigg[& \frac{ikB_r}{(4\pi\rho)^{\frac{1}{2}}}\delta V_2 + \frac{ikB_r}{4\pi\rho}\delta B_2 \Bigg] \\ & + \left[\frac{B_r}{4\pi\rho}\frac{\partial}{\partial r}(\delta B_1) + V_r\frac{\partial}{\partial r}\left(\frac{\delta B_1}{(4\pi\rho)^{\frac{1}{2}}}\right)\right] \\ & + \frac{1}{r}\left[\frac{B_r}{4\pi\rho} + \frac{V_R}{(4\pi\rho)^{\frac{1}{2}}}\right]\delta B_1 \end{aligned} \tag{18}$$

$$\begin{aligned} 0 = \mu\Bigg[& \frac{ikB_r}{(4\pi\rho)^{\frac{1}{2}}}\delta B_2 + ikB_r\,\delta V_2 \Bigg] \\ & + \left[\frac{1}{r}\left(V_r + \frac{B_r}{(4\pi\rho)^{\frac{1}{2}}}\right) + \frac{V_r}{\rho}\frac{\partial\rho}{\partial r}\right]\delta B_1 \\ & - \left[B_r\frac{\partial}{\partial r}\left(\frac{\delta B_1}{(4\pi\rho)^{\frac{1}{2}}}\right) + V_r\frac{\partial}{\partial r}(\delta B_1)\right] \end{aligned} \tag{19}$$

The perturbations δB_2 and δV_2 can be eliminated by multiplying Equation (18) by $(4\pi\rho)^{\frac{1}{2}}$ and subtracting from Equation (19). This leaves a differential equation for δB_1 alone, which may be written in the form

$$\frac{1}{\delta B_1}\ \frac{\partial}{\partial r}(\delta B_1) = \frac{1}{4\rho}\ \frac{\partial \rho}{\partial r}\left(\frac{3V_r + V_A}{V_r + V_A}\right) \tag{20}$$

where

$$V_A = \frac{B_r}{(4\pi\rho)^{\frac{1}{2}}} \tag{21}$$

From Equations (10) and (11), we have

$$\begin{aligned} r^2 \rho V_r &= r_o^2 \rho_o V_o \\ r^2 B_r &= r_o^2 B_o \end{aligned} \tag{22}$$

where ρ_o, B_o, and V_o are values at the reference level r_o. It is readily seen that

$$\frac{V_A}{V} = \frac{V_A^{\,o}}{V_o}\left(\frac{\rho}{\rho_o}\right)^{\frac{1}{2}} \tag{23}$$

In Equation (23), we have dropped the r subscript from V_r; in the following, we write B and V for B_r and V_r, as there is no possibility of confusion. Inserting (23) into (20) and integrating gives

$$\delta B(r) = \delta B_o \left(\frac{\rho}{\rho_o}\right)^{3/4} \left[\frac{1 + \dfrac{V_A^{\,o}}{V_o}}{1 + \dfrac{V_A^{\,o}}{V_o}\left(\dfrac{\rho}{\rho_o}\right)^{\frac{1}{2}}}\right] \tag{24}$$

where V_A^o is the Alfvén velocity at the reference level, and $\delta B(r)$ is the wave amplitude at r in the WKB approximation. This expression was first obtained by Parker [1965].

B. The Wave Modified Bernoulli Relation

Inserting Equations (17) and (24) into Equation (8) and averaging over one wavelength of the waves yields

$$V\frac{\partial V}{\partial r} + \frac{1}{\rho}\frac{\partial p}{\partial r} + \frac{\partial \Phi}{\partial r} + \frac{1}{8\pi\rho}\frac{\partial}{\partial r}\left[\frac{\delta B_o^2}{2}\left(\frac{\rho}{\rho_o}\right)^{\frac{3}{2}}\frac{(1+V_A^o/V_o)^2}{\left(1+\frac{V_A^o}{V_o}(\rho/\rho_o)^{\frac{1}{2}}\right)^2}\right] = 0 \tag{25}$$

Using Equation (5) and (6), Equation (25) can be integrated to give

$$\frac{V^2}{2} + \frac{a}{(a-1)}\frac{p_o}{\rho_o}\left(\frac{\rho}{\rho_o}\right)^{a-1} - \frac{GM_\odot}{r} - \frac{\delta B_o^2}{8\pi\rho_o}\frac{V_o}{V_A^o}\left(1+\frac{V_A^o}{V_o}\right)^2\frac{\left(2+\frac{V_A^o}{V_o}\left(\frac{\rho}{\rho_o}\right)^{\frac{1}{2}}\right)}{\left(1+\frac{V_A^o}{V_o}\left(\frac{\rho}{\rho_o}\right)^{\frac{1}{2}}\right)^2} = \text{constant} \tag{26a}$$

If we add the constant $\frac{V_o}{V_A^o}\frac{\delta B_o^2}{4\pi\rho_o}\left(1+\frac{V_A^o}{V_o}\right)^2$ to both sides of Equation (26a), and multiply by the constant $(4\pi\rho Vr^2)$, we obtain after some manipulation an expression for the total energy flux F, which is constant for our solution.

$$F = 4\pi r^2 \left\{ V\left(\tfrac{1}{2}\rho V^2 + \frac{a}{(a-1)}\, p + \rho\Phi\right) + \tfrac{1}{2}\left(\tfrac{1}{2}\rho\delta V^2\right)V + \tfrac{1}{2}\frac{\delta B^2}{4\pi}(V + V_A) \right\} \tag{26b}$$

The first term in parenthesis contains terms corresponding to the kinetic energy density associated with the radial motion, the sum of the enthalpy and the energy transported by thermal conduction, and the gravitational energy, all convected at the bulk radial velocity V. The second and third terms are due entirely to the presence of the waves. The second is the wave kinetic energy density convected by the bulk velocity and the third is the radial component of the Poynting vector.

We define the quantities

$$\epsilon = \tfrac{1}{2}\left(\frac{\delta B_o}{B_o}\right)^2 \tag{27}$$

$$U^2 = \tfrac{1}{2}\frac{\rho_o}{p_o}\, V^2 \tag{28}$$

$$U_o^2 = \tfrac{1}{2}\frac{\rho_o}{p_o}\, V_o^2 \tag{29}$$

$$\beta_o = \frac{8\pi p_o}{B_o^2} \tag{30}$$

$$H = \frac{G M_\odot \rho_o}{r_o p_o} \tag{31}$$

$$Z = \frac{r}{r_o} \tag{32}$$

and note that

$$\frac{\rho}{\rho_o} = \frac{U_o}{UZ^2} \tag{33}$$

$$\left(\frac{V_o}{V_A^o}\right)^2 = \beta_o U_o^2 \tag{34}$$

Dividing Equation (26a) by p_o/ρ_o and using Equations (27) through (34), we obtain

$$U^2 + \frac{a}{(a-1)}\left(\frac{U_o}{UZ^2}\right)^{a-1} - \frac{H}{Z} - \frac{\epsilon}{\beta_o}\left(1 + U_o\beta_o^{\frac{1}{2}}\right)^2 \frac{\left(2U_o\beta_o^{\frac{1}{2}} + \left(\frac{U_o}{UZ^2}\right)^{\frac{1}{2}}\right)}{\left(U_o\beta_o^{\frac{1}{2}} + \left(\frac{U_o}{UZ^2}\right)^{\frac{1}{2}}\right)^2} \tag{35}$$

$$= U_o^2 + \frac{a}{(a-1)} - H - \frac{\epsilon}{\beta_o}\left(2U_o\beta_o^{\frac{1}{2}} + 1\right)$$

This is the wave modified Bernoulli relation.

Consider Equation (25). Using Equations (5) and (6) and performing the indicated differentiations gives

$$V \frac{\partial V}{\partial r} + \frac{a}{\rho} \frac{p_o}{\rho_o{}^a} \rho^{(a-1)} \frac{\partial \rho}{\partial r} + \frac{GM_\odot}{r^2}$$

$$+ \frac{\delta B_o{}^2 (1 + V_A{}^o/V_o)^2}{32\pi \rho^{\frac{1}{2}} \rho_o{}^{\frac{3}{2}}} \left\{ \frac{\left(3 + \frac{V_A{}^o}{V_o} \left(\frac{\rho}{\rho_o}\right)^{\frac{1}{2}}\right)}{\left(1 + \frac{V_A{}^o}{V_o} \left(\frac{\rho}{\rho_o}\right)^{\frac{1}{2}}\right)^3} \right\} \frac{\partial \rho}{\partial r} = 0 \qquad (36)$$

Dividing by $\frac{p_o}{r_o \rho_o}$ and using Equations (27) through (34), Equation (36) becomes

$$2U \frac{\partial U}{\partial Z} + \frac{1}{\rho} \frac{\partial \rho}{\partial Z} \left\{ a \left(\frac{U_o}{UZ^2}\right)^{a-1} \right.$$

$$\left. + \frac{\epsilon}{2\beta_o} \left(\frac{U_o}{UZ^2}\right)^{\frac{1}{2}} \left(1 + U_o \beta_o{}^{\frac{1}{2}}\right)^2 \frac{\left(3U_o \beta_o{}^{\frac{1}{2}} + \left(\frac{U_o}{UZ^2}\right)^{\frac{1}{2}}\right)}{\left(U_o \beta_o{}^{\frac{1}{2}} + \left(\frac{U_o}{UZ^2}\right)^{\frac{1}{2}}\right)^3} \right\} \qquad (37)$$

$$+ \frac{H}{Z^2} = 0$$

Equation (37) is of the form

$$2U \frac{\partial U}{\partial Z} + \frac{W}{\rho} \frac{\partial \rho}{\partial Z} + \frac{H}{Z^2} = 0 \qquad (38)$$

From Equation (10)

$$\frac{1}{\rho}\frac{\partial \rho}{\partial Z} = -\left(\frac{2}{Z} + \frac{1}{U}\frac{\partial U}{\partial Z}\right) \tag{39}$$

so that Equation (38) can be written as

$$\frac{\partial U}{\partial Z}\left\{2U - \frac{W}{U}\right\} = \left\{\frac{2W}{Z} - \frac{H}{Z^2}\right\} \tag{40}$$

The critical point of the differential equation for U(Z) occurs when both terms in bracketts in Equation (40) are simultaneously zero. The critical point (U_c, Z_c) thus satisfies

$$2U_c = \frac{W(U_c, Z_c)}{U_c}$$

$$\frac{2W(U_c, Z_c)}{Z_c} = \frac{H}{Z_c^2}$$

so that

$$U_c^2 = \frac{H}{4Z_c} \tag{41}$$

and

$$\frac{H}{2Z_c} = W(U_c, Z_c)$$

Using Equation (37) for W, we find that (U_c, Z_c) satisfies

$$U_c^2 = \frac{H}{4Z_c} \tag{42a}$$

$$\frac{H}{2Z_c} = a\left(\frac{2U_o}{H^{\frac{1}{2}}Z_c^{\frac{3}{2}}}\right)^{a-1} +$$

(42b)

$$+ \frac{\epsilon}{2\beta_o}\left(\frac{2U_o}{H^{\frac{1}{2}}Z_c^{\frac{3}{2}}}\right)^{\frac{1}{2}} \left(1+U_o\beta_o^{\frac{1}{2}}\right)^2 \frac{\left(3U_o\beta_o^{\frac{1}{2}} + \left(\frac{2U_o}{H^{\frac{1}{2}}Z_c^{\frac{3}{2}}}\right)^{\frac{1}{2}}\right)}{\left(U_o\beta_o^{\frac{1}{2}} + \left(\frac{2U_o}{H^{\frac{1}{2}}Z_c^{\frac{3}{2}}}\right)^{\frac{1}{2}}\right)^3}$$

where

$$\frac{\rho_c}{\rho_o} = \frac{U_o}{U_c Z_c^2} = \frac{2U_o}{H^{\frac{1}{2}}Z_c^{\frac{3}{2}}} \qquad (43)$$

Equation (42) determines (U_c, Z_c) as a function of U_o, the normalized velocity at the reference level r_o, assuming H, ϵ, and β_o are given at the reference level. In order to obtain physical solutions which are supersonic at infinity and subsonic at the base of the corona, we require that such solutions pass through the critical point (cf Parker 1963), i.e., that (U_c, Z_c) satisfy the modified Bernoulli relation. Using Equations(35), (42), and (43), this requires that U_o be such that

$$\frac{a}{(a-1)}\left(\frac{2U_o}{H^{\frac{1}{2}}Z_c^{\frac{3}{2}}}\right)^{a-1} - \frac{3H}{4Z_c}$$

$$- \frac{\epsilon}{\beta_o}\left(1+U_o\beta_o^{\frac{1}{2}}\right)^2 \frac{\left(2U_o\beta_o^{\frac{1}{2}} + \left(\frac{2U_o}{H^{\frac{1}{2}}Z_c^{\frac{3}{2}}}\right)^{\frac{1}{2}}\right)}{\left(U_o\beta_o^{\frac{1}{2}} + \left(\frac{2U_o}{H^{\frac{1}{2}}Z_c^{\frac{3}{2}}}\right)^{\frac{1}{2}}\right)^2} \qquad (44)$$

$$= U_o^2 + \frac{a}{(a-1)} - H - \frac{\epsilon}{\beta_o}\left(2U_o\beta_o^{\frac{1}{2}} + 1\right)$$

Assuming that H, ϵ, and β_o are given at the reference level, Equations (42b) and (44) are of the form

$$f(U_o, Z_c) = 0$$

$$g(U_o, Z_c) = 0$$

We use Equation (42b) to determine Z_c as a function of U_o, and then Equation (44), in the form $G(U_o) = g\big(U_o, Z_c(U_o)\big) = 0$, determines U_o. For this value of U_o, the solution for U(Z) given by Equation (35) (taking the lower branch for $Z < Z_c$ and the upper for $Z > Z_c$) passes through the critical point, and this is the solar wind solution.

The detailed dependence of the Alfvén wave amplitudes as a function of r is of interest, and we define the amplification coefficient A to be the ratio

$$A(r) = \frac{\delta B(r)}{B(r)} \Big/ \frac{\delta B_o}{B_o} \tag{45}$$

Using Equations (22) and (24), we have

$$A(r) = \left(\frac{r}{r_o}\right)^2 \left(\frac{\rho}{\rho_o}\right)^{3/4} \left[\frac{1 + V_A^o/V_o}{1 + \frac{V_A^o}{V_o}\left(\frac{\rho}{\rho_o}\right)^{\frac{1}{2}}}\right] \tag{46}$$

C. Numerical Solutions and Discussion

1. Reference Level Parameters

It is easily seen that the inclusion of the wave energy flux in Parker's one fluid polytrope model of the solar wind [Parker, 1963]

should lead to significant modifications of the solutions. For example, consider the energy flux at a reference level $r_o = 10^6$km, an altitude about 3×10^5 km above the photosphere. The streaming velocity of the solar wind at this level is generally much less than the Alfvén velocity, so that the outward energy flux across the reference level in the coronal Alfvén waves is given by

$$F_w^o = V_A^o \frac{\delta B_o^2}{8\pi} (4\pi r_o^2) = 2.2 \times 10^{33} \frac{\epsilon B_o^3}{N_o^{\frac{1}{2}}} \text{ergs/sec} \quad (47)$$

where ϵ is $(\delta B_o)^2/2B_o^2$, B_o is in gauss, and N_o is in protons per cubic centimeter. If we take representative values of B_o and N_o to be 1 gauss and 2×10^7 cm^{-3} respectively, then the Alfvén velocity at r_o is about 500 km/sec, and the outward efflux of wave energy is $\epsilon(5 \times 10^{29})$ ergs/sec. Moderate values of ϵ ($\simeq .01$) give high energy fluxes ($\simeq 5 \times 10^{27}$ ergs/sec) at the reference level. These flux estimates are to be compared to estimates of the energy flux due to thermal conduction from the lower corona on the order of 2×10^{27} ergs/sec [Parker, 1963], and of the energy flux in the solar wind at 1 a.u. on the order of 10^{27} ergs/sec. Even small amplitude Alfvén waves at 10^6 km are associated with large energy fluxes because of the high Alfvén velocity. It is therefore reasonable to expect moderate amplitude Alfvén waves at the reference level to cause significant changes in the solar wind streaming properties far from the sun.

Numerical solutions for the wave modified wind model have been obtained for a variety of different parameters, and we illustrate

their general properties by presenting representative cases. The reference level r_o is taken to be 10^6 km, and the density N_o and the field strength B_o at this level are taken to be the same in all cases, with values of $2 \times 10^7/cm^3$ and 1 gauss, respectively. The 1 gauss field gives a radial field strength of 4.44 gamma at 1 a.u., in reasonable agreement with observed values. The heating of the corona above the reference level by thermal conduction is represented by the amount the polytrope index α is less than the adiabatic value of 5/3. For these calculations, we fix α at 1.2283, for reasons which will soon be evident. The remaining free parameters for these calculations are thus ϵ, which is representative of the wave energy flux at r_o, and T_o, the coronal temperature there.

The coronal plasma is assumed to be fully ionized hydrogen, so that the pressure p is 2NkT. From Equations (30) and (31), we have

$$H = 8.07 \times 10^6/T_o \tag{48}$$

$$\beta_o = 6.9 \times 10^{-15} N_o T_o / B_o^2 \tag{49}$$

In keeping with Equation (28), the solar wind velocity V is reduced to dimensionless form by dividing by the velocity V_S^o, where

$$V_S^o = \left(\frac{2p_o}{\rho_o}\right)^{\frac{1}{2}} = 1.82 \times 10^4 T_o^{\frac{1}{2}} \tag{50}$$

From Equation (21)

$$V_A^o = \frac{B_o}{(4\pi N_o m_p)^{\frac{1}{2}}} = 2.18 \times 10^{11} \frac{B_o}{(N_o^{\frac{1}{2}})} \tag{51}$$

Table 10

Reference Level Parameters
($r_o = 10^6$km)

T_o	N_o	B_o	H	β_o	V_S^o	V_A^o
(^oK)	(cm^{-3})	(gauss)			(km/sec)	(km/sec)
1×10^6	2×10^7	1	8.07	.14	182.	489.
1.3×10^6	2×10^7	1	6.21	.18	207.	489.
1.7×10^6	2×10^7	1	4.75	.24	237.	489.
2.0×10^6	2×10^7	1	4.04	.28	257.	489.

where N_o, T_o, and B_o are in cm^{-3}, degrees Kelvin, and gauss, respectively, and V_A^o and V_S^o are in cm/sec. Table 10 gives the values of these various parameters at r_o for four different values of T_o.

Given a value of T_o at the reference level (with fixed N_o and B_o), we calculate H and β_o using Equations (48) and (49). If we also choose a value of ϵ, then Equations (42b) and (44) can be solved numerically for the normalized parameters U_o and Z_c (cf. Equations (29) and (32)). The velocity V_o of the solar wind at the reference level is then given by $V_S^o U_o$, and the critical radius by $r_o Z_c$. Given U_o, we numerically solve the transcendental Equation (35) for U(Z), taking the lower branch ($U < U_c$) for $Z < Z_c$ and the upper branch ($U > U_c$) for $Z > Z_c$. The solar wind velocity V(Z) is then given by $V_S^o U(Z)$.

Figure 18 shows the locus of points in the V_o-r_c plane which satisfy Equations (42b) and (44), for the four values of T_o given in Table 10 and continuous values of ϵ from 0. to 10^{-1}. The behavior as ϵ approaches zero for the curves presented is qualitatively different depending on whether T_o is greater than or less than $1.5 \times 10^{6\,o}K$. In general, the behavior at infinitesimal ϵ is determined by whether H (Equation (48)) is greater than or less than $\frac{a}{a-1}$, and we discuss these two classes of solutions seperately.

2. Wave Modifications of the Parker Solutions

The parameter H as defined above (Equation 31)) is the negative of the gravitational potential energy per gas atom at the

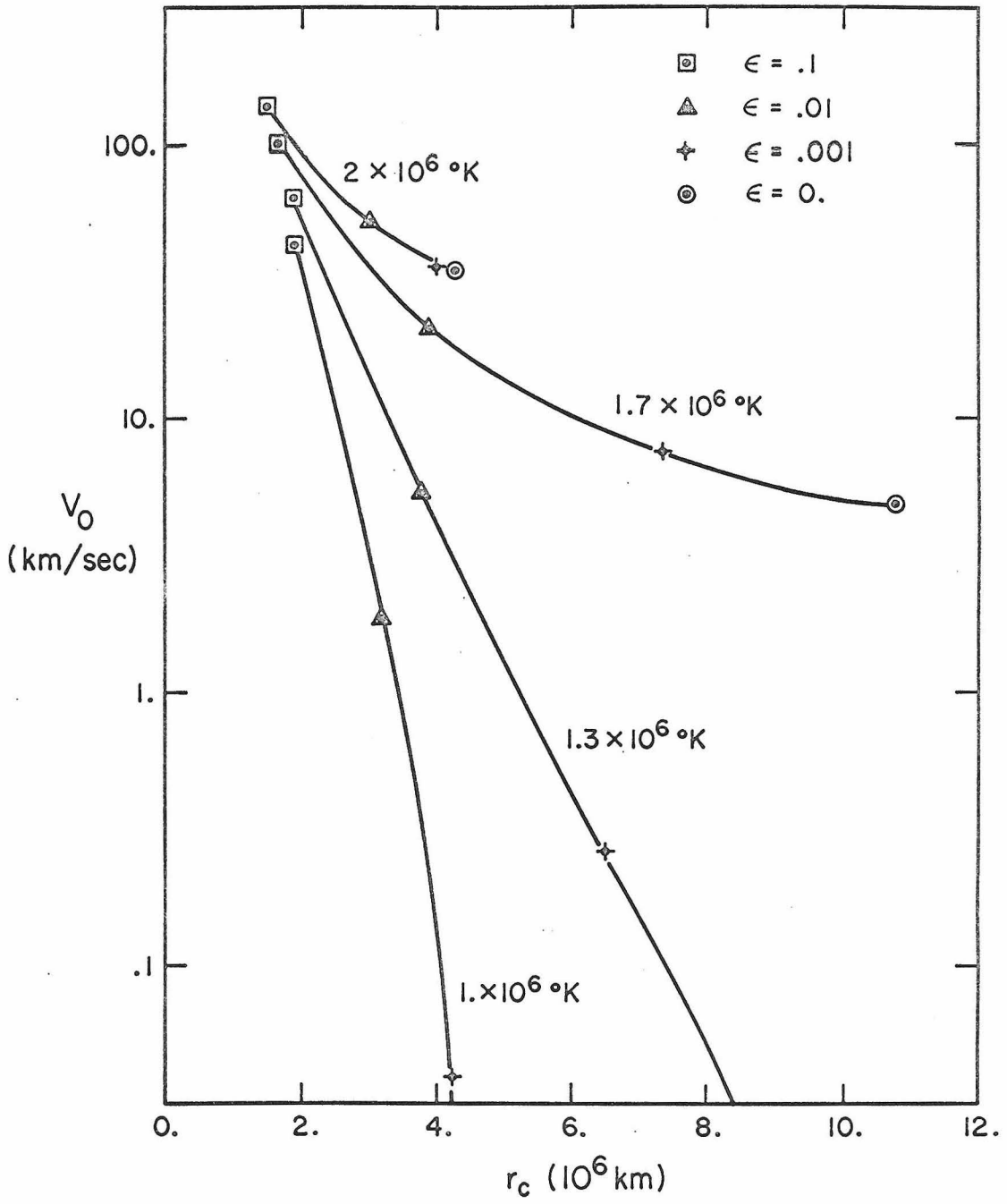

Figure 18. Solution points (V_o, r_c) for four values of T_o and continuous values of ϵ from 0. to .1, as indicated.

reference level in units of the thermal energy there. In Parker's models, H must be in the interval $2a < H < \frac{a}{a-1}$. The lower limit on H represents the point at which the solar gravitational field becomes too weak to simulate the throat of a Laval nozzle and allow the transition from subsonic to supersonic flow. Thus, if $H < 2a$, the corona explodes outward into space, and a steady state expansion can be maintained only if gas is supplied at a supersonic velocity at the base of the corona. The upper limit on H represents the point at which the solar gravitational field becomes too strong to allow expansion. Thus if $H > \frac{a}{a-1}$, the corona is contained as a static atmosphere. For the fixed value of a we have chosen, T_o must be greater than $T_{min} = 1.5 \times 10^6\ ^oK$ (Equation (45)) for Parker's wind solutions to exist. We limit ourselves in this section to a discussion of cases with T_o above this value, so that the Parker solutions exist at $\epsilon = 0$.

In Figure 18, the Parker critical point solutions are at the $\epsilon = 0$. positions on the $2 \times 10^6\ ^oK$ and the $1.7 \times 10^6\ ^oK$ curves. The effect of the waves (increasing ϵ from zero) is to increase the solar wind velocity at the reference point r_o, and decrease the critical radius r_c. A decrease in r_c implies an increase in the normalized critical velocity U_c (Equation (42a)). For a given value of ϵ, this change is more pronounced if T_o is closer to T_{min} (compare the $2.0 \times 10^6\ ^oK$ and the $1.7 \times 10^6\ ^oK$ curves in Figure 18). Figure 19 shows the solar wind velocity at 10^6km and at 1 a.u., and the solar wind particle density N (in cm^{-3}) at 1 a.u. as functions of T_o, for

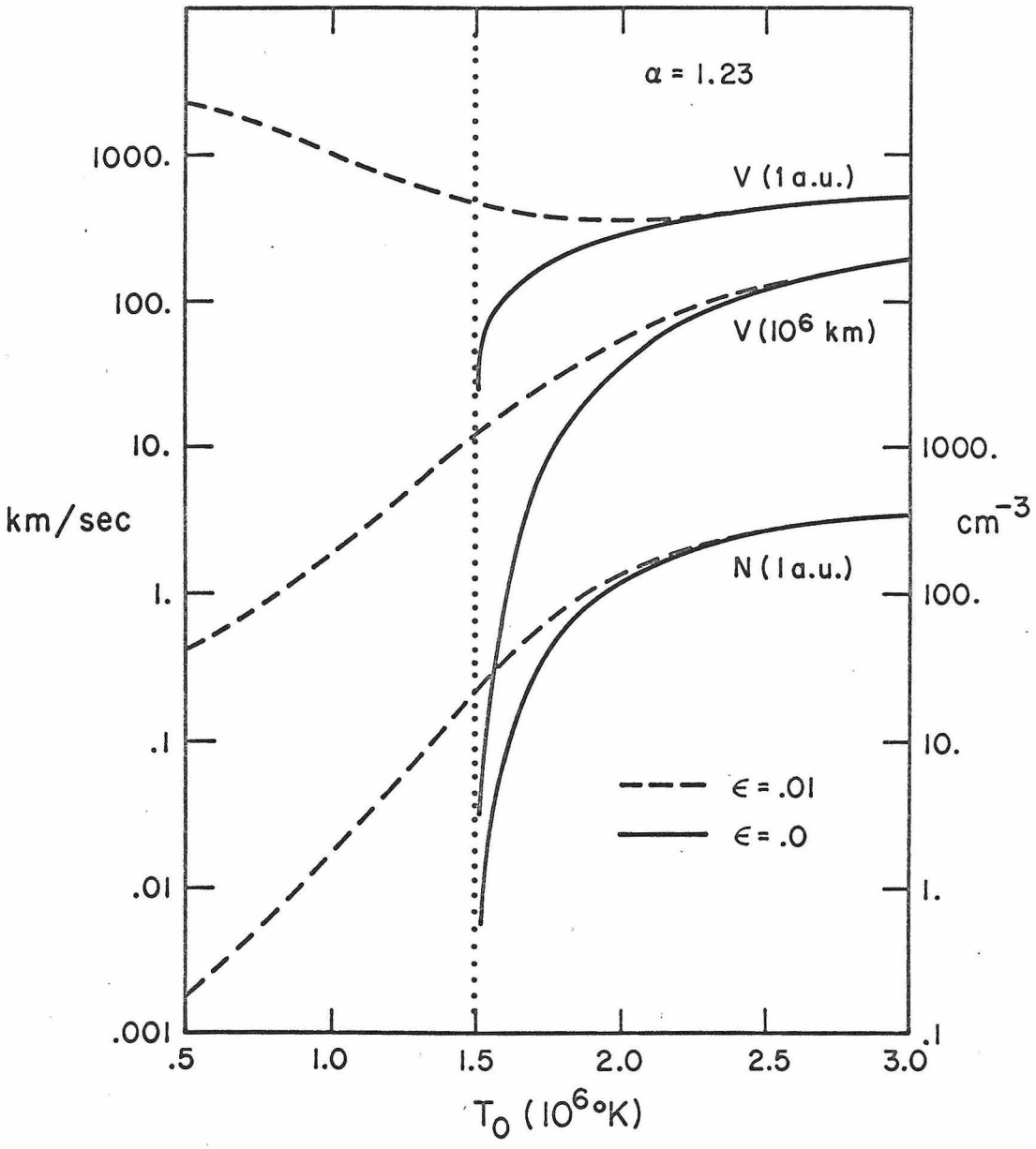

Figure 19. The solar wind velocity V at 1 a.u. and 10^6 km, and the proton particle density N at 1 a.u., as functions of T_o, for two values of ϵ (0. and .01).

two values of ϵ (0. and .01). The Parker solutions ($\epsilon = 0.$) are considerably changed for $\epsilon = .01$ and values of T_o only slightly above T_{min} (1.5×10^6 °K). The effect is less pronounced if T_o is much greater than T_{min}.

We would like to understand why for small fixed values of ϵ the Parker solutions are more strongly modified if T_o is closer to T_{min}. In part this is due to the fact that as T_o increases for fixed ϵ, the energy flux due to thermal conduction and convection becomes more important, eventually dominating the fixed wave energy flux. It is also due to the specific form of the interaction between the wind and the waves in this model. Consider the Alfvén wave amplification coefficient A(r) (Equation (45)) for unmodified Parker solutions ($\epsilon = 0.$, i.e. the waves are infinitesimal and transport zero energy flux). A(r) and the velocity V(r) are shown in Figure 20 for two values of T_o and $\epsilon = 0$. The shape of the A(r) curves is quite different for the $T_o = 1.6 \times 10^6$ °K and the $T_o = 2.8 \times 10^6$ °K solutions. This difference can be qualitatively explained by noting that

$$A(r) = \begin{cases} \left(\frac{r}{r_o}\right)^2 \left(\frac{\rho}{\rho_o}\right)^{1/4} \left(1+\frac{V_o}{V_A^o}\right) & \text{if } V \ll V_A \\ \left(\frac{r}{r_o}\right)^2 \left(\frac{\rho}{\rho_o}\right)^{3/4} \left(1+\frac{V_A^o}{V_o}\right) & \text{if } V \gg V_A \end{cases} \qquad (52)$$

If $\frac{\rho}{\rho_o}$ goes as r^{-s}, A(r) tends to go as $r^{2-(s/4)}$ in the sub-Alfvénic regime, and as $r^{2-(3s/4)}$ in the super-Alfvénic regime. If $s = 2$, this is $r^{3/2}$ or $r^{\frac{1}{2}}$, respectively. The $T_o = 1.6 \times 10^6$ °K Parker solu-

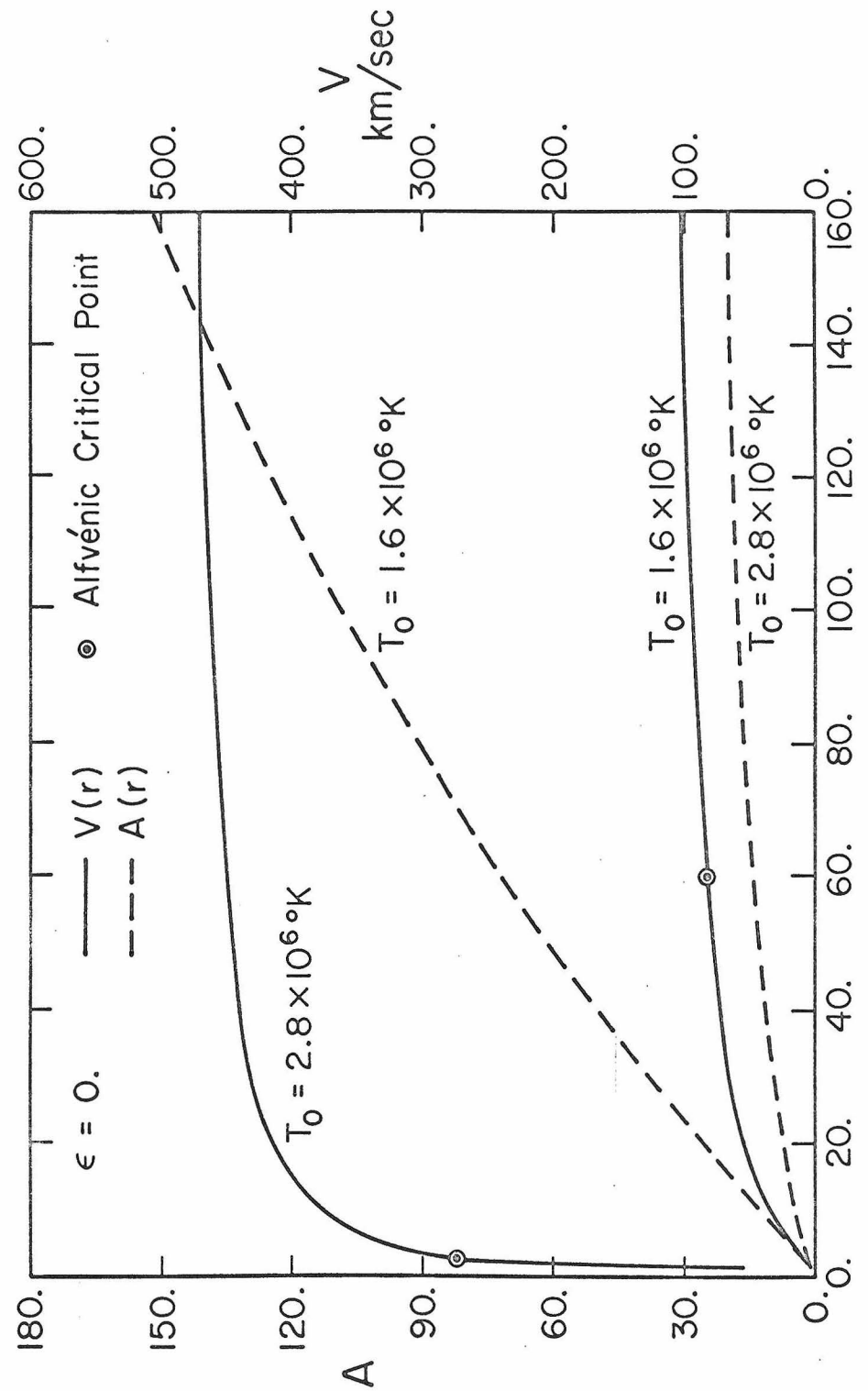

Figure 20. The amplification coefficient A and the solar wind velocity V as functions of r for two unperturbed Parker solutions.

tion in Figure 20 just barely attains escape velocity, and does not become super-Alfvénic until almost 60 x 10^6km, with the reference velocity V_o = .9 km/sec. Thus A(r) tends to increase faster than $r^{\frac{1}{2}}$ over much of the range from 10^6km to 1 a.u. On the other hand, the T_o = 2.8 x 10^6 °K Parker solution is much more energetic, and becomes super-Alfvénic almost immediately, at less than 3 x 10^6km, with V_o = 168 km/sec. A(r) in this case goes as $r^{\frac{1}{2}}$ over almost the entire range from 10^6km to 1 a.u.

The differing behaviors of δB as a function of r in the sub-Alfvénic and super-Alfvénic solar wind affects the rate at which work is done on the wind by the waves in the two regimes. Equation (26a) can be written as

$$\tfrac{1}{2} V^2 + \frac{a}{(a-1)} \frac{p_o}{\rho_o} \left(\frac{\rho}{\rho_o}\right)^{a-1} - \frac{GM_\odot}{r} + fw = \text{constant} \tag{53}$$

where

$$fw = \frac{-\epsilon}{2} \frac{V_A^o}{V_o} (V_A^o + V_o)^2 \frac{(2M_A+1)M_A}{(1+M_A)^2} \tag{54}$$

$$M_A = \frac{V}{V_A} \tag{55}$$

M_A is the solar wind Alfvén mach number The solar wind velocity at infinity is easily seen to be

$$V_\infty^2 = (V_S^o)^2 \left[U_o^2 + \frac{a}{a-1} - H\right] + \epsilon (V_A^o)^2 \left(\frac{V_A^o}{V_o}\right)\left(2 + \frac{3V_o}{V_A^o}\right) \tag{56}$$

The second term in Equation (56) is the increase in the square of the solar wind velocity at infinity due to the waves. Generally, $V_o \ll V_A^o$,

so that the increase at infinity is given approximately by $2\epsilon(V_A^o)^2 \times (V_A^o/V_o)$. From Equation (54), it can be seen that 2/3 of this additional velocity is added at values of M_A of less than 3. The waves are most effective in doing work on the wind at low Alfvénic mach numbers.

This property of the wave/wind interaction explains qualitatively why the additional velocity at infinity due to the waves depends directly on the ratio V_A^o/V_o. If this quantity is large (small V_o), then generally the solar wind will not become super-Alfvénic until far from the sun. Under these conditions, even a relatively small rate of Alfvénic energy transport into the corona can do a large amount of work on the sub-Alfvénic solar wind, since energy can be propagated into the wind (at the Alfvén velocity) over a relatively long time and distance. The velocity of the wind at infinity is increased by a significant amount as long as $\epsilon(V_A^o/V_o) \simeq 1$. Even if $\epsilon \ll 1$, the waves can still have a large effect as long as $(V_A^o/V_o) \gg 1$. On the other hand, if V_A^o/V_o is not large, then the solar wind becomes super-Alfvénic relatively close to the sun, and the region in which the waves are most effective in doing work on the wind is substantially diminished. For example, the fixed value of $\epsilon = .01$ in Figure 19 results in large changes in the Parker solutions for T_o only slightly above T_{min} (V_o very small), but causes increasingly smaller modifications as T_o increases (V_o increasing).

It should be noted that care must be taken in using estimates for the amplification coefficient A based on the unperturbed Parker

solutions ($\epsilon = 0.$), since the inclusion of the finite amplitude of the waves may significantly change the large scale structure of the solutions. For example, Figure 21 is a plot of A(r) and V(r) for a fixed value of T_o and two values of ϵ (0. and .01), showing a large reduction in values of A(r) for the finite amplitude wave solutions. Reliable estimates of amplification coefficients must be based on self-consistent solutions which allow for the possible influence of wave energy and momentum flux terms.

As values of ϵ increase, the waves have a greater influence on the wind solutions, until they eventually become the dominant energy source. In Figure 18, solutions in the V_o-r_c plane for ϵ=.1 change only slightly when T_o is changed. Although we do not show it here, variations in the polytrope index α also cause little change in the solution points when $\epsilon = .1$, even for α equal to the adiabatic value of 5/3. The energy flux which drives the solar wind for these solutions is almost entirely due to the Alfvén waves, with variations in the energy flux due to thermal conduction and convection causing relatively small perturbations in the solutions. Figures 22, 23, and 24 show the variation as a function of ϵ in the solar wind velocity V at 1 a.u., the particle density N at 1 a.u., and the amplification coefficient A at 1 a.u., respectively, for the four values of T_o given in Table 10. As ϵ increases from small values to .1, the 1.7×10^6 ^oK and 2.0×10^6 ^oK solutions move from the unperturbed Parker values at 1 a.u. toward similar wave dominated values. For reasons discussed above, the 1.7×10^6 ^oK solutions show more appreciable

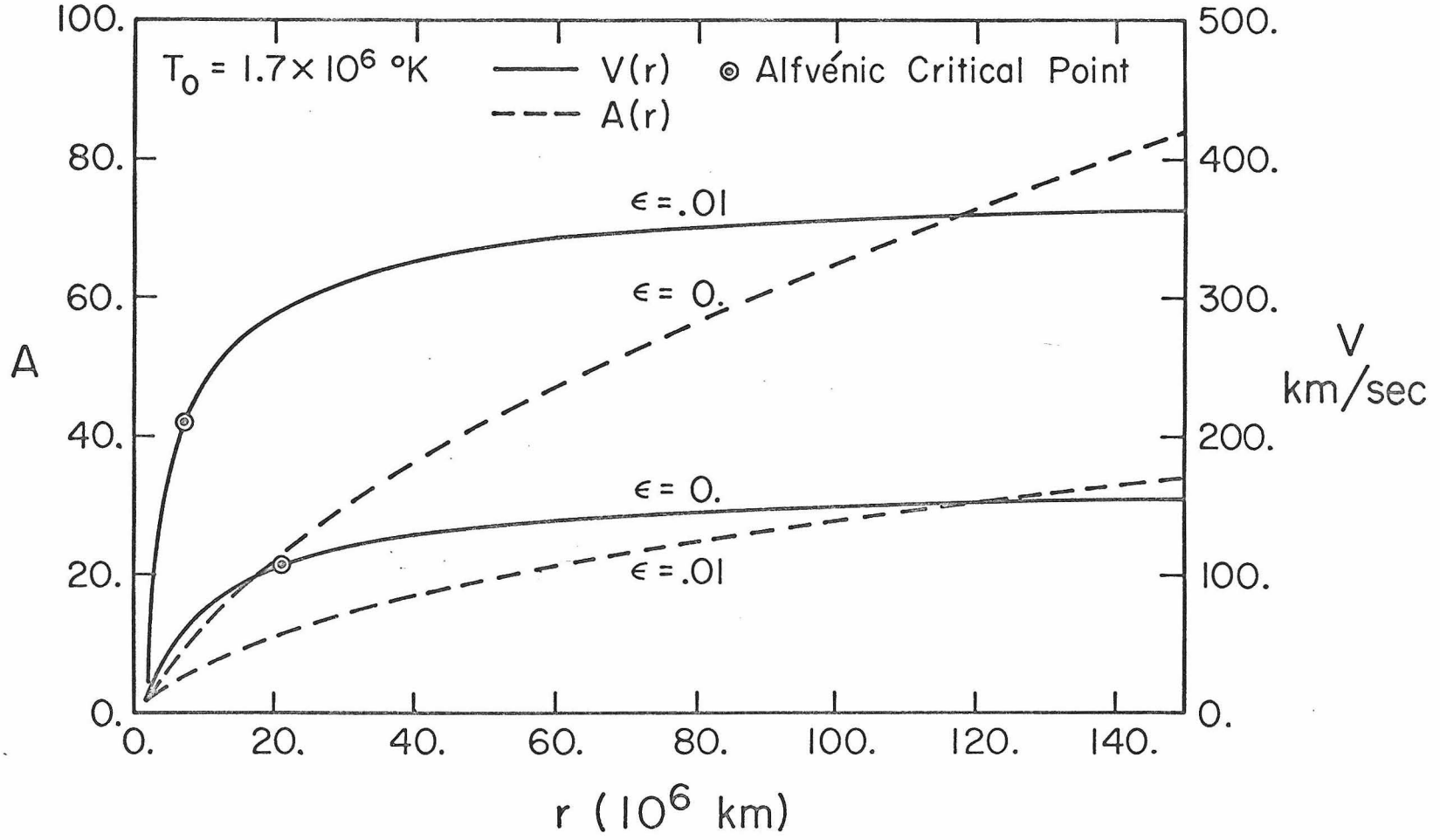

Figure 21. The amplification coefficient A and the solar wind velocity V as functions of r for a fixed value of T_o and two values of ϵ (0. and .01).

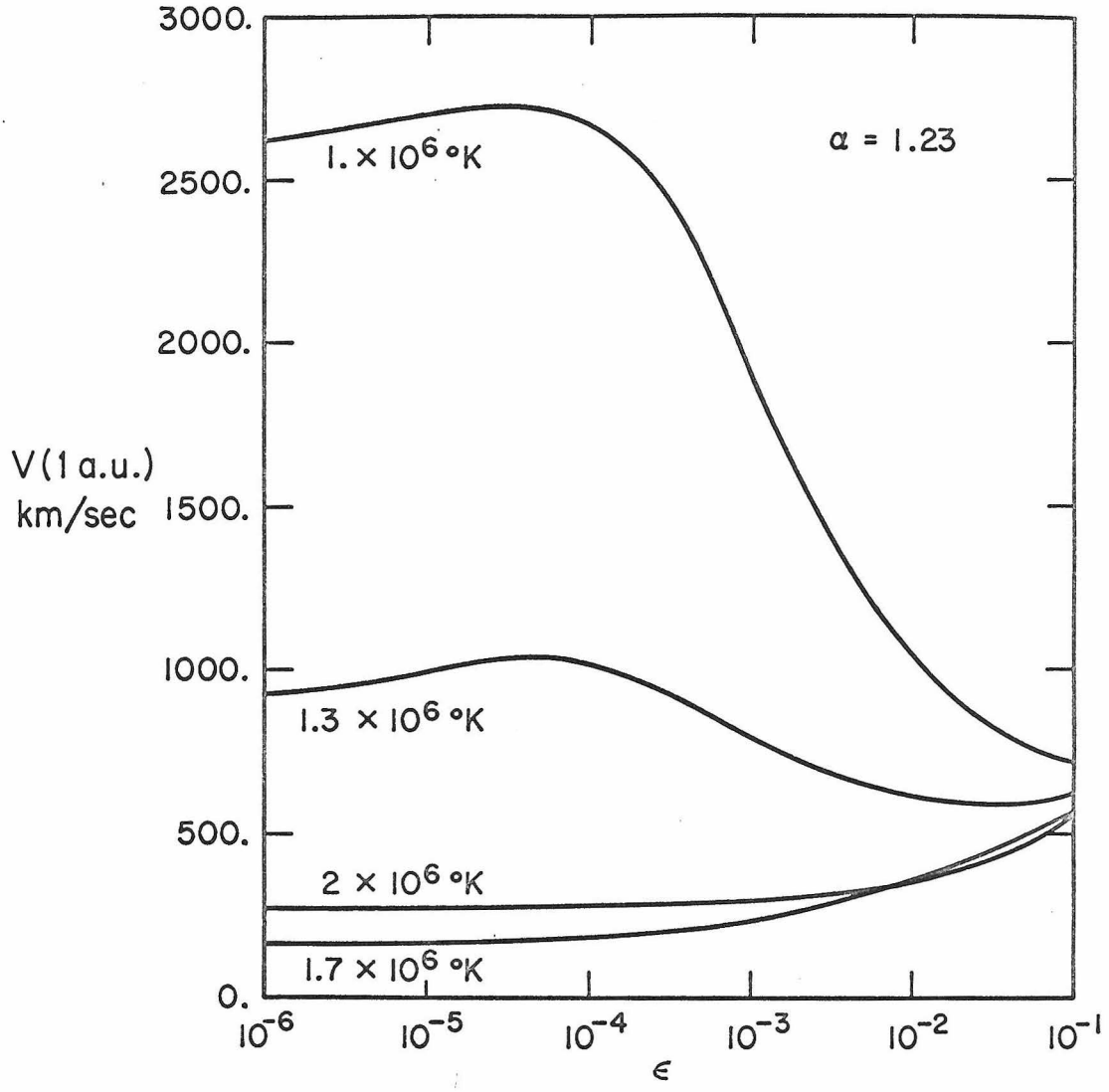

Figure 22. The solar wind velocity at 1 a.u. as a function of ϵ for four values of T_o.

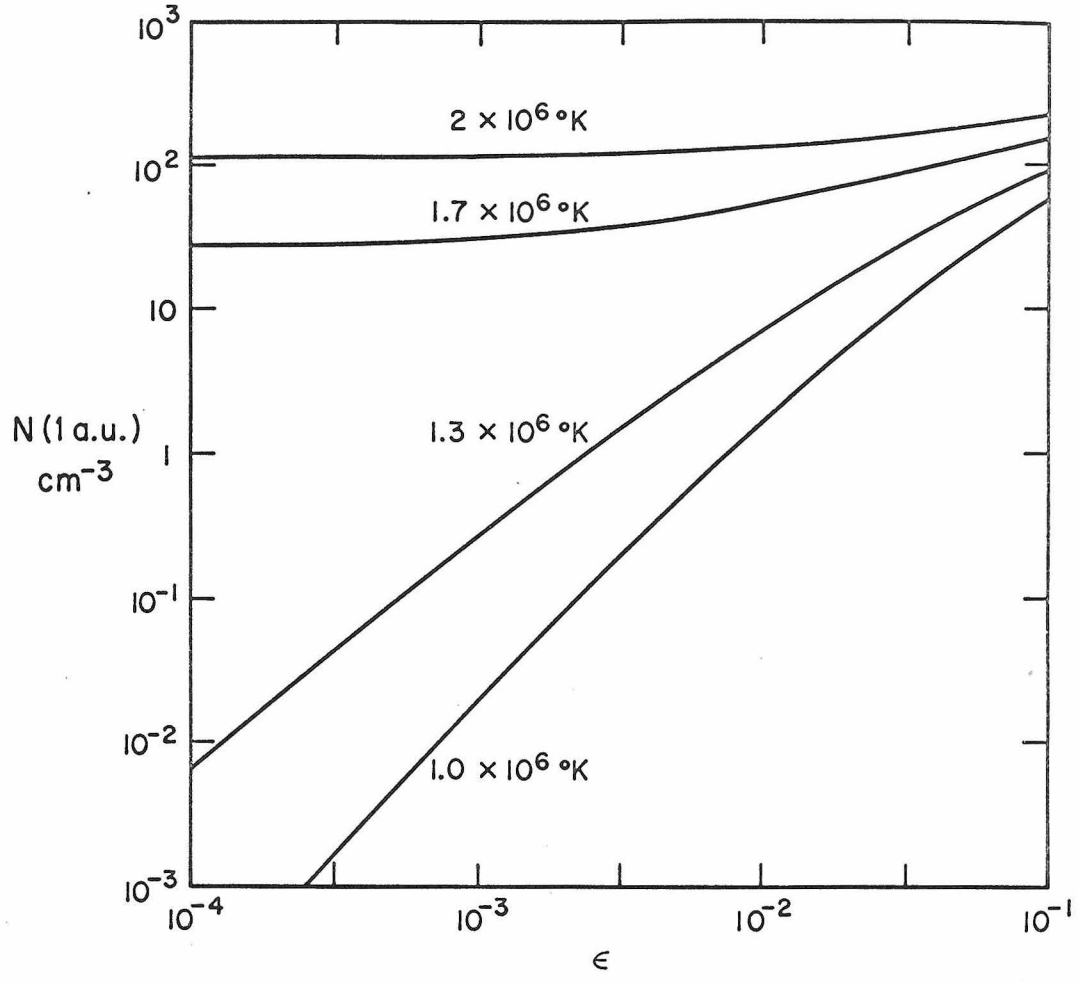

Figure 23. The proton particle density N at 1 a.u. as a function of ϵ for four values of T_o.

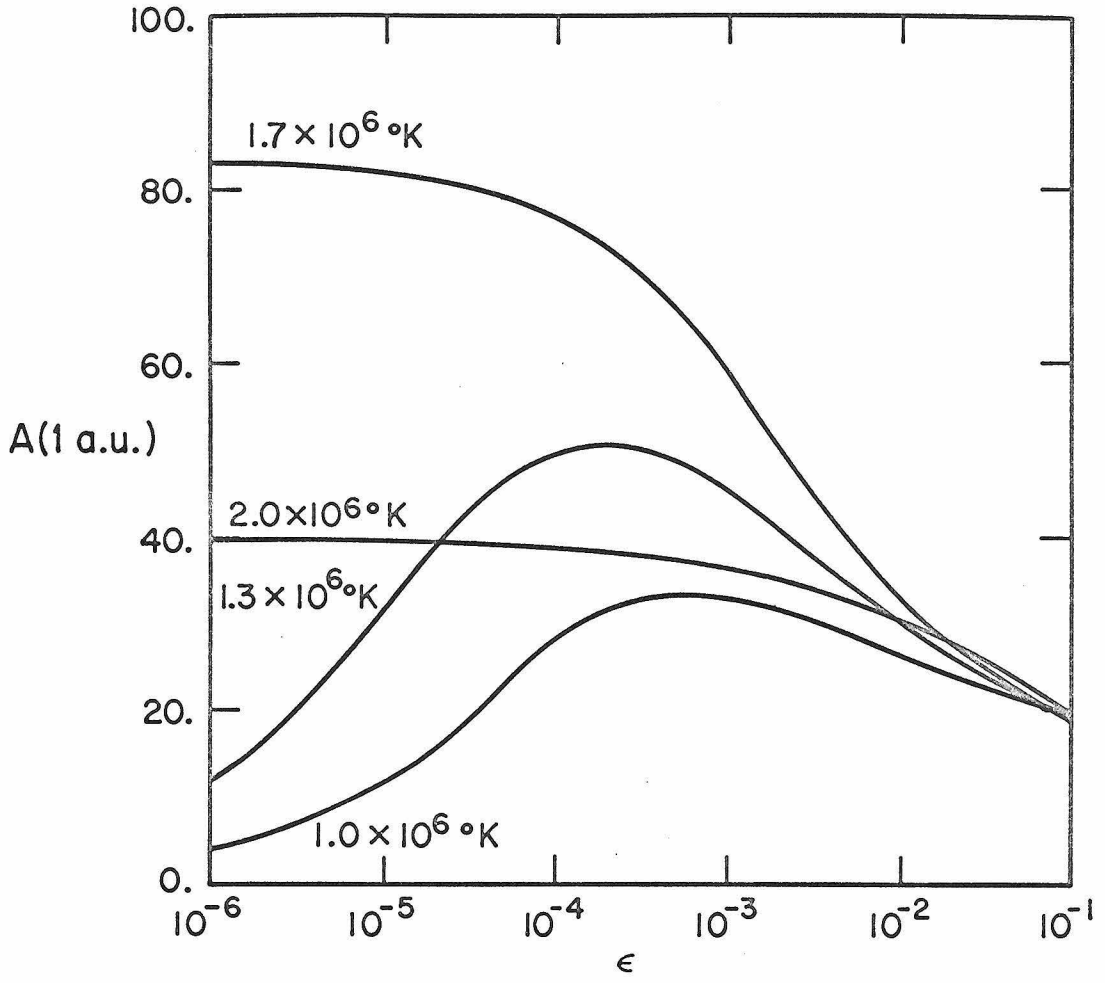

Figure 24. The amplification coefficient A at 1 a.u. as a function of ϵ for four values of T_o.

change at small values of $\epsilon (\simeq 10^{-3})$ than the 2.0×10^6 °K solutions. Note in particular that for the 1.7×10^6 °K solution, A at 1 a.u. drops from about 80 at $\epsilon = 10^{-6}$ to about 20 at $\epsilon = 10^{-1}$, a value close to that for the 2×10^6 °K solution at this point.

3. Wave Modifications of the Static Solutions

As can be seen in Figures 18, 22, 23, and 24, solar wind solutions for $\epsilon = .1$ are relatively insensitive to changes in T_o, since for high values of ϵ the waves are the primary energy source for the wind. As the wave energy flux is turned off (ϵ decreasing), the solutions with $T_o > T_{min}$ relax to the Parker solutions, as discussed above. For $T_o < T_{min}$, the behavior is quite different, as there are no dynamic solutions to relax to in the limit $\epsilon = 0$. For $T_o < T_{min}$ and ϵ identically zero, the corona is contained as a completely static atmosphere, with a density profile given by

$$N(r) = N_o \left[\frac{(a-1)}{a} H \left(\frac{r_o}{r} - 1 \right) + 1 \right]^{\frac{1}{(a-1)}} \tag{57}$$

and the top of the atmosphere at

$$r_m = r_o \left[\frac{H}{H - \frac{a}{(a-1)}} \right] \tag{58}$$

However, in our model, static solutions exist only if ϵ is identically zero. As long as ϵ is non-zero, even though infinitesimal, "wind" solutions to the Bernoulli equation exist. In the polytrope models, for fixed a and T_o, there is a certain fixed amount of energy available per unit mass, and either this energy is sufficient to lift the

plasma out of the sun's gravitational field ($H < \frac{a}{a-1}$) or not ($H > \frac{a}{a-1}$). In this idealized wave model, however, there is always an energy flux associated with the waves as long as ϵ is non-zero (see Equation (26b)), even if the wind velocity is everywhere zero. The specific wave/wind interaction developed above eventually transfers this wave energy flux into plasma streaming motion. Even if the wave flux is infinitesimal, it is sufficient to accelerate an equally infinitesimal amount of mass to escape velocities.

Figure 25 shows the wind solutions for $T_o = 1 \times 10^6$ ^oK and $\epsilon = 10^{-5}$. The heavy curve is the density profile for the static case ($\epsilon = 0.$), which has an atmospheric top at 3×10^6km. For the $\epsilon = 10^{-5}$ case, the density profile is very nearly the static one except near the top of the static atmosphere. At this point the velocity increases abruptly from very small values and there is a very small efflux of particles outward. Note that the particle density is down to $.01/cm^3$ by 6×10^6km. In the limit of very small ϵ and $T_o < T_{min}$, it can be seen from Equation (42b) and (44) that Z_c approaches a constant and V_o goes to zero as ϵ^2. Hence the solar wind velocity at infinity goes to infinity as ϵ^{-1} (Equation (56)), and the mass flux (Equation (22)) goes to zero as ϵ^2 as ϵ goes to zero. Solutions for very small ϵ and $T_o < T_{min}$ should not be taken seriously, since they are not relativistically correct. As can be seen from Figure 25, these solutions do reduce to the static cases, although in a pathological way. This is not unexpected, since in this model the purely static solutions have Alfvén velocities which approach infinity as the top of the atmosphere is reached.

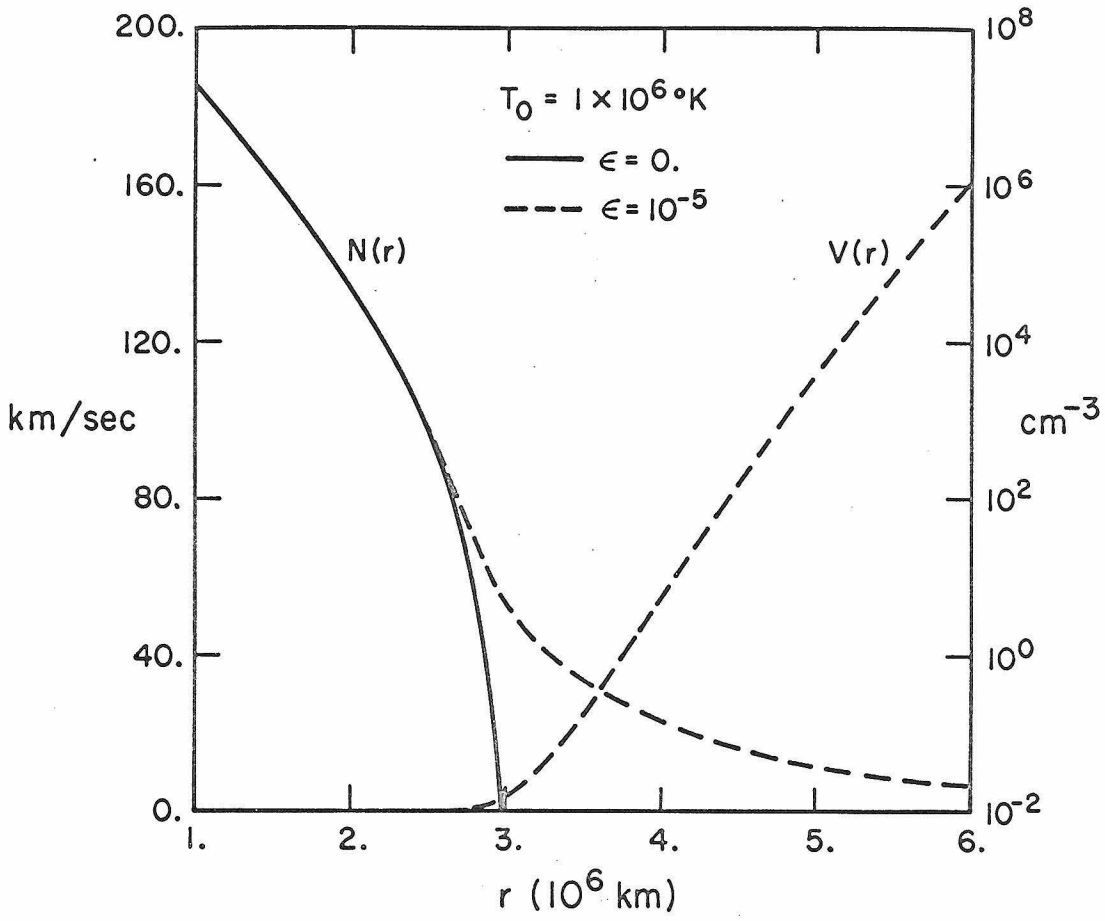

Figure 25. The solar wind velocity V and particle density N as functions of r for $\epsilon = 0.$ (static atmosphere) and $\epsilon = 10^{-5}$, with $T_o = 1 \times 10^6\ ^oK$.

The important point is that for moderate values of ϵ ($\gtrsim .001$) we still obtain reasonable solar wind solutions even if $T_o < T_{min}$. The Alfvén waves supply the additional energy needed to lift the coronal plasma out of the solar gravitational field. In Figure 19, for example the velocity and density curves for $\lambda = .01$ extend below T_{min} into the region where Parker polytrope solutions do not exist. Figures 22, 23, and 24 show the variations as a function of ϵ for V, N, and A at 1 a.u. for two previously static values of T_o (1.3×10^6 ^oK and 1.0×10^6 ^oK). The most striking feature of these solutions is the combination of high velocities and low densities. In Figure 19, for example, the velocity increases and the density decreases as T_o is reduced below T_{min} for $\epsilon = .01$. In Figures 22 and 23, the velocity increases and the density decreases as ϵ is reduced from 10^{-1} to 10^{-4}, for both the 1.3×10^6 ^oK and the 1.0×10^6 ^oK curves. In Parker's model, for fixed values of α and variable T_o, higher velocities are always associated with higher densities. In the wave driven solutions, we see that the reverse can be true; i.e., higher velocities with lower densities at 1 a.u.

4. Comparison with Observations

There are numerous deficiencies in this model if it is used to represent the actual solar wind. The model suffers from all the imprecisions characteristic of one fluid MHD polytrope models, as discussed by Parker [1965]. As far as the inclusion of the wave energy fluxes is concerned, there are two questionable assumptions in our representation. The first is the assumption that there is no

wave damping. As long as $\delta B/B < 1$, this is not unreasonable, since both from a theoretical and observational point of view Alfvén waves in the solar wind do not appear to damp rapidly under this condition. If $\delta B/B > 1$, however, nonlinear and/or mode coupling mechanisms will almost certainly result in wave damping. In our model, the wave amplitudes of the coronal Alfvén waves generally increase as r increases, so that at some point $\delta B/B$ may become equal to 1. Beyond this point, the waves will most probably damp at a rate sufficient to keep $\delta B/B \simeq 1$, thereby heating the plasma. If this point occurs at distances much greater than the critical radius r_c, the major change in the solutions due to wave damping will probably be an increase in the plasma temperature, with little change in the bulk velocity or density. If the damping is a major effect at less than the critical radius, then the bulk properties of the solutions far from the sun may change significantly, and a more complete theory is needed. In all of the numerical solutions discussed above, $\delta B/B$ does not become comparable to 1 until values of r greater than r_c.

The more serious deficiency of the model is the WKB approximation. The interplanetary Alfvén waves at 1 a.u. are observed to have wavelengths from 10^3 to 5×10^6 km, with decreasing power at shorter wavelengths. The frequency ω given by Equation (17) remains constant as we go inward toward the sun, and although the velocity V decreases, the Alfvén velocity V_A increases. The wavenumber spectrum observed at 1 a.u. is thus roughly the same as that at

10^6km. If we assume scale lengths of 10^6km for the solar wind velocity and density structures near the sun, we see that the largest observed wavelengths at 1 a.u. badly violate the WKB approximation closer to the sun. The correction of this defect in the model will probably require a detailed theory as to the actual mechanisms which generate the waves in the lower corona, as well as a complicated integration scheme. For the present, we can only point out that the wavelengths at 1 a.u. of 10^5km and less are probably adequately represented by the WKB approximation.

With these deficiencies in mind, we feel that the model is a reasonable first attempt to determine the effects of the coronal waves on the dynamics of the wind. It has two extremely attractive features. The first is the existence of wind solutions for ranges of coronal reference temperatures T_o for which there were no previous dynamic solutions. The second is the fact that wave driven solutions can easily produce the high velocities and low densities frequently observed in the solar wind at 1 a.u. For example, in Figure 4 the high velocity stream shown has an average velocity over the first three hours of day 193 of 697 km/sec, a proton number density of $1.3\,cm^{-3}$, an average field strength B of 5.9 γ, and an average most probable proton thermal speed of 110 km/sec. It is impossible to produce this combination of values at 1 a.u. in Parker models with reasonable parameters at 10^6 km. In the wave driven models, however, such solutions are quite reasonable. For example, using the values of N_o, B_o, and α given above, a value of $T_o = 1.3 \times 10^6\ ^oK$,

and $\epsilon = .003$, we obtain a solution which gives a velocity of 683 km/sec at 1 a.u., with a proton number density of 1.54 cm^{-3}. For this solution, $\delta B_o/B_o$ is .077, and $\delta B/B$ becomes 1 at $r = 26. \times 10^6$ km, with the critical radius r_c at 5.1×10^6 km. With no wave damping, the temperature $T \left(T_o \left(\frac{N}{N_o}\right)^{a-1}\right)$ at 1 a.u. is only 3×10^4 °K. However, $\delta B/B$ by 1 a.u. is 2.99. If we assume the wave energy density in excess of $\delta B/B = 1 ((\delta B - B)^2/8\pi)$ has been damped into the thermal energy density 2NkT, the plasma temperature is raised to $.76 \times 10^6$ °K, corresponding to a proton thermal velocity of 113 km/sec.

Reasonable values for a, N_o, B_o, T_o, and ϵ at 10^6 km thus can produce at 1 a.u. hot, high velocity, low density solar wind streams with large amplitude outwardly propagating Alfvén waves, as observed. As Parker [1963] points out, low velocity, dense, cold streams (the "quiet" solar wind), as in day 190 of Figure 4, can be easily obtained in the standard polytrope model ($\epsilon = 0.$) by suitable choices of a and T_o. It thus appears that Parker's classic solar wind model, as modified by the presence of Alfvén wave energy fluxes across the base of the corona, can reproduce all of the observed solar wind streaming states at 1 a.u. by suitable (and reasonable) choices of parameters at 10^6km.

CHAPTER VI

SUMMARY

The research sequence on which this thesis is based is typical of work in this field. The design of the experimental apparatus and the data acquisition during the course of the Mariner V mission preceeded the work described here. Beginning with the digitalized magnetometer readings from the spacecraft, a reduction procedure (including an evaluation of the quality of each observation) was carried out to organize the data into a form convenient for detailed analysis. Good quality data were then plotted over a wide range of time scales, and a detailed and extensive comparison was made between the field data and plasma data generously provided by the plasma experimenters, H. S. Bridge, A. J. Lazarus, and C. W. Snyder. Using both types of data, the Alfvén waves were identified, and their frequency of occurrence, direction of propagation, and patterns of occurrence with respect to the large scale stream structures were determined. On the basis of these observations, a qualitative model for the origins of the waves and their relation to the streaming properties of the wind was developed. Although not quantitative, the model serves to organize the large amount of data into a reasonably simple picture, and provides the basis for more quantitative analysis.

Observationally speaking, the properties of the waves at 1 a.u. are reasonably well established for this portion of the solar cycle (1967). The areas of significant future interest are long term obser-

vations at 1 a.u. and observations in regions closer to and further from the sun. It is obviously of importance to measure $\delta B/B$ over as wide a range of solar distances as possible, since the ratio is a measure of both initial wave amplitudes close to the sun and damping and propagation effects of the waves far from the sun. The detailed observational behavior of the waves far beyond the orbit of the earth (where the magnetic field becomes tightly wound in the classic spiral) is of particular interest. The proposed Pioneers F and G missions (Jupiter 1972-74) and the Mariner Mercury-Venus mission (1973) will thus be invaluable for observational studies of solar wind wave properties.

From a more theoretical point of view, we have investigated the properties of a simplified wind model which includes wave energy fluxes. Although the model is unrealistic in that it assumes a single fluid plasma with no wave damping, it provides useful insight into the qualitative effects of the observed waves on the actual solar wind. The next step is a two fluid model with a more sophisticated treatment of the energy transport equations (including wave damping). The effects of the rotation of the sun and the spiral field patterns on wave driven solutions is also of considerable interest. The spiraling of the magnetic field should have little effect on the solutions inside 1 a.u., but probably will have a large effect beyond 1 to 2 a.u. A more fundamental problem is the nature of the processes which generate the waves at or near the sun. This question is of obvious interest for both solar and interplanetary physics.

In conclusion, the thesis has resolved many observational points and given some consideration to the theoretical points these observations raise. The results provide the basis of and suggest possibilities for future investigations, both observational and theoretical.

REFERENCES

Barnes, A., Phys. Fluids, 9, 1483, 1966.

Barnes, A., Astrophys. J., 154, 751, 1968.

Barnes, A., Astrophys, J., 155, 311, 1969.

Belcher, J. W., L. Davis, Jr., and E. J. Smith, J. Geophys. Res., 74, 2302, 1969.

Burlaga, L. F., Solar Physics, 4, 67, 1968.

Burlaga, L. F., Solar Physics, 7, 54, 1969.

Burlaga, L. F., and K. W. Ogilvie, Ap. J., 159, 659, 1970.

Burlaga, L. F., K. W. Ogilvie and D. H. Fairfield, Astrophys. J., 155, L171, 1969.

Burlaga, L. F., K. W. Ogilvie, D. H. Fairfield, M. D. Montgomery, and S. J. Bame, NASA-GSFC preprint No. X-692-70-270, 1970.

Chew, G. F., M. L. Goldberger and F. E. Low, Proc. Roy. Soc., A236, 112, 1956.

Coleman, P. J., Jr., J. Geophys. Res., 71, 5509, 1966.

Coleman, P. J., Jr., Planetary Space Sci., 15, 953, 1967.

Coleman, P. J., Jr., Astrophys. J., 153, 371, 1968.

Connor, B. V., IEEE Trans. Magnetics, MAG-4, 391, 1968.

Davis, L., Jr., in The Solar Wind, edited by R. J. Mackin, Jr. and M. Neugebauer, p. 147, Pergamon Press, New York, 1966.

Davis, L., Jr. and E. J. Smith, Trans. Am. Geophys. Union, 49, 257, 1968.

Davis, L., Jr., E. J. Smith, P. J. Coleman, Jr., and C. P. Sonnet, in The Solar Wind, edited by R. J. Mackin, Jr. and M. Neugebauer, p. 35, Pergamon Press, New York, 1966.

Dessler, A. J., and J. A. Fejer, Planetary Space Sci., 11, 505, 1963.

Hartle, R. E. and A. Barnes, NASA-GSFC preprint No. X-621-70-114, 1970.

Hinich, M. J., and C. S. Clay, Rev. of Geophys., 6, 347, 1968.

Hundhausen, A. J., Space Sci. Rev., 8, 690, 1968.

Hundhausen, A. J., J. R. Ashbridge, S. J. Bame, H. E. Gilbert, and I. B. Strong, J. Geophys. Res., 72, 87, 1967.

Jokipii, J. R., and L. Davis, Jr., Astrophys. J., 156, 1101, 1969.

Landau, L. D., and E. M. Lifshitz, Electrodynamics of continuous media, Pergamon Press, New York, 1960.

Lazarus, A. J., Trans. Am. Geophys. Union, 51, 413, 1970.

Lazarus, A. J., H. S. Bridge, J. M. Davis, and C. W. Snyder, Space Res., 7, 1296, 1967.

Montgomery, D. C., and D. A. Tidman, Plasma Kinetic Theory, Chap. 9, McGraw-Hill Book Company, New York, 1964.

Neugebauer, M., and C. W. Snyder, in The Solar Wind, edited by R. J. Mackin, Jr., and M. Neugebauer, p. 3, Pergamon Press, New York, 1966.

Ness, N. F., Proceedings of the 13th International Conference on Cosmic Rays, Budapest, Hungary, 1969, in press.

Osterbrook, D. E., Ap. J., 134, 347, 1961.

Parker, E. N., Phys. Rev., 107, 924, 1957.

Parker, E. N., Interplanetary dynamical processes, John Wiley and Sons, New York, 1963.

Parker, E. N., Space Sci. Rev., 4, 666, 1965.

Parker, E. N., Space Sci. Rev., 9, 325, 1969.

Sari, J. W., and N. F. Ness, Solar Physics, 8, 155, 1969.

Scarf, F. L., J. H. Wolfe, and R. W. Silva, J. Geophys. Res., 72, 993, 1967.

Siscoe, G. L., L. Davis, Jr., P. J. Coleman, Jr., E. J. Smith and D. E. Jones, J. Geophys. Res., 73, 61, 1968.

Siscoe, G. L., B. Goldstein, and A. J. Lazarus, J. Geophys. Res., 74, 1759, 1969

Snyder, C. W., M. Neugebauer, and V. R. Raö, J. Geophys, Res., 68, 6361, 1963.

Sonnerup, B. U. Ö., and L. H. Cahill, Jr., J. Geophys, Res., 72, 171, 1967.

Stix, T. H., The Theory of Plasma Waves, Chap. 2, McGraw-Hill Book Company, New York, 1962.

Stringer, T. E., J. Nucl. Energy, C5, 89, 1963.

Sturrock, P. A., and R. E. Hartle, "Two-fluid model of the solar wind", Phys. Rev. Lett., 16, 628, 1966.

Thompson, W. B., An Introduction to Plasma Physics, Chap. 5, Pergamon Press, New York, 1962.

Unti, T. W. J., and M. Neugebauer, Phys. Fluids, 11, 563, 1968.

Van de Hulst, H. C., in The Sun, edited by G. P. Kuiper, p. 252, University of Chicago Press, Chicago, 1953.

Weber, E. J., and L. Davis, Jr., Ap. J., 148, 217, 1967.

Wilcox, J. M., and N. F. Ness, J. Geophys. Res., 70, 5793, 1965.

Wolfe, J. M., Trans. Am. Geophys. Union, 51, 412, 1970.